Ultra-Wideband Wireless Channel: Measurements, Analysis and Modeling

Ultra-Wideband Wireless Channel: Measurements, Analysis and Modeling

PROEFSCHRIFT

ter verkrijging van de graad van doctor
aan de Technische Universiteit Delft,
op gezag van de Rector Magnificus Prof. dr. ir. J.T. Fokkema,
voorzitter van het College voor Promoties,
in het openbaar te verdedigen op maandag 26 januari 2009 om 15:00 uur

door

Zoubir IRAHHAUTEN

elektrotechnisch ingenieur
geboren te Oujda, Morocco.

Dit proefschrift is goedgekeurd door de promotor:

Prof. dr. ir. L.P. Ligthart

copromotor:

Dr. ir. G.J.M. Janssen

Samenstelling promotiecommissie:

Rector Magnificus	voorzitter
Prof. dr. ir. L.P. Ligthart	Technische Universiteit Delft, promotor
Dr. ir. G.J.M. Janssen	Technische Universiteit Delft, copromotor
Prof. Dr. -Ing. R.S. Thomä	Ilmenau University of Technology
Prof. dr. ir. A.J. van der Veen	Technische Universiteit Delft
Prof. dr. ir. I.G.M.M. Niemegeers	Technische Universiteit Delft
Prof. dr. ir. J.C. Haartsen	Technische Universiteit Twente
Dr. ir. H. Nikookar	Technische Universiteit Delft

ISBN 978-90-76928-15-9

Copyright © 2009 by Z. Irahhauten

All rights reserved. No part of the material protected by this copyright notice may be reproduced or utilized in any form or by any means, electronic or mechanical, including photocopying, recording or by any information storage and retrieval system, without the prior permission of the author.

To my family.

Summary

Nowadays, Ultra-wideband (UWB) technology is gaining much attention in the field of wireless communication, mainly due to its unique capabilities and potential applications, also due to the large available unlicensed frequency band for these applications. However, the design and successful implementation of UWB transmission systems require a good understanding of the propagation characteristics of the radio channel. This thesis deals with the development of realistic channel models to support UWB communication design and evaluation.

Different ways exist to develop a UWB channel model. A major method, which is the focus of this thesis, is to use statistical approaches based on measurements. To this end, a time-domain measurement set-up covering the frequency band from 3.1 to 10.6 GHz has been developed. Different limitations which are specific for the time-domain measurement are highlighted and solutions have been proposed to remove these limitations. As the performance of any communication system is determined by the characteristics of the radio channel in which it operates, our measurements have been conducted in different environments e.g. indoor office, indoor industrial area, outdoor to indoor and and Wireless Personal Area Network (WPAN) environments. In order to provide a good statistical UWB channel characterization, a sufficient number of channel impulse responses (CIRs) are gathered. These CIRs are retrieved from the time-domain measured signals using an appropriate post-processing. Based on the measured data, different statistical channel models, including large, middle and small-scale fading, have been proposed for the frequency band 3.1-10.6 GHz.

UWB is a promising technology for several short-range wireless applications (e.g. WPAN). However, in these applications the transmit and receive antennas are very close to each other and far-field antenna conditions, assumed in most available link budget models, may not be satisfied. Under the near-field conditions, variations in the link budget and pulse shape compared to the far-field can be observed. In this thesis, a new empirical UWB link budget model for

short-range UWB channels is proposed and validated by measurements and simulations using different types of antennas. The proposed model includes frequency, antenna size and orientation as parameters, and shows a good agreement with the simulations and the measurements.

Usually in the statistical modeling of the UWB channel, the whole UWB band is sounded. Because of the very large bandwidth, the measurement set-up becomes complex, and consequently different parameters must be taken into consideration. In this thesis, a new approach to estimate the wireless UWB channel is introduced where partial information of sub-band channels is available (measured) and used in the estimation process.

Positioning information in indoor environments is becoming more important and attractive, especially for wireless ad-hoc networks and area dependent wireless services. One of the main issues in positioning is how to achieve a good range estimation. Usually, the required range accuracy depends on the application and can vary from a few centimeters to tens of meters. UWB radio seems to be a promising solution for achieving a high accuracy. The last part of this thesis deals with the application of UWB technology for ranging/positioning. For instance, different methods based on time of arrival or signal strength, to estimate the range in dense indoor multipath environments are evaluated.

Zoubir Irahhauten
Delft, September 2008

Contents

Summary i

Contents iii

1 Introduction 1

1.1 Introduction to UWB 1
1.2 Motivations and research questions 2
1.3 Research objectives 5
1.4 Novelties and main contributions 6
1.5 Scope of the thesis 7

2 Wireless Radio Channel Overview 9

2.1 Mathematical modeling of wireless channels 10
2.1.1 Time-domain (impulse response) modeling 10
2.1.2 Frequency-domain modeling 11
2.2 Channel parameters for system design 11
2.2.1 Power delay profile 11
2.2.2 Path loss, shadowing and fading 12
2.2.3 RMS delay spread 14
2.2.4 Correlation 14
2.3 Models for channel parameters 15
2.3.1 Path amplitude models 15
2.3.2 Path arrival time models 17
2.3.3 PDP models 18
2.4 Literature survey of UWB channel measurements 19

3 Measurement Set-up for UWB Channel Characterization 21
3.1 Measurement sounding techniques . . . 22
3.1.1 FD technique . . . 22
3.1.2 TD technique . . . 23
3.1.3 TD versus FD technique . . . 23
3.2 The measurement set-up . . . 25
3.2.1 Sampling oscilloscope . . . 25
3.2.2 Pulse generator and shaper . . . 34
3.2.3 Reference channel . . . 34
3.2.4 Antennas . . . 36
3.2.5 Low Noise Amplifier . . . 41
3.3 Total set-up performance . . . 42
3.3.1 Impact of antenna mismatch . . . 42
3.3.2 Suppression of noise and narrowband interference . . . 44
3.4 Validation of time domain measurements . . . 47
3.5 Chapter summary . . . 48

4 UWB Channel Measurements: Processing and Modeling Results 49
4.1 Description of measurement scenarios . . . 49
4.1.1 Indoor office environment . . . 50
4.1.2 Indoor industrial environment . . . 51
4.1.3 Outdoor to indoor environment . . . 51
4.1.4 WPAN environment . . . 52
4.1.5 Roughness scenario . . . 54
4.2 Data analysis and post-processing . . . 56
4.2.1 Antennas and components effect . . . 56
4.2.2 De-convolution methods . . . 56
4.2.3 Threshold setting . . . 61
4.3 Modeling results and discussion . . . 64
4.3.1 Large-scale path-loss model . . . 64
4.3.2 Fading margin model . . . 68
4.3.3 Small-scale fading model . . . 71
4.3.4 Roughness model . . . 83
4.3.5 Time dispersion model . . . 85
4.4 Chapter summary . . . 88

5 Analysis and Modeling of Short-Range UWB Channels 91
5.1 Introduction . . . 91
5.2 Near-field effects analysis . . . 92
5.2.1 Phase error . . . 92
5.2.2 Antenna mismatch . . . 100
5.2.3 Reradiation between antennas . . . 101

5.3 Proposed link budget model 103
5.4 Measurements, simulations and verification 104
5.4.1 Measurement set-up and description 104
5.4.2 Data processing method 106
5.4.3 Measurement and modeling results 106
5.4.4 Model parameters 110
5.5 Conclusions 115

6 UWB Channel Estimation Based on Partially Measured Frequency Responses 117
6.1 Introduction 117
6.2 A new approach for UWB channel modeling 118
6.2.1 Description 118
6.2.2 Advantages 118
6.2.3 Analytical integration 120
6.3 UWB channel estimation methods 124
6.3.1 Interpolation approach 124
6.3.2 Frequency correlation approach 124
6.3.3 Measurements and comparison 126
6.4 Important parameters of the model 129
6.4.1 Effective bandwidth 129
6.4.2 Chunks' pattern 130
6.4.3 Chunk width 131
6.4.4 Center frequency 134
6.5 Impact of the model on channel parameters 135
6.6 Conclusions 137

7 Application of UWB for Ranging in Dense Indoor Multipath Environments 139
7.1 Introduction 139
7.2 Range estimation methods 140
7.2.1 Time of Arrival estimation 140
7.2.2 Signal Strength estimation 143
7.3 Results and discussion 143
7.3.1 Time of Arrival estimation 143
7.3.2 Signal Strength estimation 147
7.4 Ranging based on partially measured frequency responses 148
7.5 Conclusions 149

8 Conclusions and Recommendations 151
8.1 Conclusions 151
8.1.1 UWB measurements 152
8.1.2 UWB channel modeling 153

8.1.3 UWB application for ranging 155
8.2 Recommendations 155

Bibliography **157**

List of Abbreviations **167**

List of Symbols **169**

Publications by the Author **173**

Samenvatting **177**

Acknowledgements **179**

Curriculum Vitae **181**

Chapter 1

Introduction

1.1 Introduction to UWB

The need for multimedia communications and new flexible communication capabilities with high data rates and high Quality of Service (QoS) becomes increasingly important. To fulfil these demands, advanced research in the field of communications, is needed. A new system based on so-called Ultra Wide Band (UWB) technology is gaining much attention to be used for communication and ranging due to its potential capabilities.

UWB technology has a history dating back to one hundred years ago when Guglielmo Marconi sent the first ever wireless transmission from the Isle of Wight to Cornwall on the British mainland using spark-gap transmitters [1–3]. Radio subsequently was developed to provide telephony services based on analogue techniques, and recently transited to digital telephony thanks to numerous technological advances. Through the years (1960s to 1990s) the United States military developed the UWB technology that was first used for ground penetrating radar [4].

Recently, the Federal Communications Commission (FCC) has recognized the significance of UWB technology and initiated the regulatory review process of the technology. As a result, UWB technology has been authorized for commercial use with different applications, different operating frequency bands and corresponding transmitted power spectral densities, as shown in Figure 1.1. According to the definition proposed by the FCC, an UWB signal is any signal which occupies a bandwidth larger than 500 MHz or has a fractional bandwidth larger than 0.20, [5].

This huge bandwidth allows a high capacity, processing gain and large number of users. It has also other desirable capabilities like accurate positioning and ranging, lack of significant fading, covert communications, and material penetration. Due to its bandwidth, UWB has to share the spectrum with other narrow-band

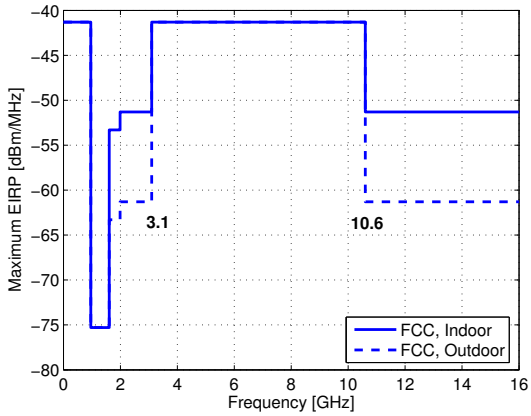

Figure 1.1: *UWB spectral mask.*

systems and may cause or suffer interference. Moreover, in the case in which UWB is implemented in base-band it neither requires an IF stage in the receiver nor transmitter, and no mixers are needed. Nevertheless, UWB systems require accurate synchronization.

The main techniques used to generate UWB signals [2] are: time modulated UWB (TM-UWB) and direct sequence UWB (DS-UWB). The former is based on the transmission of very short pulses while the second one is based on a technique similar to CDMA (Code Division Multiple Access). A pseudo-noise sequence is multiplied by an impulse sequence at a duty cycle approaching a sinusoidal carrier, providing spectrum spreading, channelization and modulation. However, there are other techniques to generate UWB signals that are not based on impulse transmission as for example multi-band orthogonal frequency division multiplexing (MB-OFDM) based on the aggregation of several narrow-band carriers.

1.2 Motivations and research questions

In this section, some important motivations related to the UWB channel characterization are given followed by research questions.

- The successful implementation of UWB transmission over wireless channels requires a good understanding of the propagation characteristics of the radio channel, which may vary from one environment to another. The UWB radio propagation mechanisms in indoor environments are complex. These signals propagating inside buildings undergo attenuation, reflection, refraction and diffraction. In general, because of these effects, the transmitted impulses ar-

rive at the receiver through various paths having different amplitudes, delays and phases. Usually pulse transmission results in delayed and attenuated echoes of each transmitted pulse, which in digital communication systems causes inter-symbol interference and eventually limits the transmission rate of the data. In addition to this, the received signal also suffers from noise and interference. That is why a designer of UWB communication systems must have an accurate UWB channel model to predict the signal coverage, to reach the maximum achievable data rate, to define the optimal location for the antennas [6], to design efficient modulation schemes, and to study associated signal-processing algorithms.

- Much work has been done to characterize indoor and outdoor communications channels for narrow- and wide-band channels [7]. The most useful and widely accepted models are grounded in reasonable theoretical frameworks and are verified by extensive measurement campaigns. General agreement of results and conclusions from different measurement campaigns further confirm the validity and reliability of a model for general scenarios. To date different measurement campaigns and channel modeling efforts have been carried out to characterize the UWB channel [8–18]. Accordingly, the following research question can be made:

  Research question 1: Are the available measurements sufficient for modeling the UWB channel for various environments?.

- According to the type of UWB applications, FCC has considered some factors in order to determine the frequency bands, which should be made available for UWB [5]. Because UWB is mainly introduced for indoor communication applications, the frequency band proposed by FCC for such environment is from 3.1 to 10.6 GHz. However, in the previous works, not all channel models were developed for this frequency band [8]. Therefore, it is more relevant to characterize the UWB channel for the whole frequency band (i.e. 3.1-10.6 GHz) and for this new channel measurements are needed. Performing UWB measurements over such large bandwidth may cause difficulties regarding the matching needed between the components in the set-up. In this respect, the following research question is given:

  Research question 2: Does mismatching within a measurement set-up affect the statistics of the UWB channel?

- Most reported results on UWB channel modeling as well as performance studies are based on the measurements in where the distances are from 1 to 20 m [10–12, 16]. On the other hand, UWB technology is prone to be used in many Wireless Personal Area Networks (WPAN) applications. In these applications transmit and receive antenna are very close to each other and the far-field condition assumed in most of the UWB models may not be satisfied. Under near-field conditions, variations in the link budget and

pulse shape compared to the far-field, might be observed. Therefore, more research and investigation are needed on to this subject which leads to the following research question:

Research question 3: How can the link budget for short-range UWB channels be modeled taking into account all different near-field aspects?.

- Although its large bandwidth makes UWB technology suitable for many applications, the development of new methods to characterize the technology is required. Thus, for instance, the measurement set-up for sounding the UWB band becomes complex, and hence more parameters must be taken into consideration. However, it is also noted that major parts of the UWB band with narrow widths have already been completely modeled and validated by extensive measurement campaigns [7]. Now, at this point, the following research question can be stated:

  Research question 4: How to make use of all available knowledge on narrow- and wide-band channels in order to estimate the UWB channel?".

- Radio signal propagation is usually affected by the characteristics of the antennas. For conventional narrow- and wide-band communication systems, the effect of the antenna can be well separated from the channel because the bandwidth is small and hence the antenna frequency response can be assumed as flat over this frequency band. However, this is not the case for UWB since the frequency response of the antenna is not flat over the entire bandwidth occupied by the UWB signal. This means that the antenna becomes an essential part of the channel and consequently more work is needed to investigate the effect of the antenna.

- Because of the large frequency band (3.1 to 10.6 GHz) devoted to UWB wireless communication in indoor environments, the wavelength remarkable changes (3 to 10 cm) over the whole band. However, propagation mechanisms (e.g. reflection, diffraction, scattering...) are frequency dependent for a channel with a large fractional bandwidth. Thus, channel parameters become frequency dependent. This aspect of wave interaction with a frequency dependent environment has to be incorporated in the modeling of the UWB channel.

- Positioning information in indoor environments is becoming more important and attractive especially for wireless ad-hoc networks and area-dependent services, logistics and emergency managing. Common navigation systems like the Global Positioning System (GPS) or Galileo are not designed to work in indoor environments. They do not operate with sufficient accuracy due to attenuation and the complicated environment, responsible for a lot of multipaths. UWB radio seems to be a prone solution for achieving such high accuracy. The extremely large bandwidth offered by UWB systems allows a fine time resolution of the multipath components of the received

signal. Accordingly, it is possible to reach an accurate range estimation when the time-of-arrival technique is used to detect the first path of the received signal. However, if the channel is dense this may influence the desired range accuracy which leads to the following research question:

Research question 5: Do UWB signals provide acceptable range accuracy in dense indoor multipath environments?.

- Due to the very large bandwidth occupied by the UWB signal, a high time resolution can be achieved which is attractive for scattering diagnostics.

  Research question 6: Is it possible to recognize the roughness in the scattering/reflecting objects using UWB radio technology?.

1.3 Research objectives

Generally, there are several methods to build a model for the UWB radio propagation channel. The first one is to solve mathematically the propagation equation of the channel, but the method is very computation-time intensive even with the use of a modern computer and limited to a specific environment. The second method is based on ray-tracing where radio wave propagation is approximated by "optical" wave propagation. This technique is not accurate enough for modeling of the UWB channel in indoor environments because of the frequency-dependent propagation mechanisms. Moreover, because of the wide bandwidth of the UWB signal, diffraction/scattering phenomena might be important for the propagation channel especially for lower frequencies. However, these effects are totally ignored when optical ray-tracing is used. The third one uses statistical methods to characterize the UWB radio channel. This method is mostly used because it describes the statistical behavior of the wireless channel taking different propagation environments into account in a statistical way.

The main objective of this thesis is to perform extensive UWB measurements and to develop a statistical model for the UWB channel for indoor wireless communications. To this end, a measurement setup for UWB channels has to be developed covering the frequency band 3.1 to 10.6 GHz. Based on the measured data, channel parameters statistics have to be extracted to complete the UWB channel model. In addition to this, the possibility of using known wideband channel models have to be studied for applicability in the UWB channel model. Investigation of problems faced in specific UWB very short-range applications (e.g. WPAN) is another goal of this thesis. For short-range applications as in WPAN, the UWB channel under near-field conditions has to investigated. At last, investigation of possible applications utilizing UWB technology with ranging capabilities is another objective of this thesis work.

1.4 Novelties and main contributions

The novelties of this thesis work can be categorized in terms of measurement campaign, channel modeling and applications.

Measurement campaign

- The most reported UWB measurement were performed using a frequency-domain technique due to its simplicity and high dynamic range. In this thesis, a new time-domain measurement set-up has been developed covering the frequency band from 3.1 to 10.6 GHz.
- Due to hardware limitations (e.g. length of acquisition time window, imperfections of the system, multiple antenna reflection), different solutions are proposed to overcome these limitations, implemented, tested and examined.
- The channel impulse response strongly depends on the physical channel in which the actual communication takes place. Therefore, in this thesis, based on various applications of UWB in indoor environments, different measurement scenarios such as for WPAN, UWB radio for outdoor to indoor and for an industrial area, have been considered to characterize the UWB channel.
- A sufficiently large set of measurements has been performed which provides for a good statistical characterization of the UWB channel (e.g. large-scale as well as small-scale fading and scattering phenomena).

Channel modeling

- Based on the measured data, a statistical model for the UWB channel is proposed. From this model the large-scale path-loss and shadowing effects, and small-scale fading are extracted.
- The already available UWB channel models are proposed for large distances (e.g.$>$ 1 m). In this thesis, a novel link budget model for short-range UWB channels is proposed and validated with measurements and simulations. This breakthrough provides link budget estimations for very short-range applications in e.g. WPAN, WBAN.
- Usually in the statistical modeling of the UWB channel, the whole UWB band is sounded. In this thesis, a new approach to estimate the wireless UWB channel is introduced where partial information of sub-band channels is available. This method requires less information, is less sensitive to narrow-band interference and is less antenna-dependent.

Applications

- Ranging in dense indoor multipath environment has been investigated utilizing UWB channel measurements.

1.5 Scope of the thesis

In Chapter 2, an overview of wireless indoor channels is given. In particular, conventional wireless channels are discussed. The multipath fading phenomena caused by the radio propagation mechanisms are explained. The impulse response of the mobile radio channel is introduced and relevant channel parameters are identified. Reported UWB measurements are reviewed and important issues missing in these measurements are identified and discussed.

Chapter 3 describes the measurement set-up needed to perform the UWB channel measurements. Due to hardware limitations (e.g. length of time window, imperfections of the system, multiple antenna reflection), different solutions are proposed to solve these problems. The measurement set-up is validated by comparing antenna gain results obtained in time-domain with those in frequency-domain as measured in an an-echoic chamber.

In Chapter 4, different measurement scenarios are described and data post-processing is explained. Based on the measurement data, a statistical propagation model for the UWB channel, which includes small-scale, large-scale and shadowing parameters, is proposed. Results on time dispersion are also presented followed by a general discussion on the modeling results.

In Chapter 5, a novel link budget model for very short-range UWB channels is proposed and validated with measurements and simulations. Particulary, the near-field effect is analyzed and its consequence on the UWB link budget is modeled.

Chapter 6 introduces a new approach for estimating an UWB channel based on partially measured sub-band channels within the UWB band.

Chapter 7 deals with the potential application of UWB radio with ranging capabilities. Different approaches to detect the time of arrival of the first multipath component are evaluated. Obtained ranging results using time-based estimation are compared to that of signal strength. The effect of bandwidth on range estimates is analyzed.

Finally, conclusions and recommendations are provided in Chapter 8.

Chapter 2

Wireless Radio Channel Overview

The signal paths from a radio transmitter antenna to a receiver antenna are called the radio channel. Some researchers include the antennas as part of the radio channel but in this thesis we consider it more appropriate to define the channel as the propagation medium.

A transmitted signal usually experiences the influence of several propagation mechanisms such as reflection, diffraction and scattering [19]. Due to these propagation mechanisms, the transmission between a transmitter and a receiver is achieved not only via a direct path or line-of-sight (LOS) but also via other paths. This non-line-of-sight (NLOS) phenomenon is called multipath propagation. So, each replica of the signal has traveled over different distances and thus has suffered from different amplitude attenuation, phase shift, and arrives with a different time delay. Because of the random nature of the radio channel, the received signals may add destructively or constructively. This phenomenon is referred to fading. In general, multipath fading in the mobile radio channel causes a limitation on the performance of wireless communication systems. Therefore, the characterization of the wireless channel is an important task during the design process of the mobile communication system [20].

This chapter gives an overview of the wireless channel. First, the mathematical model of the channel which can be described either in time- or frequency-domain is given. Then, useful parameters of such channel model needed for the system design are addressed. Finally, a literature survey of UWB channel measurements is provided.

2.1 Mathematical modeling of wireless channels

2.1.1 Time-domain (impulse response) modeling

The indoor radio propagation channel can be modeled as a linear time-varying filter with the following impulse response:

$$h(t,\tau) = \sum_{k=1}^{K} a_k(t)\delta(\tau - \tau_k(t))e^{j\theta_k(t)} \tag{2.1}$$

where τ is the delay, t refers to the impulse response at instant t and δ is the Dirac delta function transmitted at $t = 0$. The parameters of the kth path are a_k, τ_k, θ_k and K, i.e. amplitude, delay, phase and number of relevant multipath components, respectively. This mathematical model is a generalized model, which can be used to obtain the response of the channel to ***any*** transmitted signal $s(t)$ by convolving $s(t)$ with $h(t,\tau)$ and adding noise [7]. Three kinds of channels can be distinguished:

- narrow-band channel,
- wide-band channel,
- UWB channel.

For the narrow-band case, a signal with small bandwidth centered around a single frequency is used to excite the channel. A convenient model, which describes such a channel, can be expressed as:

$$Ae^{j\Theta} = \sum_{k=1}^{K} a_k e^{j\theta_k} \tag{2.2}$$

where A and Θ are the amplitude and phase of the received signal. From 2.2, due to the assumed narrow bandwidth, the corresponding channel model is based on the received power only (amplitude envelope). This means that only information about the signal power and fading statistics can be retrieved. Moreover, no information about the delay can be extracted because the duration of the signal is remarkably large compared to the path delay differences.

The model of 2.1 is mainly introduced to characterize wide-band channels. From wide-band channel measurements, different parameters can be determined: signal power, fading statistics as well as delay statistics. However, the same model can also be used for the characterization of the UWB channel. The main difference concerns the achieved time resolution, which is much higher in the UWB channel case. In order to determine the UWB channel characteristics, an UWB signal has to be used like a narrow pulse. For a base-band UWB signal, equation (2.1) can then be reduced to:

$$h(t,\tau) = \sum_{k=1}^{K} a_k(t)\delta(\tau - \tau_k(t)) \tag{2.3}$$

2.1.2 Frequency-domain modeling

Another approach for modeling of the UWB channel uses the frequency-domain Autoregressive (AR) model. The basic idea of AR modeling is that the frequency response $H(f_n)$ of the UWB channel at frequency $f = f_n$ can be modeled by an AR process. This model was first introduced by Howard et al. [21] for conventional wide-band channels and has been used later for UWB channel modeling by Ghassemzadeh [12]. The AR model has the advantage that it can statistically represent the UWB channel with a minimum number of parameters. Accordingly, the measured frequency responses can be regenerated in an easier way, important for computer simulation. The model can be expressed as:

$$H(f_n, x) - \sum_{i=1}^{p} b_i H(f_{n-i}, x) = V(f_n) \tag{2.4}$$

where $H(f_n, x)$ is the nth sample of the complex frequency response at location x, $V(f_n)$ is complex white noise, the complex constants b_i are the parameters of the model and p is the order of the model. Taking the z-transformation of equation (2.4), the AR process $H(f_n, x)$ can be viewed as the output of a linear filter with transfer function

$$G(z) = \frac{1}{\prod_{i=1}^{p} (1 - p_i z^{-1})} \tag{2.5}$$

excited by $V(f_n)$. With this method only p poles are required to characterize the frequency response of the UWB channel. The geometry of the poles is important. The delay associated with a pole is determined by the angle of that pole and the distance of a pole to the unit circle represents the power at the corresponding delay.

2.2 Channel parameters for system design

2.2.1 Power delay profile

When an UWB signal is sent through a multipath-fading time-invariant (static) channel, the average received power as function of excess time delay is called the power delay profile (PDP) and is defined as:

$$P(t) = h(t)h(t)^* = |h(t)|^2 = \sum_{k=1}^{K} a_k^2 \delta(t - t_k) \tag{2.6}$$

where * denotes the complex conjugate. However, in our case the transmitted pulse has a finite width. Then, the PDP can be calculated as follows. Suppose a narrow pulse $p(t)$ is used to excite the channel. Then the transmitted signal can be written as:

$$s(t) = p(t) \tag{2.7}$$

where $p(t)$ is the pulse at the transmit antenna output. The received signal is then the convolution of the transmitted signal with the channel impulse response:

$$r(t) = s(t) * h(t) \tag{2.8}$$

By assuming no phase distortion in the channel, we get:

$$r(t) = \sum_{n=1}^{K} a_k p(t - t_k) \tag{2.9}$$

The PDP is then calculated via:

$$P(t) = |r(t)|^2 \tag{2.10}$$

$$= \sum_{n=1}^{K} a_k^2 p^2(t - t_k) \tag{2.11}$$

2.2.2 Path loss, shadowing and fading

For developing a wireless communication system the radio engineer must know the radio propagation characteristics. A lot of measurements have been done to obtain information concerning propagation loss and spatial distribution of power when the environment is physically static. The effect of space variation on the channel, and consequently in the signal reception, are experienced by displacements of the antennas. So we can distinguish different results of these displacements, each having a different impact on the signal reception. Three types of signal variations can be distinguished: path-loss, shadowing and small scale fading.

Path loss: large-scale fading

Link budget calculations require an estimate of the power level so that a signal-to-noise ratio SNR at receive may be computed. Because mobile radio systems tend to be interference-limited (due to other users sharing the same radio channel) rather than noise-limited, the thermal and man-made noise effects are often insignificant compared to the signal levels of co-channel users. Understanding the propagation mechanisms in wireless systems is important not only for predicting the range coverage of a particular user, but also for predicting the interference that user will experience from other radio frequency (RF) sources. Path loss is defined as the ratio of the transmit signal power to the receive signal power. Path-loss $PL(d)$ generally increases exponentially with increasing distance d between transmitter and receiver [19]:

$$PL(d) \propto \left(\frac{d}{d_0}\right)^{\alpha} \tag{2.12}$$

where α is the path-loss exponent, d_0 is the reference distance (corresponding to a point located in the far-field of the antenna, usually $d_0 = 1$ m). The path-loss exponent indicates how fast the signal power is decaying as function of distance and usually it depends on the type of propagation environment. In logarithmic scale, equation (2.12) transforms into:

$$PL_{[dB]}(d) = PL_{[dB]}(d_0) + 10\alpha \log_{10}\left(\frac{d}{d_0}\right) \tag{2.13}$$

Shadowing effect

If many users are equally separated from the base station (i.e. they have the same separation distance) but situated at different locations, they do not always experience the same signal power as resulted from the large-scale fading model. Measurements show that this model is not realistic in some circumstances because the results obtained at various sites with the same antenna separation have shown that, by going from one receive position to the other, the received signal power can vary quite significantly. This slow signal fluctuation is known as shadowing due to the presence of large-scale (fixed) obstacles in the propagation path of the radio signal. The nature of the terrain surrounding the base station and the mobile terminal as well as the antenna heights determine the shadowing behavior. Researchers have found that a good agreement of signal power variations around the average path-loss can be obtained with the lognormal distribution (i.e. Gaussian distribution in logarithmic scale) [7, 22, 23]. So, the shadowing effect is usually modeled as a lognormal random process, meaning that the path-loss model can be described by:

$$PL_{[dB]}(d) = PL_{[dB]}(d_0) + 10\alpha \log_{10}\left(\frac{d}{d_0}\right) + X_\sigma \tag{2.14}$$

where X_σ is a zero-mean Gaussian random variable in logarithmic scale with a standard deviation σ.

Small-scale fading

Multipath channels cause signals with fading due to constructive and destructive interference between replicas of the transmitted signal. Because the wavelength of the RF signal is in the order of cm's, small movement can produce phase shifts of individual multipath components that result in large variations in their coherent sum. Such fading refers to small-scale variations that occur over very small distances and small time intervals. Usually the displacement over a portion of a wavelength can also lead into a dramatic change in the relative phases of path signals. Consequently, after superposition of all path signals, it affects the resulting overall received signal.

2.2.3 RMS delay spread

The rms (root mean square) delay spread is a good measure of delay spread in the received multipath signals and is defined as the second moment of the PDP:

$$\tau_{rms} = \sqrt{\overline{\tau^2} - (\overline{\tau})^2} \tag{2.15}$$

where $\overline{\tau}$ and $\overline{\tau^2}$ are the first and second moments of the power delay profile respectively. They are are defined as:

$$\overline{\tau^\beta} = \frac{\sum_n a_n^2 \tau_n^\beta}{\sum_n a_n^2} \tag{2.16}$$

where a_n, P_n, and τ_n are the amplitude, power and delay characteristics, respectively. This moment parameter is a compact powerful description of the channel because it affects the most important properties of the communication system. The mean rms delay spread value has been introduced as a parameter that determines the frequency selectivity of the fading in a channel [24, 25]. This frequency selective fading, caused by multipath time-delay, degrades the performance of digital communication systems over radio channels. In fact, some earlier research indicated the relationship between the rms delay spread and the maximum data transmission rate, which can be reliably supported by the channel under investigation. In the case without using frequency/space diversity or equalization, the rms delay spread is inversely proportional to the maximum usable data rate R_{max} of the channel where

$$R_{max} = \frac{1}{\nu \tau_{rms}} \tag{2.17}$$

and $\nu \approx 4$ as extracted from literature [26].

2.2.4 Correlation

Wireless communication systems usually suffer from multipath fading caused by propagation mechanisms due to obstacles in the channel. To combat this problem, techniques like frequency and space diversity can be used. Such techniques are more efficient in the case where the received signals are independent, but if the received signals are correlated, this leads to a limitation on performance improvement of the system by using diversity [27]. Two types of correlation can be distinguished: amplitude correlation and time correlation. The first one is the correlation in the amplitude between adjacent multipath components collected at the same profile and is defined as:

$$\rho(\Delta\tau_i) = \frac{E\left([a_{n+1} - E(a_{n+1})]\,[a_n - E(a_n)]\right)}{\sqrt{var(a_{n+1})var(a_n)}} \tag{2.18}$$

where $E(.)$ is the expected value, $var(.)$ is the variance, a_n and a_{n+1} denotes the path amplitude at delay τ_n and τ_{n+1}, respectively. The amplitudes of adjacent

multipath components of the same delay profile are likely to be correlated since a number of scattering objects that produce the multipaths with tightly different delay can be approximately the same and they have traveled over nearly the same path length. However, the second type of correlation is the correlation between arrival times of multipath components $\Delta\tau$ caused by the grouping property of local structures. This time correlation is explained in the next section.

2.3 Models for channel parameters

2.3.1 Path amplitude models

For describing the statistics of amplitude fading, a number of distributions exist. Extensive field trials in the past have been used to validate these distributions, and the results show a good agreement between measurements and theoretical models. In the following some important distributions are given.

Rayleigh distribution

In mobile radio channels, the Rayleigh distribution is the most accepted model for small-scale rapid amplitude fluctuations in absence of the LOS component. The probability density function (PDF) is given by:

$$f(x) = \frac{x}{\sigma^2} \exp\left(-\frac{x^2}{2\sigma^2}\right) \tag{2.19}$$

where σ is the rms value of the received signal voltage, and σ^2 is the time-averaged power of the received signal. The mean and variance of Rayleigh are $\sigma/\sqrt{\pi/2}$ and $\sigma(2-\pi/2)$, respectively.

Ricean distribution

In contrast to the Rayleigh distribution, the amplitude fluctuations should be modeled by the Ricean distribution when the LOS component is present. The PDF is:

$$f(x) = \frac{x}{\sigma^2} \exp\left(-\frac{x^2+A^2}{2\sigma^2}\right) I_0\left(\frac{Ax}{\sigma^2}\right) \tag{2.20}$$

where A is the LOS component amplitude and I_0 is the zero-order modified Bessel function of the first kind expressed as:

$$I_0(x) = \frac{1}{2\pi} \int_{-\pi}^{+\pi} e^{x\cos\Phi} d\Phi \tag{2.21}$$

Usually, a parameter called Rice factor K_{rice} is introduced to describe the Rice distribution, and is defined as:

$$K_{rice} = \frac{A^2}{2\sigma} \tag{2.22}$$

For the special case with $A = 0$, the Ricean distribution becomes the Rayleigh distribution.

Log-normal distribution

This distribution characterizes the large-scale variations of the signal amplitude in fading environments with obstructions. The PDF is given by:

$$f(x) = \frac{1}{\sigma x\sqrt{2\pi}} \exp\left[-\frac{(\ln x - \mu)^2}{2\sigma^2}\right] \tag{2.23}$$

where $\ln(x)$ has a normal (Gaussian) distribution, and the parameters μ and σ are the mean and variance, respectively.

Nakagami distribution

This distribution is also called the m-distribution and contains many other distributions as special cases. Its PDF is given as:

$$f(x) = \frac{2m^m x^{2m-1}}{\Gamma(m)\Omega^m} \exp\left[-\frac{mx^2}{\Omega^2}\right] \tag{2.24}$$

where $\Omega = E[x^2]$, $m = \left[E(x^2)\right]^2 / var(x^2) \geq 0.5$, and $\Gamma(.)$ is the Gamma function defined as:

$$\Gamma(m) = \int_0^\infty t^{m-1} \exp(-t) dt \tag{2.25}$$

The Nakagami distribution reduces to the Rayleigh distribution for $m = 1$.

Weibull distribution

The pdf of this distribution is written as:

$$f(x) = \frac{\beta}{b}\left(\frac{x}{b}\right) \exp\left[-\left(\frac{x}{b}\right)\beta\right] \tag{2.26}$$

where β and b are the shape and scale factors, respectively. The distribution reduces to the exponential distribution for $\beta = 1$, and to the Rayleigh distribution for $\beta = 2$.

2.3.2 Path arrival time models

In literature the so-called excess delay axis is mostly used instead of just the delay axis. It means that the delays are measured taking the delay τ_0 of the first arriving echo as reference, where $\tau_0 = 0$. The reason for this excess delay is that the delay of the first component, the LOS path (if it exists), is not random, since it depends directly on the distance between transmitter and receiver [19]. The most important models for the arrival times are presented in the following.

Standard Poisson model

This model is based on the assumption that the arrival times (in terms of excess delay) follow a Poisson distribution. In this distribition, the probability of l arriving paths within an interval of T seconds is given by the expression [28]:

$$P(L = l) = \frac{\mu^l e^{-\mu l}}{l!} \tag{2.27}$$

where $\mu = \int_T \lambda(t)d(t)$ is the Poisson parameter, and $\lambda(t)$ is the mean arrival rate at time t. Another distribution related to the arrival time sequence is the inter-arrival time sequence, defined as the difference between two successive arrival paths where $x_i = \tau_i - \tau_{i-1}$. For a standard Poisson process, the differences are exponentially distributed:

$$f(x) = \lambda e^{-\lambda x} \tag{2.28}$$

However, results obtained from measurements, characteristic for several indoor environments, have established the inadequacy of the Standard Poisson process to model the time of arrival sequence [29]. This inadequacy is probably due to the fact that scatterers inside a building (causing multipath dispersion) are not randomly located. Patterns in their location give rise to deviations from a standard Poisson model, which is based on purely random arrival times [29].

The Δ-K model

Since the standard Poisson process does not closely match the results of the empirical measurements at some locations, a second-order model has been suggested. The idea behind this model is to make profit of the clustering properties of the channel, i.e., that the paths arrive in clusters, probably reflected by the same closely spaced scatterers.

The model tries to create the correlation between radio wave arrivals by means of two parameters, K and Δ [29]. As we can see in Figure 2.1, the model has two states: S1 and S2. The first is the initial state, where the mean arrival rate of the paths is $\lambda_0(t)$. As soon as a path reaches the receiver, the process makes a transition to state S2, where the mean arrival rate is $K\lambda_0(t)$. If no path arrives in the next Δ seconds, then the process comes back to S1. However, if a path arrives at time t' before the interval is out, then it is restarted. The model can therefore

be described by a series of transitions between the two states. If the parameter $\Delta = 0$ or $K = 1$, the model reverts to the standard Poisson process. For $K > 1$, an incidence of a path at time t increases the probability of receiving another path in the next Δ interval (i.e., the process shows a clustering property). On the other hand, if $K < 1$, the probability of a path occurrence in the Δ seconds after a path arrived at time t is decreased (i.e., the paths arrive more evenly than in a standard Poisson process) [29].

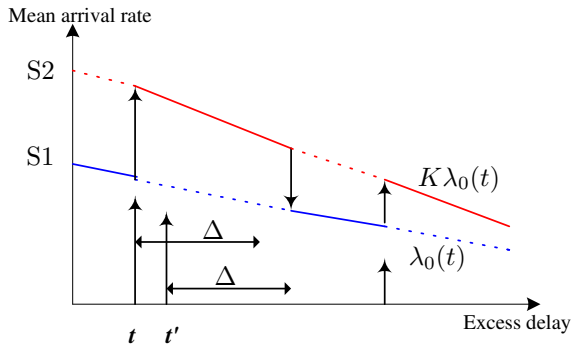

Figure 2.1: *Continuous time modified Poisson process.*

The model of Figure 2.1 has not exactly been used in the real characterization of the wideband channel. A discrete-time version has been implemented to model the indoor environment. The results obtained in two dissimilar office buildings show that the fit was good [7]. Most observed optimal K values were less than 1, i.e., the paths occurrences are more evenly distributed than a standard Poisson model.

2.3.3 PDP models

The behavior of the averaged received power as function of excess time delay follows mostly an exponential decreasing function since the later paths of the profile experience more attenuation after traveling over larger distances [7]. However, for indoor environments another model is introduced based on measurements [30,31]. This model refers to the double exponential model based on clustering, i.e., the received components arrive in clusters, in terms of arriving angles and delays. In Figure 2.2 a scheme showing the double exponential model is presented. T_l refers to the arrival time of the first path in the lth cluster, $\tau_{n,l}$ refers to the arrival time of the nth path in the lth cluster and Γ and γ are the ray and cluster time decay constants of the power delay profiles, respectively.

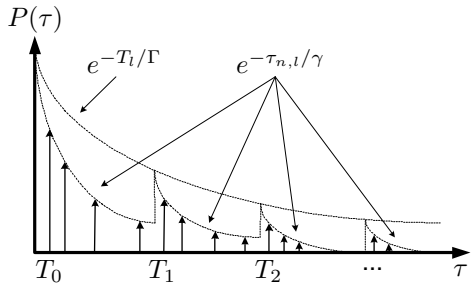

Figure 2.2: *Power delay profile showing the double exponential model.*

2.4 Literature survey of UWB channel measurements

Due to an increasing interest of UWB technology for wireless communications as well as for positioning, much effort is devoted by many researchers for developing reliable and accurate channel models to be used for simulation purposes. To this end, different UWB measurements have been carried out. However, these measurements are still limited when compared to narrow-band and wide-band measurements [7,21,29,32–36]. A detailed comparison between UWB and narrow- and wide-band channel parameters is given in [8]. One of the main issues between both measurements is that UWB pulse measurements are antenna dependent meaning that the measurements are affected by the antenna characteristics [18].

The most known UWB measurement campaign is performed by the Ultra Lab group at the University of South California (USC), in collaboration with the Time Domain Corporation [9, 37]. These measurements were performed in time-domain using a sampling oscilloscope, a pulse generator and wide-band antennas. The obtained results were used to develop further models [10, 11]. However, no information on the pulse shape and antennas characteristics as used in their measurements have been provided. The pulse width was about 1 ns covering the lower frequency band only (up to 1 GHz). However, the propagation mechanisms in indoor environments are frequency dependent which means that the proposed model might not be valid for the frequency band proposed by the FCC (from 3.1 to 10.6 GHz). The UWB measurements over the lower frequency band (up to 1 GHz) may suffer from active narrow-band systems (e.g. TV station) which dramatically degrades the signal to noise ratio. Additionally, the measurement results covered only large distances from 7 m to 17 m considering only NLOS propagations. Other time-domain UWB measurements which use a narrow pulse (i.e. 85 ps rise-time) and cover a large frequency band were presented in [38]. However, only large-scale path-loss and time dispersion parameters have been addressed. The same set-up has been used to characterize different materials for indoor environments [39].

Characterization of the UWB channel propagation using frequency-domain measurements is reported in many papers [12, 14–16, 40]. Measurements of [12] were performed in 23 residential homes in the Unlicensed National Information Infrastructure (UNII) band. The bandwidth in their measurements was limited only to 1.25 GHz centered at a frequency of 5 GHz. Both time-domain and frequency-domain models have been proposed [41, 42]. The measurements of [16] and [43] were conducted over a large frequency band 1-11 GHz and 3-10 GHz, respectively. In both references it has been observed that the channel gain tends to decrease with frequency. It is noted that all results account for frequency dependent antenna characteristics.

So far, all UWB measurements have been conducted in indoor office/home environments. However, other environments may also be attractive for UWB like industrial areas and wireless personal area networks (WPAN). To our understanding, only one measurement campaign has been performed in an industrial area [44]. Thus, more measurements in such environments are needed. With respect to WPAN applications, many UWB measurement results have been reported [40, 45–55]. In [46], the human body effect on UWB signal propagation has been investigated, but only for the receive antenna near the body and the transmit antenna in the far-field. In [47], UWB channel measurements for a Body Area Network (BAN) are presented where transmit and receive antenna are placed directly on the body; here only the 3-6 GHz band was measured. In all measurements, the far-field conditions of the antennas have been assumed which may not valid as the antennas can be close to each other. Thus, in spite of a significant number of measurement efforts for short-range UWB applications, the analysis of many effects related to short-distance propagation, e.g. near-field effects, has not received much attention.

In summary, there still exist many unresolved issues and hence more UWB propagation measurements are needed. Different measurement conditions, insufficient measurement data, and the effect of other excitation pulses are among the priority issues that demand additional measurements in order to develop robust models for different environments before designing simulators.

Chapter 3

Measurement Set-up for UWB Channel Characterization

Design and implementation of UWB transmission systems require a good understanding of the propagation characteristics of the radio channel. Different ways exist to characterize this channel. A major method is to use statistical approaches based on measurements. To perform UWB channel measurements, different techniques can be used. The main difference in various channel sounders is the signal used to excite the channel. The overall concept of such techniques is to probe the channel with a suitable (i.e. UWB) signal in order to obtain an estimate of its impulse or frequency response, which can in turn provide most important channel information.

The frequency band devoted to UWB wireless indoor communications is from 3.1 to 10.6 GHz. So it might be relevant to characterize the UWB channel for this whole frequency band. This may provide the advantage of using the measured channel data to propose different statistical channel models associated to whatever selected portions within this frequency band. However, measuring the channel over this large frequency band requires the development of a powerful and reliable measurement set-up.

This chapter describes the set-up used to perform UWB measurements needed to characterize the UWB channel covering the whole frequency band of interest. For instance, two possible channel sounding techniques (i.e. frequency- and time-domain) for UWB channel measurements are reviewed. The time-domain measurement set-up is given and important related parameters are described. The performance of the developed set-up is discussed. Here we also introduced new methods for measuring larger acquisition time windows which may be useful for time-domain measurement techniques.

3.1 Measurement sounding techniques

Channel characterization can be achieved by performing measurements in time-domain (TD) or frequency-domain (FD). In this section, the two techniques are discussed.

3.1.1 FD technique

In this technique, a vector network analyzer, controlled by a PC (personal computer), is used to control in turn a synthesized frequency sweeper, and an S-parameter test-set to measure the complex frequency response of the channel. Clearly, the bandwidth centered around the frequency of interest is scanned by the synthesizer through discrete frequencies with equal frequency spacing as shown in Figure 3.1. The parameters f_c, f_{min}, f_{max}, Δf_s and B_w are the center frequency, the minimum frequency, the maximum frequency, the spacing between two adjacent measurement frequencies and the bandwidth, respectively.

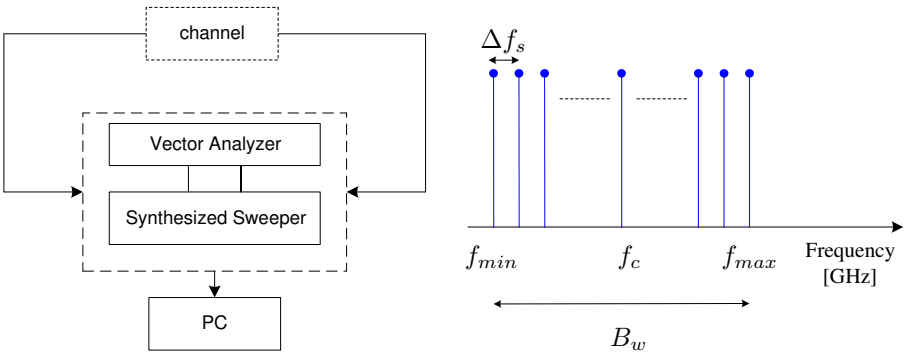

Figure 3.1: *Illustration of the FD measurement set-up.*

For each frequency sample a sine-wave signal is transmitted and information about the magnitude and phase of the received signal is obtained. The channel impulse response can be obtained using the inverse fast Fourier transform (IFFT). The scanned bandwidth and the frequency spacing determine the multipath resolution of the measured impulse response. From multipath resolution we distinguish: spatial resolution and maximum unambiguous echo-path time-delay resolution [56]. The former is a measure of the minimum discernible path length difference between two consecutive echo contributions and the last one ensures that all multipath components are received. The bandwidth determines the spatial resolution as:

$$\Delta d = c \cdot \tau_{res} \approx \frac{c}{B_w} \tag{3.1}$$

where τ_{res} is the resolution in time delay and c is velocity of light. As the frequency

band of interest is 3.1-10.6 GHz, the spatial resolution that can be achieved is about 4 cm, i.e. $\tau_{res} = 134$ ps. It should be noted that before performing the IFFT to obtain the channel impulse response, the frequency response has to be windowed first to reduce the side-lobes [57]. The type of window applied influences the echo-path resolution and hence its effect on the UWB channel parameters has been investigated in [58]. The maximum unambiguous echo-path time-delay resolution τ_{un} is determined from the frequency spacing as:

$$\tau_{un} = \frac{1}{\Delta f_s} \tag{3.2}$$

3.1.2 TD technique

This technique employees a narrow pulse to probe the channel. Thus, the received signal is the convolution of the sounding pulse with the channel impulse response. The technique is based on the so-called stroboscopic sampling principle of the measured pulses. In other words, a number of pulses are sent in order to recover one impulse response. The main parts of a such measurement system are an oscilloscope controlled by a PC, a sampling unit and a pulse generator as shown in Figure 3.2. The sampling oscilloscope controls the sampling unit and the pulse generator with trigger pulses. The sampling unit receives a sequence of waveforms with a certain repetition rate and it takes one sample per waveform. The time difference between two successive samples is equal to the pulse repetition interval T_{PRI} plus a slight time displacement Ts (i.e. sampling time). Figure 3.3 illustrates the stroboscopic sampling principle using number of samples N_s to get one reconstructed pulse. The time needed for a single measurement is:

$$t_{meas} = N_s T_{PRI} \tag{3.3}$$

For the TD technique, the spatial resolution depends on the rise time of the transmitted pulse and the maximum unambiguous echo-path time-delay resolution is equal to T_{PRI}.

3.1.3 TD versus FD technique

It should be emphasized that there is in principle no difference in the channel characterization using TD or FD set-up. However, when making a decision on the technique to be used some trade-offs should be taken into consideration. In the following a comparison between the two techniques is provided.

One of the advantages of the TD technique is that it requires only a single measurement where as the FD technique requires frequency sweeping, which involves measurements at different discrete frequencies. Thus, sounding the channel using the TD set-up requires a relatively simple implementation. Another advantage is that the recorded signal waveform using the TD technique immediately gives a physical insight into the channel characterization problem, whereas for the

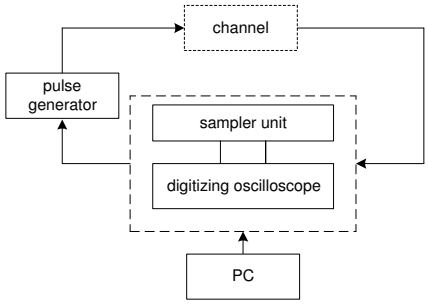

Figure 3.2: *Illustration of the TD measurement setup.*

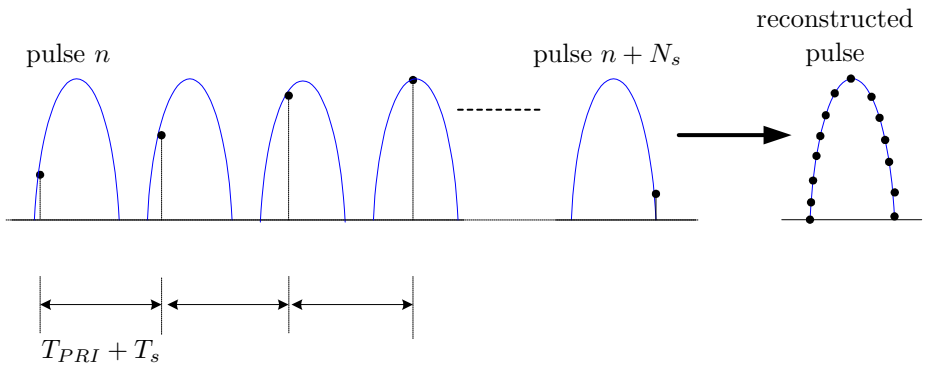

Figure 3.3: *Illustration of the stroboscopic sampling principle.*

FD technique, calculations have first to be performed by the user to visualize the actual TD signal.

A limitation of the TD technique is that the method is more susceptible to noise when compared to the FD technique. This is because in the FD technique the measurements are performed over narrow-band frequencies which easily allows the use of a wide variety of noise reduction algorithms [59]. Clearly, typical measurements that provide low noise results are designed for continuous signals rather than for transient signals. Another limitation of the TD technique is that the measurement range is limited by the characteristics of the pulse generator. Moreover, the TD technique needs a careful synchronization because any time jitter that exists in the system will lead to a variation in the measured signal reducing the measurement quality especially for large distance measurements (the trigger pulse may suffer more attenuation and dispersion) [59].

The FD technique has the advantage of improving the signal to noise ratio

and hence provides a large dynamic range (i.e. high sensitivity). For the TD measurement, the transmitted pulse compromises the dynamic range. Since the spectrum of the transmitted pulse is not uniform over all frequencies (usually the spectrum decreases with frequency), the signal to noise ratio for higher frequencies is limited which causes measurement difficulties. FD measurements are performed using a discrete frequency sweep, and hence the amount of transmitted power for each frequency is almost uniform with respect to the system noise. Drawbacks of the FD technique are a careful calibration and highly-accurate synchronization. It turns out that the transmit and receive antennas must physically be connected to the network analyzer making long distance measurements difficult.

3.2 The measurement set-up

The UWB channel measurements presented in this thesis are performed using the TD measurement technique. This technique is mainly chosen because the equipment to perform such UWB channel measurements is available in our IRCTR (International Research Center for Telecommunications and Radar). The set-up consists of two main parts: the transmitter and receiver. The transmitter sub-systems are the pulse generator, pulse shaper, resistive coupler and transmit antenna. The receiver sub-systems are the same antenna type, band-pass filter, wideband resistive attenuator, broadband Low Noise Amplifier (LNA), sampler unit, sampling oscilloscope and PC. Using a GPIB (General Purpose Information Bus), the measured time signal is transferred to a PC where the data is stored for later processing and analysis. The whole measurement set-up is depicted in Figure 3.4. In the following paragraphs, a detailed description of the set-up parameters is given.

3.2.1 Sampling oscilloscope

- **Frequency range of the measurements**
  The sampling oscilloscope can measure four channels simultaneously:
  - 2 channels up to 6 GHz,
  - 2 channels up to 18 GHz.

  This means that the system is suitable to carry out measurements until 18 GHz, which satisfies the requirement regarding the frequency band of interest. The important characteristics of the sampling oscilloscope are given in Table 3.1.

- **Measurement range**
  The pulse generator has a repetition rate of $PRF = 100$ kHz. This means that the unambiguous range R_{un} is equal to:

$$R_{un} = cT_{RPI} = c\frac{1}{PRF} = 3\,\text{km} \tag{3.4}$$

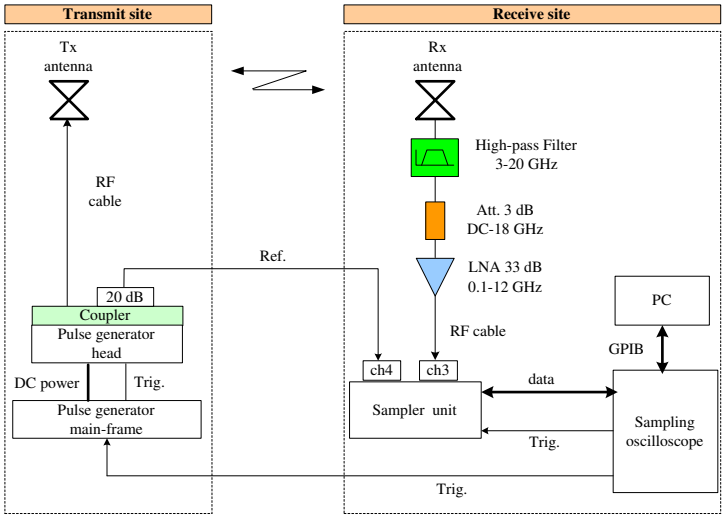

Figure 3.4: *The time-domain measurement set-up [60].*

The maximum excess delays for indoor propagation entwinements are ranging from 70 ns to 300 ns as reported in [10, 14, 16, 17]. The R_{un} value of 3 km is therefore more than large enough and allows to record all multipath components for indoor environments. It should be noted that the system has two trigger outputs: "1" and "2". The measurement range is 10 μs if trigger "1" is used and 40 ns for trigger "2". This means that trigger "1" has to be used. The time needed for a single measurement is the number of samples times the pulse repetition interval, i.e. measuring a waveform with 1024 samples takes 10 ms. If also an averaging of 256 is used, the measurement time then becomes 2.56 s.

- **Sampling time**
  The maximum frequency to be measured is 10.6 GHz. According to the Nyquist criterion the minimum sampling frequency f_s has to be:

$$f_s = 2f_{max} = 21.6\,\text{GHz} \tag{3.5}$$

This corresponds to a minimum sampling time T_s of:

$$T_s = \frac{1}{f_s} \approx 47\,\text{ps} \tag{3.6}$$

As a trade-off between accurate pulse shape reconstruction and obtaining a large time window, a sampling time of 10 ps (oversampling of 5 times) was considered for the measurements.

Table 3.1: *The characteristics of the sampling oscilloscope [61, 62].*

Parameters	**Value**
Number of channels	4
Bandwidth	2 x (1-6 GHz) 2 x (1-18 GHz)
Noise (RMS)	$\pm$ 1.0 mV (1-6 GHz) $\pm$ 4.0 mV (1-18 GHz)
Max. input voltage	$\pm$ 1.0 V
Voltage measurement accuracy	$\leq$ (0.02 V_x + 0.002) [V]
A/D converter	12 bit
Number of samples	256, 512, 1024
Max. averaging	256
Minimum sampling time	0.1 ps (10 ps used)
Jitter	$\leq$ 2.0 ps
Measurement range	10 ps - 10 μ s

- **Time window**
  The total delay due to all RF cables and the propagation between the transmit and receive antennas (free space propagation) is important for the determination of the time window. The position and width of the time window depends on the settings of the sampling oscilloscope.

  The parameter time delay defines the start (t_{start}) of the time window as shown in Figure 3.5 while the width TW of the time window is equal to:

$$TW = (N_s - 1)T_s \tag{3.7}$$

  Usually, the number of samples N_s is limited, in our case equal to 1024. Thus, the maximum width of the time window, which can be achieved, is 10.23 ns. This value does not satisfy the requirements for measuring the full range of most UWB channel responses of interest. Therefore, two solutions have been investigated and also implemented.

  - ***Setting the generator delay***
    The main idea is that the generator must have the capability to generate the pulse with several delays. In our case, 12 delay pulse positions

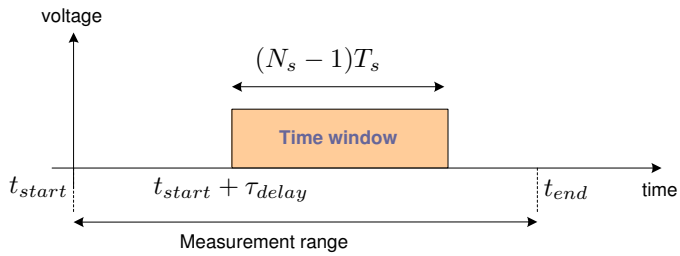

Figure 3.5: *Placement of time window in the measurement range.*

each separated over 10 ns can be obtained from the generator as shown in Figure 3.6. The delay between two successive pulses has to be less than the time window otherwise we miss some part of the channel response. This is why a high accuracy is required for the generation of the delay between the pulses. The frequency response of each pulse for a given delay has to be identical. The measurement method is illustrated in Figure 3.7. It is suggested to start with the highest generator delay (in our case 110 ns) and go down to 0 ns with steps of 10 ns. Clearly, the initial delay in the oscilloscope is set for a measurement at a certain start location using 110 ns generator delay. The pulse corresponding to this delay position is then generated and transmitted. A first time window can so be measured. After that the pulse is generated according to the next delay (i.e. $110 - 10 = 100$ ns) and we measure the next time window. This is repeated until 0 ns generator delay is archived. Because different pulse delay positions have to be used for one whole measurement, the pulse generator should be automatically controlled. In our case the generator communicates with the PC via an RS232 protocol. However, the length of the RS232 cable is a limitation and hence defines the maximum distance. From pilot measurements the critical length of the cable was found to be about 9 m, which is too short. Therefore, another solution has been introduced.

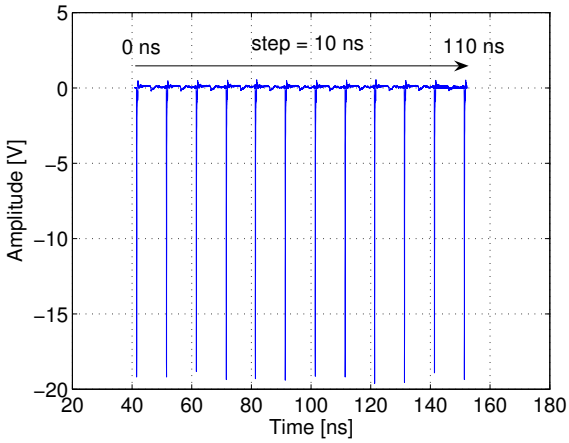

Figure 3.6: *Measured pulse at different delay positions.*

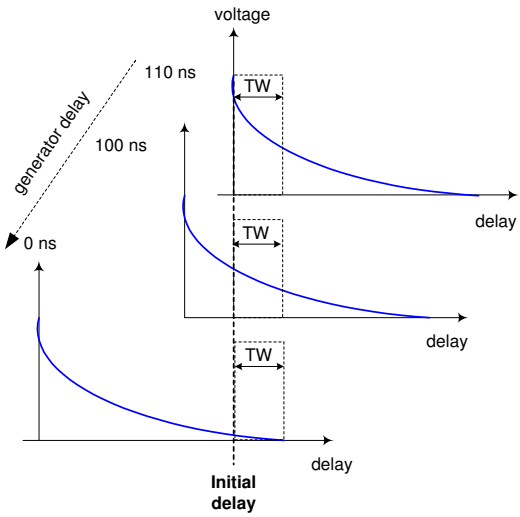

Figure 3.7: *Illustration of setting the generator delay.*

- ***Setting the oscilloscope delay***

  Software has been developed which allows automated measurements for larger maximum delays. The principle is illustrated in Figure 3.8. First, the initial delay τ_0 of the oscilloscope is set and a series of measurement is performed. According to the number of samples and sampling time, the time window is computed. After this, the various delays τ_i are set according to the old delay τ_{i-1} plus TW as:

$$\tau_0 = \tau_{initial}$$

$$\tau_i = \tau_{i-1} + (N_s - 1)T_s \tag{3.8}$$

  Further, we repeat the measurement until the desired maximum delay is achieved. In this case, any maximum delay can be set. The total signal is then reconstructed by cascading several measurement parts associated with successive time windows. The time between adjacent windows is important and hence the accuracy of the delay of the oscilloscope. However, because the setting of the delay in the oscilloscope is not exact, we may miss some information about the channel, especially around the edges of the time windows. Therefore, a time-framing has been implemented so that adjacent time windows overlap each other as illustrated in Figure 3.9. The new delay τ_i is set according to the old delay τ_{i-1}, time window and Overlap Time Interval OTI parameter as follows:

$$\tau_i = \tau_{i-1} + (N_s - 1)T_s - OTI \tag{3.9}$$

  After reconstruction of the signal, the autocorrelation function method is used to estimate the delay error associated to the oscilloscope accuracy and compensated using the cross-correlation between the signals coming from two successive time windows. This is illustrated in Figures 3.10 to 3.12. The method of setting the oscilloscope has the advantage that the number of time windows to be measured is not limited. It means that large maximum delays of the channel can be achieved. To validate this method, a number of measurements have been performed. We selected for testing an OTI of 1.23 ns (i.e. almost 12% of the time window). In order to obtain a total time window of 120 ns, 14 measurements are then needed. The obtained results show that the accuracy of the delay does not exceed 300 ps in all measurements.

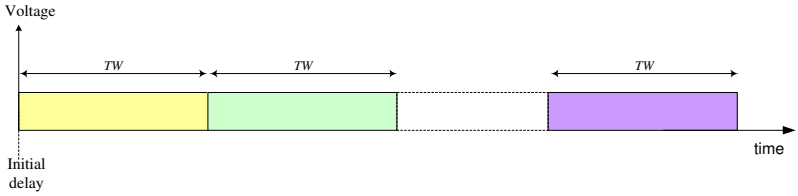

Figure 3.8: *Illustration of setting the oscilloscope delay.*

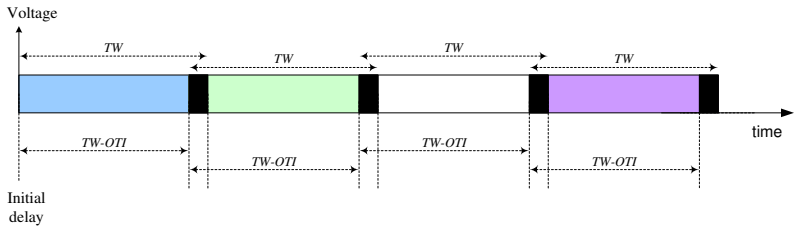

Figure 3.9: *Illustration of the overlap time interval method.*

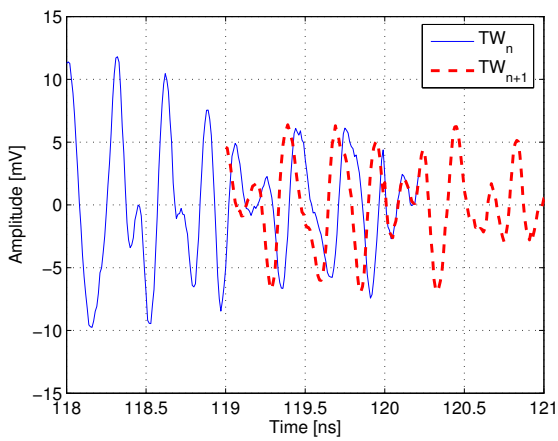

Figure 3.10: *Delay error between measured successive time windows.*

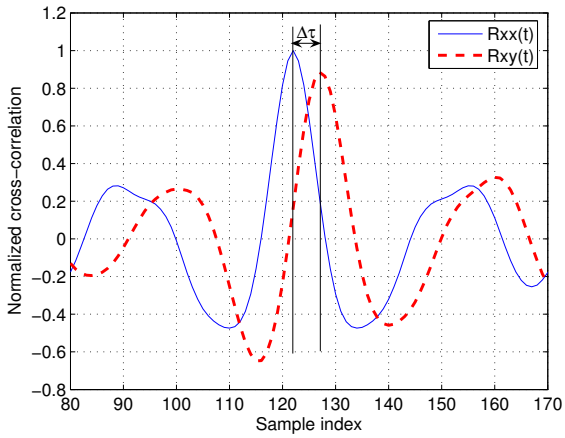

Figure 3.11: *Estimated delay using the cross-correlation method, sampling time of 10 ps was used.*

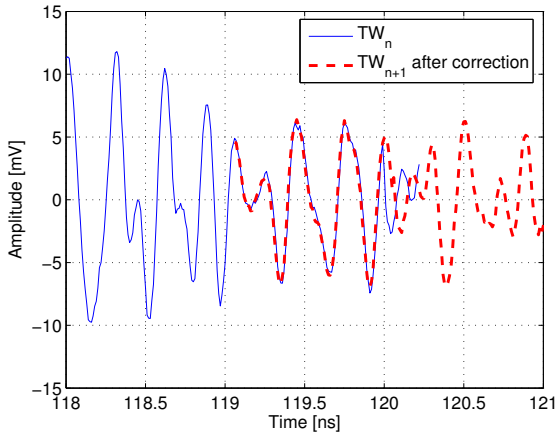

Figure 3.12: *Reconstructed signal after delay error compensation.*

- **Dynamic range**
  The dynamic range of the measurement system is defined as the difference between the strongest and the weakest resolvable echoes. The dynamic range depends on the sensitivity of the receiver. This sensitivity specification indicates how well a receiver will capture weak signals. It is a key specification because it directly affects the range of the system as demonstrated in the following example. We assume that the average received power $P(\tau)$ as function of the channel time delay τ can be expressed as:

$$P(\tau) = P_0 e^{-\frac{\tau}{\gamma}} \tag{3.10}$$

where P, τ and γ are the power, the delay and the time decay constant, respectively. The total received power yields:

$$\begin{aligned} P_{total} &= \int_0^{\infty} P_0 e^{-\frac{\tau}{\gamma}} d\tau \\ &= \frac{P_0}{\gamma} \end{aligned} \tag{3.11}$$

and the not-detected power becomes:

$$\begin{aligned} P_{no-det} &= \int_{T_{max}}^{\infty} P_0 e^{-\frac{\tau}{\gamma}} d\tau \\ &= \frac{P_0}{\gamma}^{-\frac{T_{max}}{\gamma}} \end{aligned} \tag{3.12}$$

We define the power error as:

$$\varepsilon_{error} = \frac{P_{no-det}}{P_{total}} \tag{3.13}$$

Inserting equations (3.11) and (3.12) in equation (3.13) we get:

$$T_{max} = -\gamma \ln(\varepsilon_{error}) \tag{3.14}$$

The reported time decay constant for diffident propagation environments was found to be in the range of 40 ns [10]. If we assume that the not-detected power must not exceed 5% of the total received power, then the maximum excess delay is equal to:

$$T_{max} = -40 \ln(0.05) = 120 \text{ ns} \tag{3.15}$$

This means that the selected time window has to be larger than 120 ns. The dynamic range can then be determined as:

$$DR = \frac{P_{max}}{P_{min}} = \frac{P_0}{P_0 e^{-\frac{T_{max}}{\gamma}}} = 20 \text{ dB} \tag{3.16}$$

Thus the minimum dynamic range has to be 20 dB [1]. According to Table 3.1, the maximum peak-to-peak voltage at the sampler input equals 2 V, and the maximum rms noise (i.e. quantization noise) of the oscilloscope is about 4 mV. The dynamic range at the receiver equals:

$$DR = \frac{P_{max}}{P_{min}} \tag{3.17}$$

where:

$$P_{max} = 20\log_{10}(2) = 6\,\text{dB} \tag{3.18}$$

and

$$P_{min} \approx P_{noise} = 20\log_{10}(4\,10^{-3}) = -48\,\text{dB} \tag{3.19}$$

Thus, a dynamic range of at most 54 dB can be achieved. This value satisfies the requirement of the dynamic range; however, it is still low when compared to values reported in the literature. In order to lower P_{noise} and so to improve the dynamic range averaging over maximum 256 measurements [2] has been implemented. That means that the the noise is reduced by almost 24 dB and hence a dynamic range of 78 dB is achieved.

- **Triggering cables**
  The pulse generator is placed as close as possible to the transmit antenna to reduce the RF cable length which means that less dispersion and attenuation of the transmitted pulse are achieved. Therefore, to measure large distances long triggering cables are needed. However, long cables may introduce loss and dispersion of the triggering pulse which results in higher jitter. For this reason high quality cables are used. Low loss microwave cables (Sucoform, from sucoflex) have been used for experiments up to 18 GHz.

3.2.2 Pulse generator and shaper

The generator used for the measurements fires Gaussian-like pulses with a maximum amplitude equal to -25 V and a width of about 50 ps. The measured generator output and its spectrum are shown in Figure 3.13.

3.2.3 Reference channel

Errors in time-domain measurements can be divided into two groups: short-term errors and long-term errors [63]. The former are due to thermal noise, jitter and quantization noise. Only jitter is discussed here because this error source is specific for time-domain measurements. Jitter can be explained as the non-deterministic variation in the sample position which results into a voltage error

[1] Please note that this is an example and in practice 20 dB might not be enough; hence a higher dynamic range is required (e.g. 40 dB).

[2] This value is the maximum averaging allowed by the measurement system.

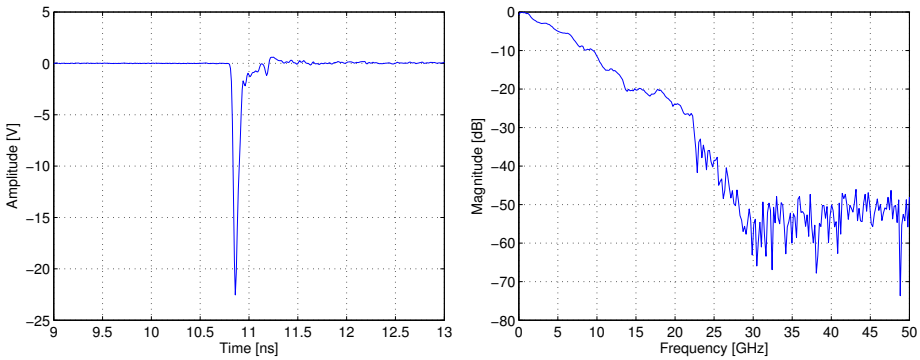

Figure 3.13: *The output of generator PG2 and its spectrum.*

as illustrated in Figure 3.14. Long-term error sources are due to changes in the position and shape of the measurement pulse. These long-term variations are mainly induced by imperfections in the measurement system. The variations in the pulse shape lead to amplitude variations and the variation in the pulse position ("drift") results in phase errors. The measurement results showed a drift of almost 20 ps over three hours. Figure 3.15 shows the measured error in the pulse position caused by drift without changing the setting of the oscilloscope. To compensate for such long-term effect, a reference channel is needed for the measurements. Two possibilities can be applied:

- using an extra receive (reference) antenna at the transmitter site. This puts a limitation for the measurements because an extra antenna support is needed and the distance between the transmit and reference antenna must be kept the same for all measurements which provide some difficulties for measuring at different locations in different environments.

- inserting a cable between the pulse generator and the sampler unit (see Figure 3.4). This solution is preferable as the generator output is directly measured using a coupler and a long cable.

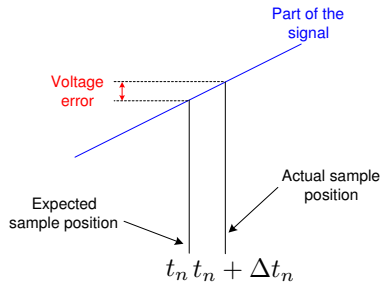

Figure 3.14: *Illustration of the voltage error caused by jitter.*

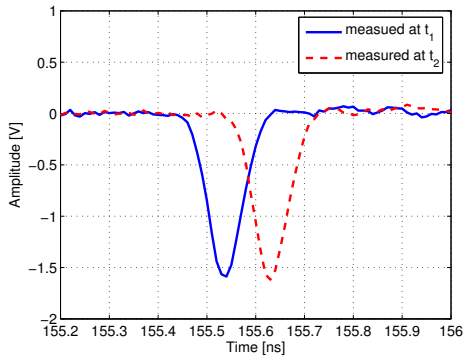

Figure 3.15: *Measured error in the pulse position caused by drift,* $t_1 - t_2 = 13.5$ *hrs.*

3.2.4 Antennas

Radio signal propagation is usually affected by the characteristics of the antennas. For conventional narrow- and wide-band systems, the effect of the antenna can be well separated from the channel because the bandwidth is small, i.e. antenna frequency response can be assumed as flat. However, this is not the case for UWB where the antenna frequency response is not flat over the large bandwidth. Due to this antenna frequency dependency, the channel depends on the type of antenna. Figure 3.16 illustrates the effect of a directive and an omni-directional antenna on the channel impulse response. The transfer function of the antenna H_{ant} can be expressed as a function of frequency and angular pattern characteristics:

$$H_{ant} = g(f, \theta, \phi) \tag{3.20}$$

where f, θ and ϕ are the frequency, azimuth and elevation angles, respectively. The average received signal power $R(f)$ can be represented in the frequency do-

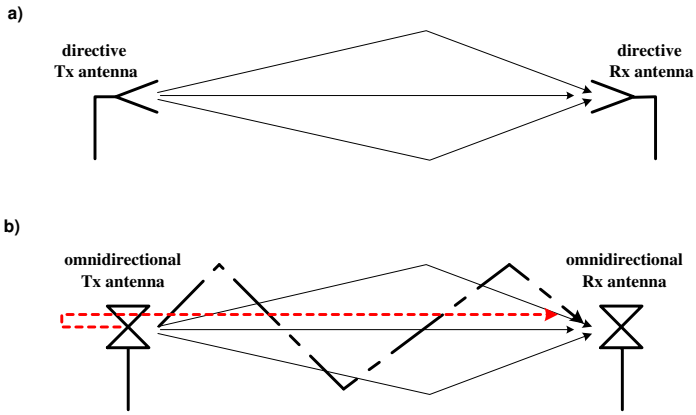

Figure 3.16: *Influence of the antenna type on the channel impulse response when a) directive antennas and b) omni-directional antennas, are used.*

main as:

$$R(f) = \int_0^{\pi}\int_0^{2\pi}\int_0^{\pi}\int_0^{2\pi} G_g(f)H_{Tx}(f,\theta_{Tx},\phi_{Tx})H(f,\theta_{Tx},\phi_{Tx},\theta_{Rx},\phi_{Rx}) \\ H_{Rx}(f,\theta_{Rx},\phi_{Rx})d\theta_{Tx}d\phi_{Tx}d\theta_{Rx}d\phi_{Rx} \tag{3.21}$$

where $G_g(f)$ is the generator signal amplitude spectrum, H_{Tx}, H_{Rx} and H are the transfer functions of the transmit antenna, receive antenna and channel, respectively. Equation (3.21) seems to be more complicated and is very difficult to be used in our evaluations; hence, the angular dependencies of the antennas can be included in the channel. Consequently, the obtained results for the channel impulse response become antenna dependent, meaning that a general characterization of the channel can be offered for the specific antenna used in the measurements. The consequence is that if we use an other antenna, the results will not be the same. Therefore, it may be relevant to characterize the UWB channel for different types of UWB antennas. The effect of using directive or omnidirectional antennas on the channel parameters like rms delay spread and path-loss is investigated in [18].

Different types of antennas can be selected for the measurements. In our Lab three sets of bi-conical antennas and one set of elliptical planar UWB Time Domain antenna (also called Schantz antennas) are available and are shown in Figure 3.17. The bi-conical antennas have already been used for wideband channel measurements at TNO-FEL [26] and were developed to operate at different frequencies 2.4, 4.75 and 11.5 GHz. They are referred to as BC1, BC2 and BC3, respectively. The antenna input reflection and gain characteristics are presented in Figure 3.18. All antennas are calibrated in our an-echoic chamber DUCAT (Delft University Chamber for Antenna Tests). The measurements in DUCAT

are performed using the frequency-domain technique. The results of the radiation patterns for both E-plane and H-plane for BC1, BC2 and BC3 antennas at frequencies 3, 5, 7 and 10 GHz are given in Figures 3.19, 3.20 and 3.21. More details on the Time Domain antennas can be found in [64] [3]. From these results it can be concluded that all antennas radiate quite well in all directions. It should be noted that the same behavior is observed for other frequencies. Also, the gain of the antennas as function of frequency was examined. From these results, we learn that the response of the BC1 and BC2 antennas are almost flat at the frequency band of interest except some discrepancies around 2 GHz for the BC1 and around 3.75 GHz for the BC2 antenna. The BC3 antenna starts to radiate around 4 GHz. Therefore, BC1 antennas have been selected for the measurements since they do not show any discrepancy in the frequency band of interest 3.1-10.6 GHz (e.g. no deep nulls in the radiation pattern and higher gain relative to BC2 and BC3).

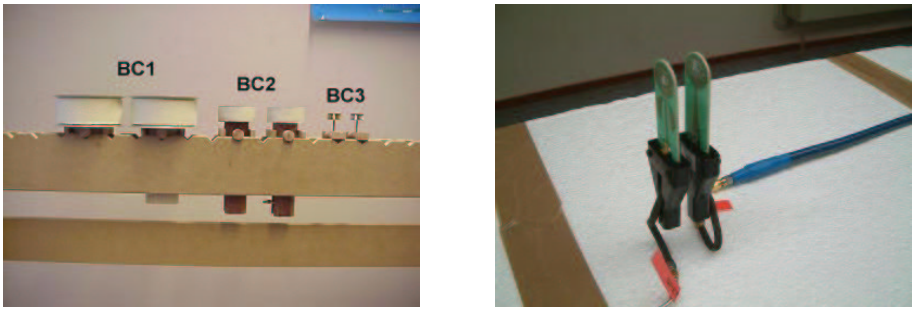

Figure 3.17: *The bi-conical (BC) antennas (left) and Time Domain "Schantz" antennas (right).*

[3] Please note that the Time Domain antennas are developed to operate from 2 GHz to 8 GHz which does not cover the full frequency band of interest.

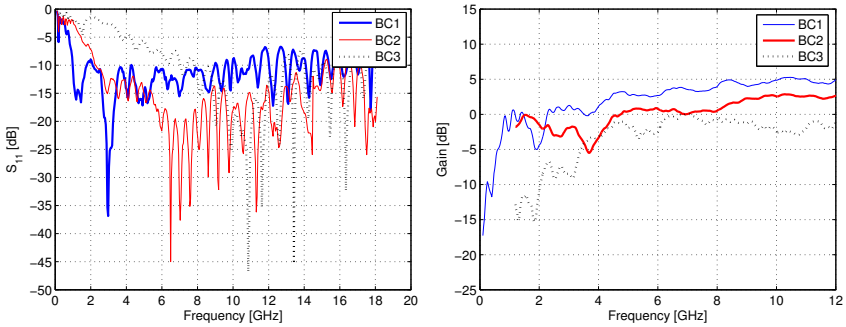

Figure 3.18: *The reflection coefficient and gain as a function of frequency for BC1, BC2 and BC3 antennas*

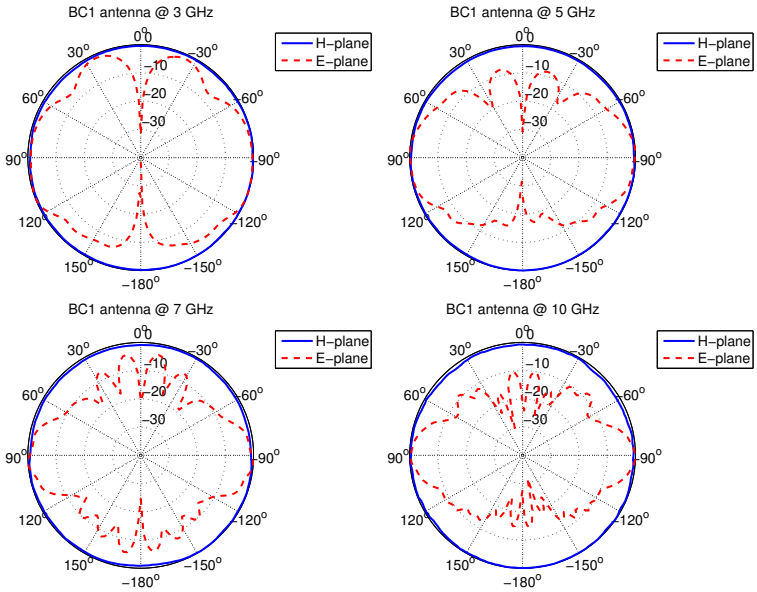

Figure 3.19: *Normalized radiation patterns of BC1 antenna at different frequencies.*

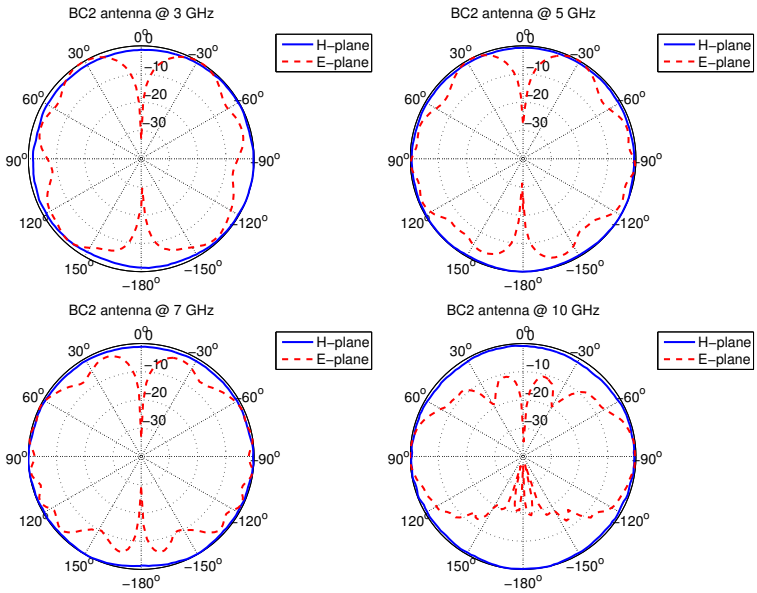

Figure 3.20: *Normalized radiation patterns of BC2 antenna at different frequencies.*

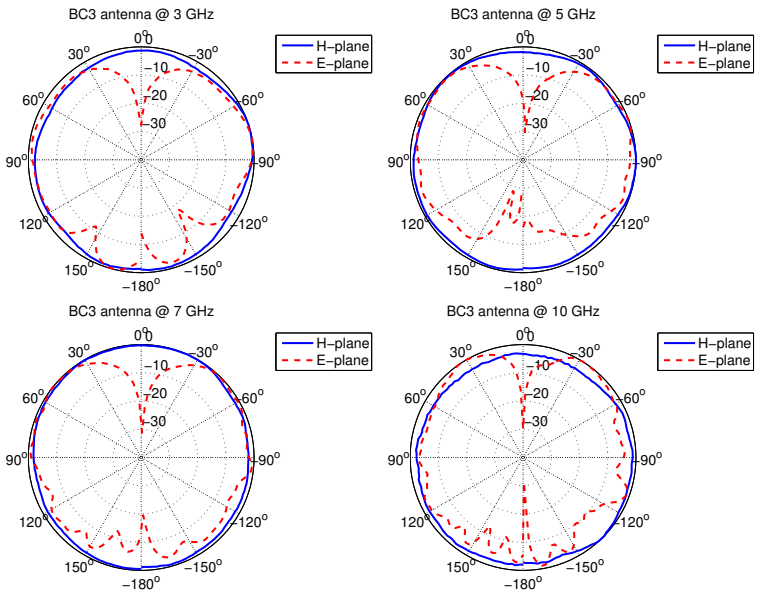

Figure 3.21: *Normalized radiation patterns of BC3 antenna at different frequencies.*

3.2.5 Low Noise Amplifier

In order to extend the maximum distance to be measured, a broadband low noise amplifier (LNA) is used. The LNA is specified over a band from 0.1 to 12 GHz, i.e. covering more than the frequency band of interest. The measured gain of the LNA is shown in [65]. It should be noted that the power budget depends also on the selected antennas: the lower the gain of the antenna, the shorter the maximum measurement distance.

The linearity of the LNA has been checked over the whole frequency band using an adjustable wideband attenuator (e.g. 0 to 11 dB with steps of 1 dB and a bandwidth from DC to 24 GHz). The measurement results from our set-up with antennas are shown in Figure 3.22(a). From this figure it can be observed that the amplifier performs quite well for frequencies up to 8 GHz. However, for the upper-frequency band 8-12 GHz, the transfer function of the LNA seems to be non-linear. A possible explanation for this is that the noise might be higher at higher frequencies due to the frequency-dependent attenuation in the long cable used between the generator and transmit antenna. To avoid higher noise levels at those frequencies the signal is directly measured from the generator output (meaning no antennas) and by using an extra fixed attenuation of 60 dB. The obtained results are given in Figure 3.22(b). From this figure we can see that the LNA is quite linear over the whole frequency range. It should be noted that pilot measurements also show that the LNA is not fully matched to the receive antenna, and hence reflections occur. To avoid this problem an extra 3dB resistive wideband attenuator was used between the receive antenna and the LNA, with the consequence of higher noise figure.

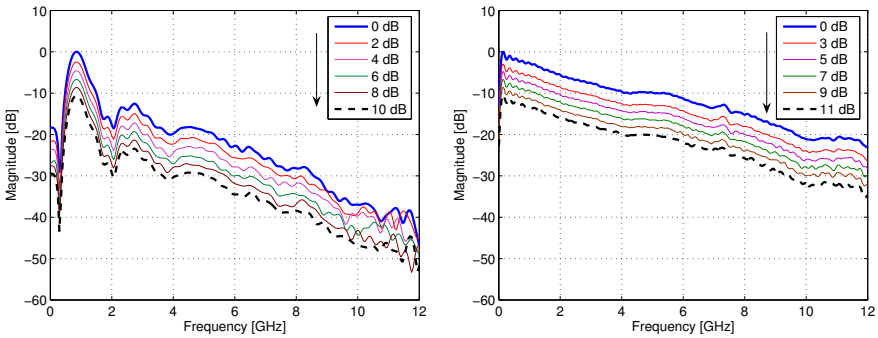

(a) With antennas. (b) Without antennas.

Figure 3.22: *Linearity of the LNA with (left) and without (right) antennas using different attenuator steps.*

3.3 Total set-up performance

3.3.1 Impact of antenna mismatch

Figure 3.23(a) shows an example of the measured impulse response in a LOS situation and 1 m separation between transmit and receive antenna. From this figure it is observed that the signal contains a number of strong multipath components arriving with 26 ns intervals. Different measurements have been repeated at different locations and the same results were found. These paths might be reflections from the channel and hence the PDP can be well modeled by a double exponential function. However, the channel can be considered as random at different locations with different structures and hence different arrival rates of clusters are expected, which is not the case. In this case, it turned out that the reason for occurrence of these clustered paths is a reflection due to mismatch between the generator and transmit antenna. So the pulse bounces between the transmit antenna input and the generator output, which is indicated here as a multiple-antenna-reflection (MAR) issue.

To check whether this effect is happening during the measurements, we have also used a different cable length between the transmit antenna and generator. The results shown in Figure 3.23(a) were obtained by using a 3 m cable length, while the results of Figure 3.23(b) correspond to 6 m cable length. The effect of MARs can be easily detected from these figures namely that the repeated pattern occurs every 26 ns or 52 ns (i.e. twice 26 ns), respectively. It should be noted that these internal reflections do occur in frequency-domain measurement techniques as well. The received pulse due to MARs is placed at different delays according to the length of the cable between the generator and transmit antenna. The MARs can hardly be recognized when a NLOS situation is considered because it will be mixed with multipath components. Moreover, MARs can also lead to measuring a substantially larger maximum excess delay which results in overestimation of the rms delay spread of the UWB channel. Additionally it will remarkably influence the statistics of the channel model parameters like cluster arrival rate.

Several solutions can be implemented to avoid the MAR problem. A standard solution is to use a wideband resistive attenuator between the generator and transmit antenna to attenuate reflections at the expense of a range reduction due to loss in transmit power. Another solution is to use an isolator or a circulator; however such microwave component need to operate over a large bandwidth. A practical solution is to use a longer cable between the generator and transmit antenna. The length of the cable determines the total time window TW that can be measured:

$$TW = 2 \cdot l_c \cdot \tau_{prop} \tag{3.22}$$

where l_c is the length of the cable between the generator and transmit antenna in [m] and τ_{prop} is the propagation delay constant through the cable in [ns/m]. However, a limitation of this solution is that the pulse is attenuated, especially its higher frequency components. Because most of the received power is concentrated

in the first part of the power delay profile [6], a short cable can be used. A cable of 10 m length provides a time window of 90 ns which usually is enough for measuring the UWB impulse response over its full excess delay as reported in [12]. Pilot measurements using a shorter cable of 1 m or 3 m with a wideband resistive attenuator of 6 dB and a cable of 9 m length between the generator and transmit antenna have been performed. The corresponding results are shown in Figure 3.24. From this figure it can be observed that the use of a long cable between transmit antenna and generator provides better results. Clearly, the energy of the signal is higher over the frequency band of interest which can improve the link budget, especially for NLOS channels.

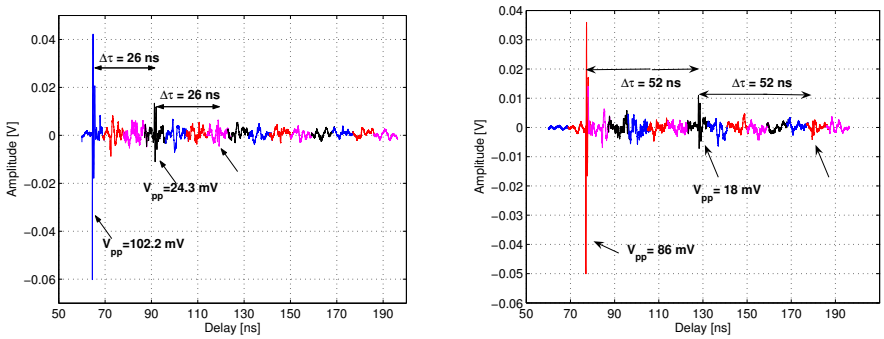

(a) Measured signal using a 3 m cable length. (b) Measured signal using a 6 m cable length.

Figure 3.23: *Illustration of the multiple antenna reflections by using different cable lengths between generator and transmit antenna.*

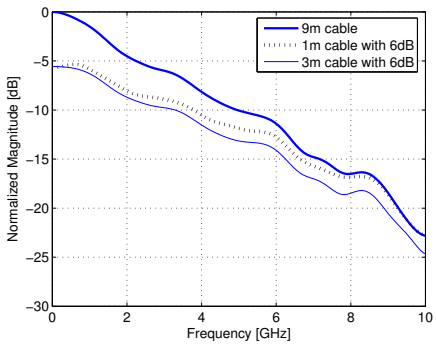

Figure 3.24: *Measurement results comparing the case of using a long cable and/or a 6 dB resistive attenuator.*

3.3.2 Suppression of noise and narrowband interference

As stated before, the UWB measurements can be performed either in FD or TD which in principal provide the same information about the channel. However, a difference exist in the manner how the signal is measured. Clearly, in the FD technique each frequency component is sent and measured over a small bandwidth; on the contrary in the TD technique the signal is measured over a large bandwidth (high sampling rate) based usually on the stroboscopic sampling principle. That means that when a narrow-band interferer is active during the UWB channel measurements, this might influence the results. In several results reported in literature on UWB channel measurements using the time-domain technique [8, 9, 11, 18, 66], the deteriorating effect of this type of noise has not been addressed. In this section, the influence of noise due to non-coherent narrowband interference on the UWB channel measurements performed in time domain is investigated.

After applying the LNA in the receive channel it was observed that while increasing the magnitude of the received signal, the LNA does not improve the SNR by the expected amount (Figure 3.25). Investigation has shown that the receive antenna picks up substantial interference. The spectrum up to 2.4 GHz is heavily used in our measurement environment. Also frequencies around 10 GHz can be occupied by naval radar signals due to ships in the Rotterdam harbor. Because these signals are uncorrelated with the measurement pulse sequence, the stroboscopic (under) sampling receiver creates from this continuous interference a quasi-random noise-like signal. The spectrum of this noise-like signal is almost white in the frequency band between 1-12 GHz and increases at frequencies below 1 GHz as can be seen in Figure 3.26(left). Figure 3.26(right) shows the measured noise over a large time window (i.e. 6 microseconds). From this figure large peaks can be observed which are due to the sampling of narrow-band interferences. These peaks are quite high and might influence the UWB channel measurements.

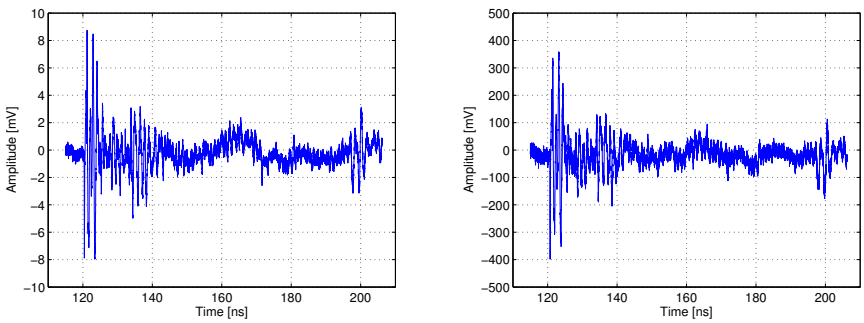

(a) Without LNA. (b) With LNA.

Figure 3.25: *Measured signal at 10 m for a LOS channel.*

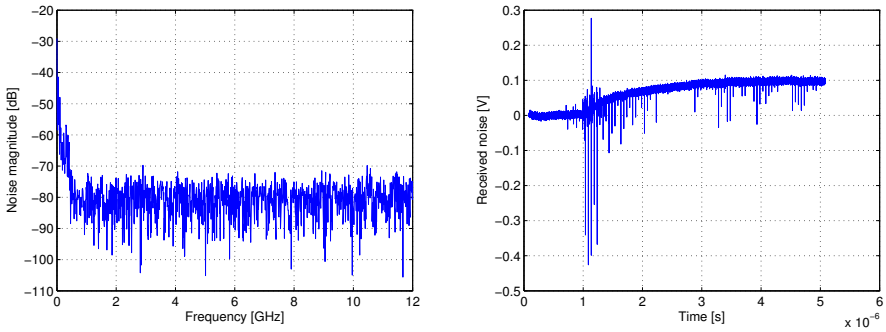

Figure 3.26: *Magnitude of the received noise (left), measured noise and narrowband interference (right).*

From experiments with different antennas, we observed that the noise level decreased for antennas with less gain at frequencies below 2 GHz. In this case, the antenna acts as a high-pass filter, partly suppressing low-frequency interference signals. In order to suppress this interference at frequencies below 2.4 GHz and to improve the SNR of the measurements, an analogue bandpass filter (4 to 8 GHz) is put directly behind the receive antenna terminal. Figure 3.27 shows the received noise without filter and Figure 3.28 with filter. In order to determine the rms value of the received noise, the sliding time window method for eliminating the mean signal characteristics has been used. Comparing the results, we can observe that the rms noise level has remarkably been reduced.

Furthermore, measurements have been performed using this filter in order to show its impact on the SNR. The measured signal at 25 m for a LOS situation without filter and with filter is shown in Figure 3.29. The measured signal at 10 m for NLOS without and with filter is shown in Figure 3.30. From these figures it can be observed that for both LOS and NLOS the SNR is improved by filtering because of the rejection of interference and noise. The rms value of the received noise for the case without and with filter is about 5.9 mV and 0.15 mV, respectively. The peak-to-peak voltage of the direct path at 1 m for the case without and with filter is 2.03 V and 0.92 V, respectively. Based on this, the SNR is improved by:

$$\begin{aligned} \Delta SNR &= |SNR - SNR_{filter}| \\ &= 20\log_{10}\left(\frac{2.03}{5.9}\,\frac{0.15}{0.92}\right) \\ &= 25\,\text{dB} \end{aligned} \tag{3.23}$$

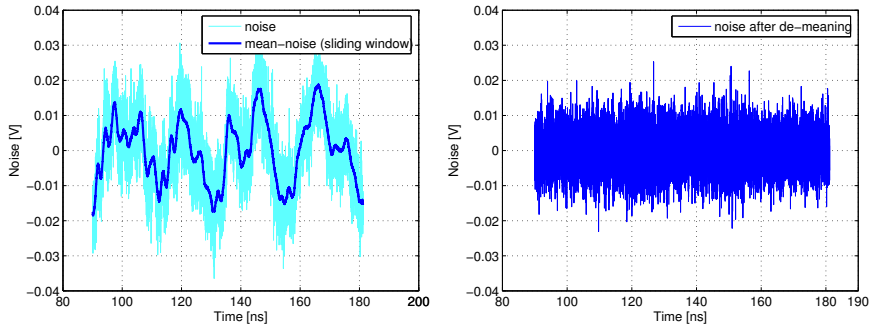

Figure 3.27: *Received noise and its mean.*

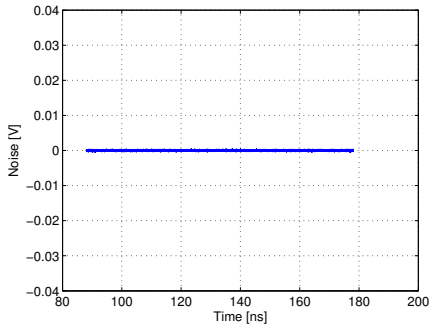

Figure 3.28: *Received noise using a bandpass filter (4-8 GHz).*

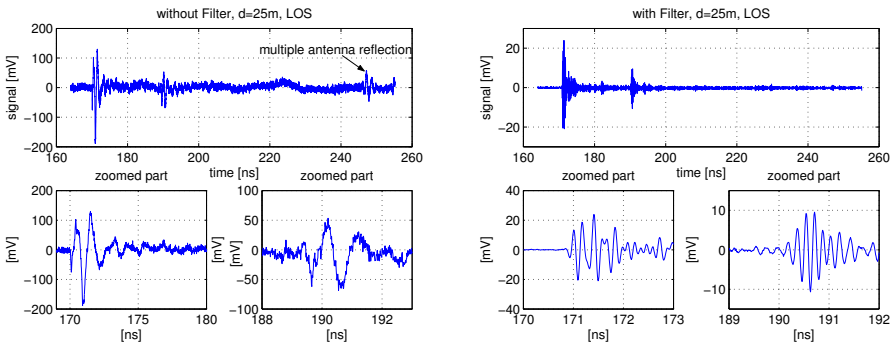

Figure 3.29: *Received signal without and with filter at 25 m LOS.*

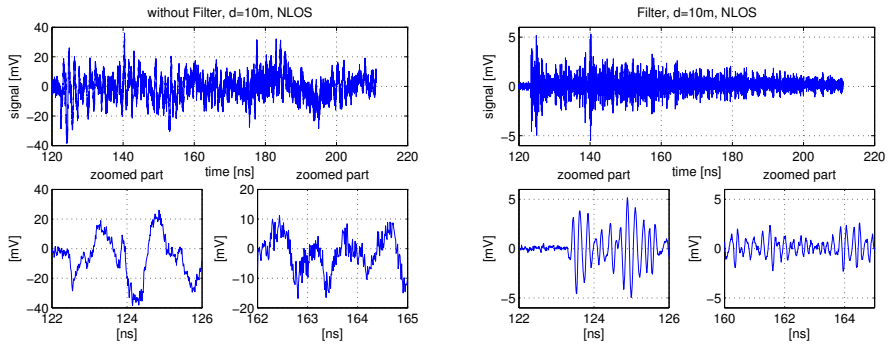

Figure 3.30: *Received signal without and with filter at 10 m NLOS.*

3.4 Validation of time domain measurements

Before we started with the measurements, we have examined whether our UWB time-domain measurements give correct results. To this end, the BC1 antenna has been characterized using both time-domain and frequency-domain set-ups. Figure 3.31 gives the frequency response of the antenna. From this figure it

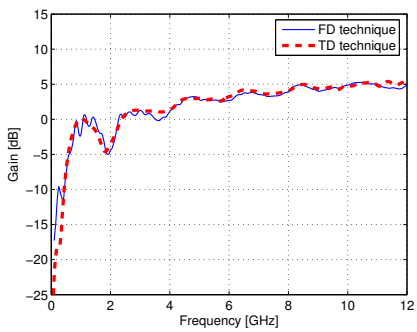

Figure 3.31: *The gain of the BC1 antenna measured using frequency-domain and time-domain techniques.*

can be observed that the same gain is obtained using both techniques. Some discrepancies at low frequencies are due to insufficient performance of the absorber materials used within the anechoic chamber (the absorber material is specified for frequencies above 2 GHz). The small variation between the results may be due to

different antenna support and different separation distances considered in time- and frequency-domain measurements.

3.5 Chapter summary

In this chapter, a time-domain measurement set-up for UWB wireless channel characterization covering the frequency band from 3.1 to 10.6 GHz, is developed. Limited acquisition time window length, which is a typical problem in the time-domain technique, is solved by introducing a new method called "Overlap Time Interval". This method is based on measuring different time windows in cascade and overlapping each other. This time-framing between the time windows allows us to correct any delay inaccuracy in the oscilloscope setting. This method is used in all UWB channel measurements described in next Chapter 4. Another important aspect is the multiple reflections which are due to the mismatch between the set-up components (e.g. generator and transmit antenna). This aspect has to be avoided in the measurements because it remarkably influences the actual statistics of the UWB channel.

Under-sampling of non-coherent narrow-band interference in time-domain UWB channel measurements reduce the signal-to-noise ratio. Clearly, in the time-domain technique energy of external narrow-band interference (especially at frequencies below 3.1 GHz) is spread over the whole measured bandwidth as quasi-white noise. This is caused by under-sampling in the stroboscopic receiver used in the measurement set-up. The level of this additional noise is relatively high and its suppression is required for long-distance measurements. In order to suppression out-of-band narrow-band interference an analogue band-pass filter can directly be placed after the receive antenna which decreases the noise and results in a substantial improvement of the "signal-to-noise" ratio.

Initial measurements confirm the validity of the approach by comparing time-domain measurements with frequency-domain measurements.

Chapter 4

UWB Channel Measurements: Processing and Modeling Results

The performance of any communication system is determined by the characteristics of the radio channel in which it operates. For a UWB communication system, the channel is rather different from a conventional narrow-band one regarding many propagation aspects. Thus, the UWB system designer should have realistic UWB channel models to evaluate the system performance.

The main objective of this chapter is to provide relevant channel models to support the UWB communication system design and evaluation. The channel modeling is performed using the statistical approach based on measurements. Here, different channel models, covering the FCC-approved frequency band 3.1-10.6 GHz, are proposed and validated by means of measured data. In order to provide a good statistical UWB channel characterization, a sufficient number of channel impulse responses (CIRs) are gathered.

In this chapter, the measurement scenarios are described. The measurements are performed using the set-up described in Chapter 3. As the CIRs strongly depend on the physical environment, the measurements have been conducted in different locations (e.g. indoor office, industrial area ... etc.). The CIRs are retrieved from the measured data using an appropriate post-processing. Based on these obtained CIRs different channel models are proposed and its statistics are extracted from the measured data for different environments.

4.1 Description of measurement scenarios

Based on the various applications of UWB communication systems, different measurement scenarios are proposed to characterize the UWB channel. These scenar-

ios are discussed below.

4.1.1 Indoor office environment

The measurements were carried out in the EEMCS faculty building of the Technical University of Delft (TU-Delft) at different floors. The external walls are made of concrete and the floors of reinforced concrete. To characterize the small-scale and large-scale fading parameters of the UWB channel, a grid of 7x7 with a spacing of 5 cm between adjacent points was designed and used in the measurements. The grid was made of wood to reduce reflections. The maximum measurement distance is about 10 m and both LOS and NLOS situations were considered. The LOS measurements were conducted in a corridor, an office (i.e. small room) and a library (i.e. large room). The NLOS measurements were conducted in the following locations: corridor to office, office to office and library[1]. In each scenario, the receiver is kept at a fixed position Rx and the position of the transmitter Tx has been changed. A total of 1470 channel impulse responses have been recorded. Figure 4.1 shows the plan for the measurement scenarios.

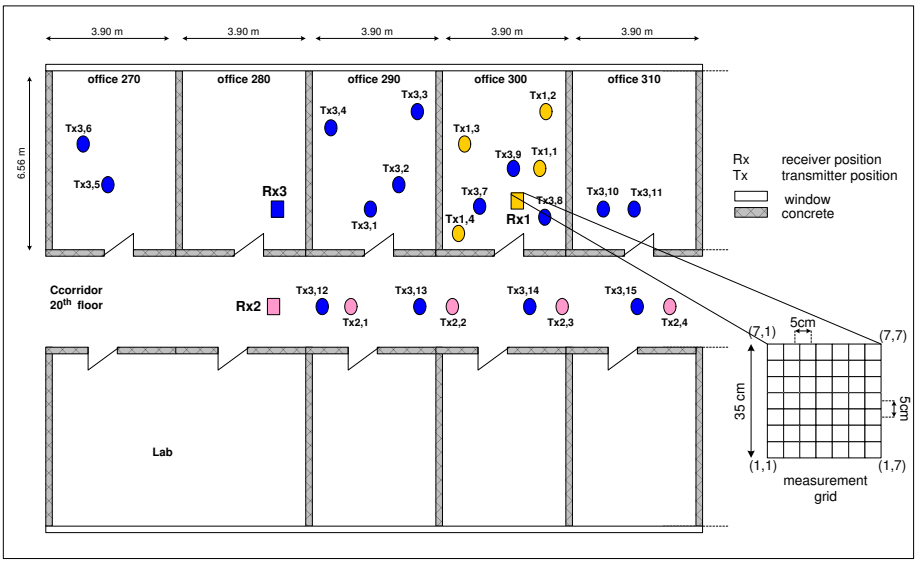

Figure 4.1: *The floor plan for the indoor office scenarios at the 20th floor of the EEMCS building.*

[1]Please note that these measurements have been conducted on the 20th floor except for the library which is located on the 2th floor of the EEMCS faculty building

4.1.2 Indoor industrial environment

For the industrial environments, measurements have been conducted in the laboratory for "Apparatenbouw en Proces Industrie" (API) of TU-Delft. This laboratory contains densely packed metal structures and equipment which makes it representative for radio experiments in an actual "Process Industry" environment. During all measurements, the receiver was kept at a fixed location Rx. For the measurements of different channels, the transmitter was put at different locations Tx in the building. Most of the measurements were taken with the transmitter at ground level. The picture shown in Figure 4.2 gives an impression of the measurement environment. For this scenario, 73 channel impulse responses were obtained; covering distances between 1-25 m. More details about this scenario can be found in [67].

Figure 4.2: *An impression of the API measurement environment.*

4.1.3 Outdoor to indoor environment

In many emergency situations, particularly within large buildings, which may be partially or completely collapsed, communications with rescue personnel can be difficult. Due to its good through-wall penetration and high resolution, UWB technology is foreseen as a good candidate for such applications improving the reliability of communications and allowing precise locationing of personnel. Usually the communication in these scenarios happens either from outside to inside or from inside to outside. However, the radio channel is totally different for the case where both the transmitter and receiver are at close location. Efforts have been made to measure and model the UWB channel in indoor [8, 10, 12, 13, 16, 18, 68] and in outdoor [69, 70] environments. However, a limited or no channel measurements have been found from outdoor to indoor. In our measurements campaign, such scenario has been taken into consideration. To this end, a number of measurements is carried out on the TU-Delft Campus in 3 different locations:

- Balcony 21th floor: the transmitter is placed at a fixed position on the roof of the 21th floor of the TU faculty building, and the receiver at different positions inside the building. In this scenario the transmitter is placed at 3 m and 6.5 m away from the building. In this case, the transmitted UWB signal travels through windows (double glass) into a hallway and into adjacent rooms. In total (7+9)*8=128 measurements have been recorded.

- API-building for industry: the transmitter grid is located outside the building. The receiver is put at different locations inside the building. In this scenario we measured at 12 positions 12*8=96 channel impulse responses.

- Library: in these measurements the grid structure is placed at the receiving site. The receiver is inside the library and its position is kept fix during all measurements. The transmitter was placed in the corridor and its locations were on a straight line. For this scenario at 9 positions 72 measurements were obtained in total.

Details on this scenario can be found in [71].

4.1.4 WPAN environment

UWB is becoming a promising technology for WPAN (wireless personal area network) applications because of its capability of supporting high-rate short distance communications and low power consumption. In our measurement campaign, a number of practical usage scenarios well suited for UWB-WPAN applications have been identified. The measurements for a such scenario were conducted in an office environment at the 20th floor of our building. The dimensions of the office is 6.5x4 m. It contains a desk with metallic drawers underneath, a computer (display and case), a telephone set on the desk and a chair. In total, 4 situations can be distinguished for this scenario:

- wpan1: The transmitter and the receiver were placed on table with a height of 76 cm. The height of the antenna support is about 21 cm, so the antenna itself is 97 cm above the ground. On the table there is a computer (display, keyboard, mouse and tower). The table is a wooden one, with a metallic drawer underneath at both sides. The receive antenna was kept fixed while the transmit antenna was moved along a straight line doing measurements at 5 cm intervals from 100 cm to 20 cm. Both LOS and NLOS measurements have been performed. For the NLOS case the receive antenna was put behind a display as shown in Figure 4.3(a).

- wpan2: This scenario was in the same location as the previous scenario, but the transmit antenna was placed under the table near the left metallic drawer (see Figure 4.3(b)). The receive antenna was placed next to the tower of the computer. Two cases have been considered: 1) the antennas are not oriented in its maximum radiation direction, so the direct path is

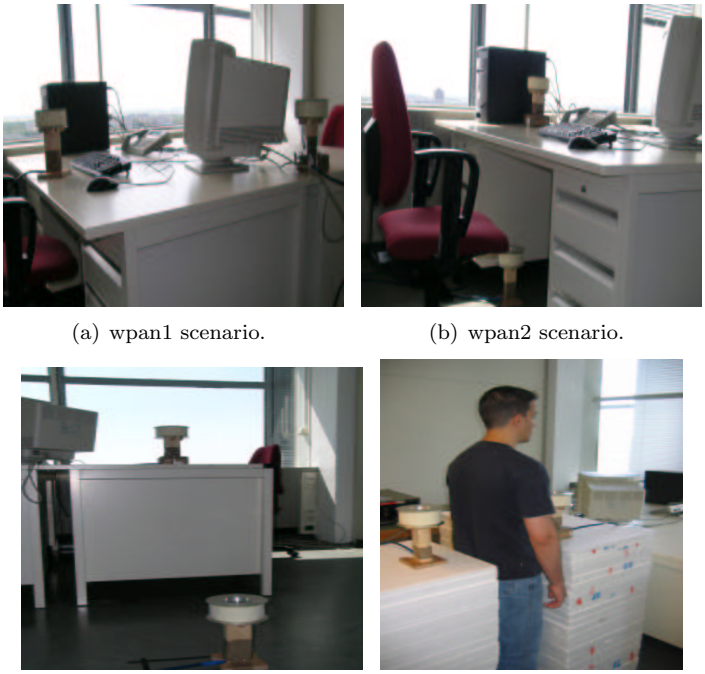

(a) wpan1 scenario. (b) wpan2 scenario.

(c) wpan3 scenario. (d) wpan4 scenario.

Figure 4.3: *Illustration of the wpan scenario.*

not expected to be strong, and 2) the antennas are well oriented in its maximum radiation direction. The measurements were done every 4 cm for different heights of the transmit antenna. To change the height of the antenna, polystyrene sheets (foam) were used. The minimum height of the transmit antenna was 21 cm (the height of the antenna support).

- wpan3: In this scenario the receive antenna was situated on the table, while the transmit antenna was situated on the ground giving a LOS situation. The distance between the vertical axes of both antennas is 1 m. The difference in height of the antennas was 76 cm (the height of the table). The transmit antenna was moved vertically, changing its height in steps of 6 cm up till a height of 135 cm above the ground. Additional measurements were conducted in such way that the antennas could be situated in a manner that (depending of the height of the transmit antenna) they will be in LOS or NLOS as depicted in Figure 4.3(c). At the beginning the antennas are in NLOS situation. When the transmit antenna goes beyond the table, it becomes in a LOS situation.

- wpan4: In this scenario, the measurements were done to determine the

effects of the body on the channel. For instance, the measurements were performed interposing a human body between the Tx and Rx antenna as shown in Figure 4.3(d).

Further details on this scenario can be found in [72].

4.1.5 Roughness scenario

To investigate the roughness effects of the wall on UWB propagation, a measurement setup has been developed. The main idea is to illuminate a rough wall with an UWB signal and measure the reflected signal. To this end, a wall of 1m by 1m of plaster has been made with a thickness of 15 cm. To make the wall rough, different stones with different sizes were used and put randomly on the wall. The wall was placed on foam boards at a distance of 50 cm from the ground. In this way the stones could easily be distributed over the surface. For these measurements the "Schantz" Time Domain antennas have been used (2-8 GHz). The minimum wavelength is about 3.75 cm. Thus the maximum size of the stones should not be more than 1.85 cm (half the shortest wavelength) to avoid resonances from the stones. Different stones of different sizes and heights were used:

- quartz stones:
  - 4-8 mm
  - 8-16 mm
  - 4-32 mm
- broken quartz stones
  - 1-3 mm
  - 4-8 mm

The stones and the measurement set-up are shown in Figures 4.4 and 4.5. For each stone size 6 volumes were selected: 125 ml, 250 ml, 375 ml, 500 ml, 750 ml and 1000 ml. Further, for each volume 30 measurements with random distribution of the stones have been performed. In total 4*6*30=720 measurements have been gathered.

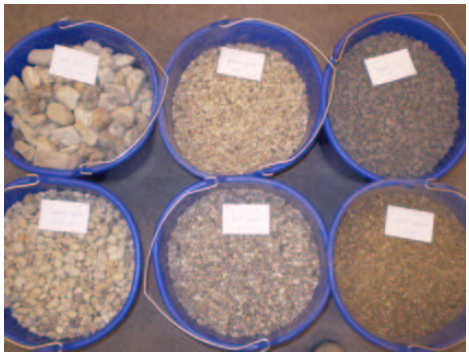

Figure 4.4: *Different stones used for the measurements.*

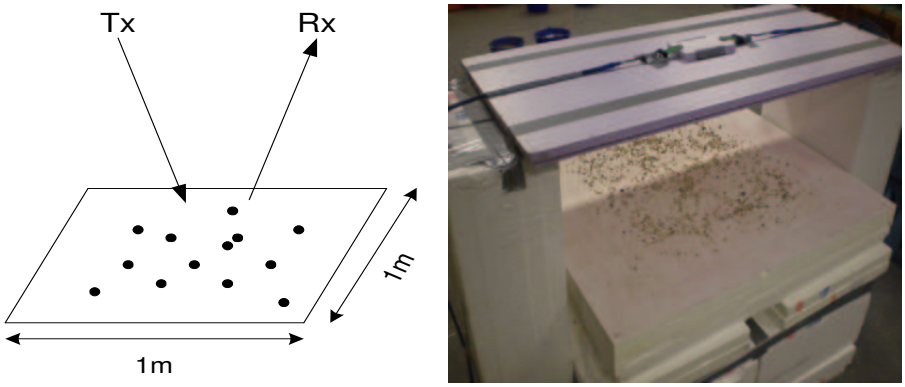

Figure 4.5: *Illustration of the measurement scenario.*

4.2 Data analysis and post-processing

4.2.1 Antennas and components effect

To extract the channel impulse response from the measured signal, an appropriate data analysis technique is required. The received signal $r(t)$ is usually affected by both the transmit and receive antenna characteristics as well as by the measurement system and can be expressed as:

$$r(t) = p(t) * h_{sys}(t) * h_{Tx}(t) * h(t) * h_{Rx}(t) \tag{4.1}$$

where $p(t)$ is the generator output, $h_{sys}(t)$ characterizes the transfer through the measurement system (i.e. cables, filter and LNA), $h_{Tx}(t)$ and $h_{Rx}(t)$ are the impulse responses of the transmit and receive antenna respectively, and $h(t)$ is the channel impulse response. So, extracting the channel impulse response (CIR) $h(t)$ from the measured signal $r(t)$ allows a general analysis of UWB channels regardless of the generator output, the measurement system as well as the antennas used in the measurements. In the case where no channel is present, the received signal will be the result of the convolution of the generator output with the measurement system and with both antenna responses. If the channel is free-space, its impulse response is simply an impulse at a certain delay equal to the propagation time τ_1. We find:

$$r_{free-space}(t) = p(t) * h_{sys}(t) * h_{Tx}(t) * \delta(t - \tau_1) * h_{Rx}(t) \tag{4.2}$$

This signal is almost equivalent to the direct unobstructed LOS (i.e. line of sight) path with no reflectors/difractors in the environment. This means that if a received pulse from only the LOS path can be isolated from other pulses (using time gating), this pulse can be used to determine the CIR. This received pulse can be expressed as:

$$p_{rx-los}(t) = p(t) * h_{sys}(t) * h_{Tx}(t) * h_{Rx}(t) = r_{free-space}(t + \tau_1) \tag{4.3}$$

This pulse contains all effects which we would like to remove from the measured signal in order to determine the CIR. The received signal of equation (4.2) can be written as:

$$r(t) = p_{rx-los}(t) * h(t) \tag{4.4}$$

So, once the signal $p_{rx-los}(t)$ is known, the channel impulse response can be well retrieved by de-convolving $p_{rx-los}(t)$ from $r(t)$. From a careful measurement, the template $p_{rx-los}(t)$ is obtained and used for the de-convolution process. Figure 4.6 shows $p_{rx-los}(t)$ and its spectrum measured at 1 m separation distance between the transmit and receive antenna.

4.2.2 De-convolution methods

The de-convolution can be seen as the process to separate two signals that have been combined by convolution. It can be applied in the time- or frequency-domain.

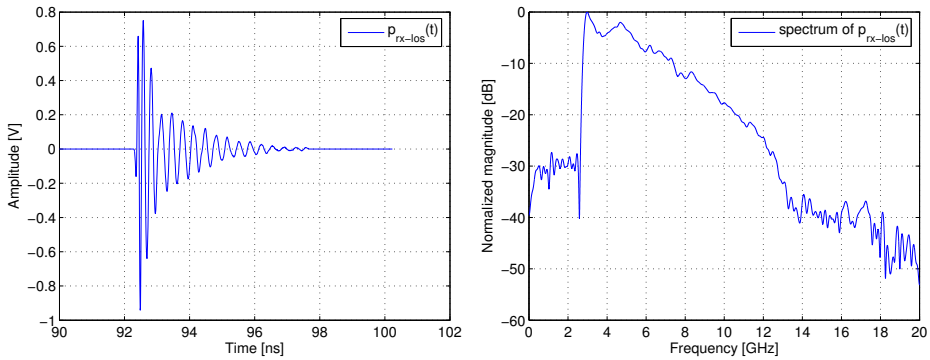

Figure 4.6: *The measured reference pulse at 1 m and its spectrum.*

CLEAN algorithm

In time-domain, the de-convolution can be applied by using a kind of super-high resolution algorithm like CLEAN [9, 73]. This algorithm applies matched filtering to find the strength and delay of individual multipath components. The algorithm searches the received waveform iteratively with a template to find maximum correlation. Discrete components in the impulse response (i.e. due to individual multipath components) that are separated by less than the pulse width can be resolved. The algorithm performs the following steps:

1. initialize a so-called "dirty" map with $d(t) = r(t)$ and a "clean" map with $c(t) = 0$;
2. derive the correlation function $\Gamma(\tau) = p_{rx-los}(t) \odot d(t)$ ($\Gamma(\tau)$ is normalized with $\Gamma_{rx-los} = p_{rx-los}(t) \odot p_{rx-los}(t)$; $\odot$ means correlation);
3. find all peaks, Γ_i, and their positions, τ_i, in $\Gamma(\tau)$;
4. ignore peaks Γ_i below the threshold;
5. clean the dirty map by $d(t) = d(t) - \Gamma_i p_{rx-los}(t - \tau_i)$;
6. update the clean map by $c(t) = c(t) + \Gamma_i \delta(t - \tau_i)$;
7. repeat the process starting with step 2 until all peaks are below a predefined threshold in step 4;
8. the estimated channel impulse response becomes $h(t) = c(t)$.

As stopping criterion for the CLEAN algorithm, a threshold below the maximum correlation should be set. In the following we discuss some limitation of the CLEAN algorithm. As stated in the previous paragraph, the CLEAN algorithm uses a matched-filtered signal to estimate the delays and strengths of

the multipath components (MPCs). In the case where the MPCs are all resolvable, the CLEAN algorithm would give a perfect estimate of the CIR. However, when the paths are not resolvable, the matched filter output is affected and the CLEAN algorithm does not necessarily produce the true CIR. This is because the unresolvable pulses will sum up and produce some constructive and destructive interference. As a consequence, the peaks in the matched filter will be shifted away from the true delays and through the iterative operation of the algorithm errors will be produced in the estimated CIR. To illustrate this effect, we consider a two-path channel with the following impulse response:

$$h(t) = \sum_{i=1}^{2} a_i(t)\delta(t - \tau_i) \tag{4.5}$$

where $a_i(t)$ are the channel coefficients. The received signal can be written as:

$$r(t) = p_{rx-los}(t) * h(t) = a_1(t)p_{rx-los}(t - \tau_1) + a_1(t)p_{rx-los}(t - \tau_2) \tag{4.6}$$

Let's assume $a_1 = a_2 = 1$. Figure 4.7 shows the two-path CIR and its estimate using the CLEAN algorithm for $\Delta\tau = 3$ ns and $\Delta\tau = 150$ ps with $\Delta\tau = \tau_2 - \tau_1$. From this Figure it can be concluded that when the two pulses are sufficiently separated in time-domain CLEAN gives a perfect estimate. However, when the two pulses overlap with each other, CLEAN deviates from the real CIR. Due to the destructive interference, the largest correlation is negative at a delay between τ_1 and τ_2 and the algorithm continues from this incorrect estimated path to find other paths that minimize the up-dated matched filter output.

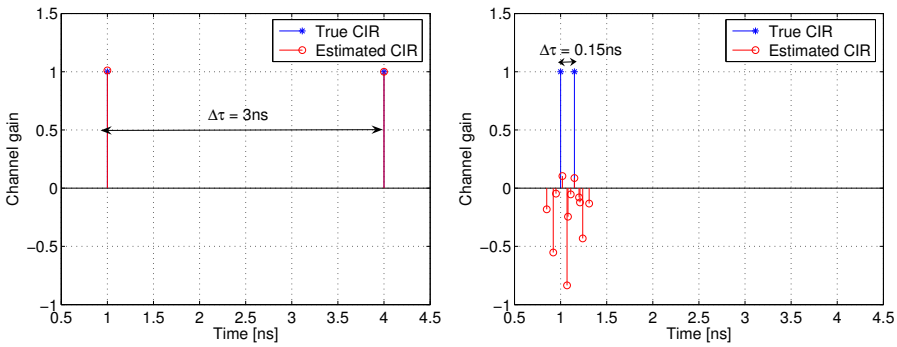

Figure 4.7: *De-convolution using the CLEAN algorithm for different time interval $\Delta\tau$ between the pulses.*

Inverse filtering

The most straightforward de-convolution method used in frequency-domain is known as inverse filtering. For instance, equation (4.4) becomes:

$$R(f) = P_{rx-los}(f)H(f) \tag{4.7}$$

where $R(f)$, $P_{rx-los}(f)$ and $H(f)$ are the Fourier transforms of $r(t)$, $p_{rx-los}(t)$ and $h(t)$, respectively. The channel transfer function can be determined as:

$$H(f) = \frac{R(f)}{P_{rx-los}(f)} \tag{4.8}$$

The UWB CIR can be obtained using the inverse Fourier transform of $H(f)$. It should be noted that when equation (4.8) is blindly applied, then the estimate of $H(f)$ will be unreliable especially when $P_{rx-los}(f)$ is noisy. To avoid this problem zeros can be added to $H(f)$ at frequencies outside the signal bandwidth. In order to reduce the leakage problem when transforming the signal back to time-domain, a Hamming window was used which provides side-lobes of about -43 dB [57]. The obtained signal in time-domain is a continuous signal. To estimate the MPCs the discrete channel impulse response (D-CIR) method is usually used. This method is adopted by the IEEE UWB channel modeling sub-group [74]. In this approach, the temporal axis is divided into delay bins and each bin is assumed to contain either one resolvable path or no path. The width of each delay bin is determined by the signal bandwidth. For a selected bandwidth of 7.5 GHz (from 3.1 to 10.6 GHz), the MPCs are estimated with a resolution of about 134 ps. The power for each bin is then computed; if it is above a threshold level then it is assumed that the path is present, if not then the bin is set to zero. This method may provide the advantage of its simplicity and it is more convenient to be used in practice as it can be considered as a type of delay line model. However, it has the drawback that the number of paths are overestimated. This is because the pulse width in time-domain is wider than $1/B_w$. In fact the pulse width is about $2/B_w$ and if a frequency-domain window is applied the pulse width becomes even larger than $2/B_w$. This means that when we start to collect the energy each $1/B_w$, one received pulse can be represented by more than one path. This effect can be illustrated by the following example.

Let's assume a one path channel (e.g. LOS path). The measured frequency response of the UWB channel can be given as:

$$H(f) = \begin{cases} 1 & \text{if } |f| < \frac{B_w}{2} \\ 0 & \text{otherwise} \end{cases} \tag{4.9}$$

The CIR can be obtained by use of an IFFT:

$$h(t) = sinc(\pi B_w t) \tag{4.10}$$

Let's assume that we are interested only in the main lobe. Then, the energy E_n^i of the ith bin can be determined as:

$$E_n^i = \int_{t0}^{t0+iT_b} sinc^2(t)dt \tag{4.11}$$

where $T_b = 1/B_w$. Collecting the energy each $1/B_w$ two paths are detected instead of one path as can be seen from Figure 4.8. This remarkably influences the statistics of the UWB channel.

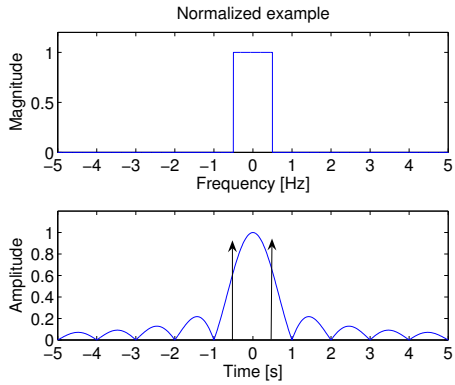

Figure 4.8: *Illustration of the path estimation using the D-CIR method.*

To avoid this problem, we introduce the so-called maximum detection (MD) method in which the paths are estimated by detecting local maxima. This method provides a simple implementation and the maximum peak may give an indication of the presence of the path. It should be noted that the discussed methods will provide the same statistics of the UWB channel for path-loss, fading margin and rms delay spread. However, a huge difference can be observed in the statistics for the number of multipath components. From simulation point of view, this might lead to a wrong reconstruction of the measured CIR. In the following, we evaluate this effect by means of regenerating/recontruction the measured CIR using the obtained statistics of each method. Figure 4.9 shows an example of the measured CIR and the reconstructed CIR for both methods. From this figure, it can be observed that D-CIR leads to a huge deviation in the modeling results whereas the MD method converges to the "true" measured CIR. To quantify this effect, we define the following error ε_h between the measured and estimated CIR:

$$\varepsilon_h = \frac{|E_{h(t)} - E_{\hat{h}(t)}|}{E_{h(t)}} \tag{4.12}$$

where $E(.)$ denotes the energy, $h(t)$ is the estimated CIR and $\hat{h}(t)$ is the modeled CIR. Figure 4.10 shows the cumulative distribution function (CDF) of ε_h for

both (D-CIR and MD) methods. From this figure it can be concluded that at 80% chance ε_h is less than 10% for the MD method whereas it is about 200% for D-CIR and hence the MD is more preferable to be used in our modeling analysis.

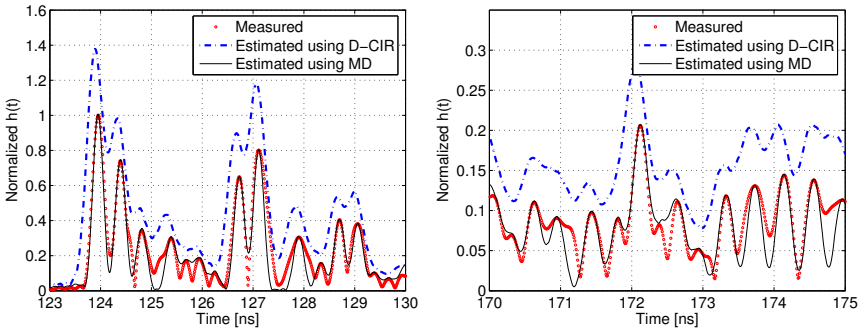

Figure 4.9: *Comparison of the measured and estimated (using D-CIR and MD methods) CIR at different time delays (corridor-office, 10 m).*

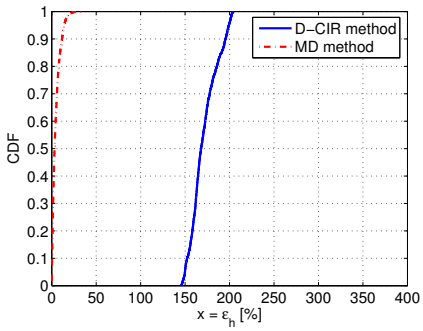

Figure 4.10: *CDF of ε_h of the reconstructed CIR using D-CIR and MD method.*

4.2.3 Threshold setting

The setting of the threshold is an important key parameter to determine the CIR. This threshold has to be set taking into account the amount of the total received power, relevant multipath components and noise level. Figure 4.11 shows the total received power averaged over all measurements for LOS and NLOS propagation using the MD method. From this figure it can be observed that for both LOS and NLOS channels a threshold level of 40 dB below the strongest path is enough to receive nearly all power, and for a threshold level of 30 dB the received power is about 97% of the total power. Moreover, the number of received paths for the

40 dB threshold level is 185 and 221 for LOS and NLOS, respectively, and for the 30 dB threshold level this number is 62 and 140, respectively as can be read from Figure 4.12. As the difference in the received power between the threshold level of 30 and 40 dB is only 3%, the impact of the added paths (e.g. 185-62= 123 for LOS and 221-140=81 for NLOS) is negligible when compared to the amount of the power delivered by those paths. Therefore, we have introduced a factor called the threshold impact factor γ_{TIF}, given as:

$$\gamma_{TIF} = \frac{\Delta P_r}{N_r} = \frac{{P_r}^{total} - {P_r}^{th_i}}{N_r^{th_i}} \tag{4.13}$$

where P_r^{total} is the total received power, $P_r^{th_i}$ and $N_r^{th_i}$ are the received power and the number of paths for a certain threshold "th_i", respectively. The parameter γ_{TIF} as a function of the threshold is shown in Figure 4.13. From this figure, it can be concluded that a threshold of 30 and 25 dB is enough to model the recorded channels for LOS and NLOS propagation, respectively. Moreover, our signal and noise analysis shows that this threshold level setting is always above the noise floor as can be seen in Figure 4.14. In our further analysis and channel modeling, a threshold level of 30 dB is therefore selected.

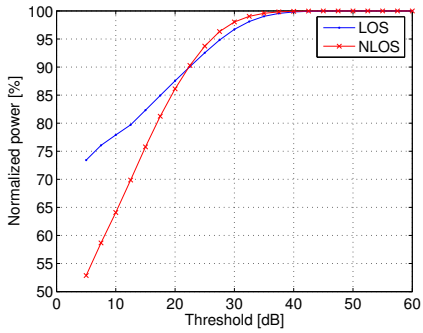

Figure 4.11: *Total received power as a function of threshold (0 dB is strongest path).*

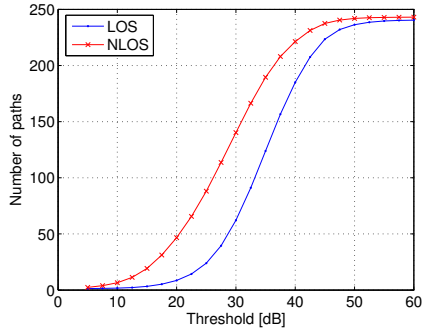

Figure 4.12: *Number of multipath components as a function of threshold.*

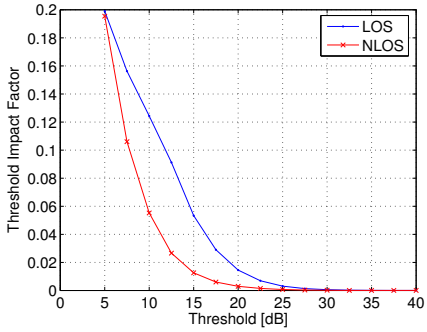

Figure 4.13: *The threshold impact factor as a function of threshold.*

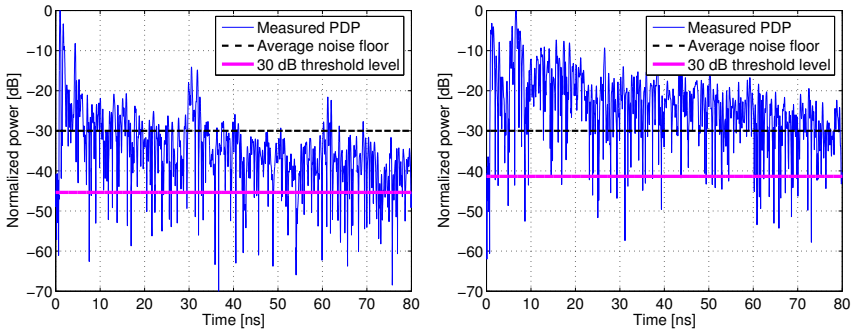

Figure 4.14: *Typical measured PDP: LOS channel, corridor, 10 m (left) and NLOS channel, corridor-office, 5 m (right).*

4.3 Modeling results and discussion

In Chapter 2, different important channel parameters needed for a UWB communication system design were given. In this section, we try to model most of those parameters. For instance, the large-scale path-loss as well as the small-scale fading are modeled. In addition to this, time dispersion of the UWB propagation signals are also evaluated. We note that the modeling results are discussed in details in the next section.

4.3.1 Large-scale path-loss model

The path-loss model suggests that the average path-loss increases exponentially with distance between transmit and receive antenna according:

$$PL(d) = \overline{PL_0}(d_0) + 10\alpha \log_{10}(d/d_0) + X_\sigma \tag{4.14}$$

where $PL(d)$ is the average path-loss at distance d, relative to a reference distance d_0. The parameter α represents the path-loss exponent and it indicates how fast the path-loss increases with distance. X_σ is a Zero-mean Gaussian-distributed random variable in dB with standard deviation σ. The path-loss exponent is obtained by fitting a line of the received energy versus distance. However, the standard deviation for the Gaussian random variable is determined by calculating the deviation from the obtained fit.

Figures 4.15 and 4.16 give the path-loss model and the standard deviation of the shadow fading for all data collected in the indoor office for LOS and NLOS cases, respectively. From these figures it can be seen that the proposed model fits well to the data. The high variations of some data for NLOS is due to the fact that the proposed model does not take into account the number of walls between the transmit and receive antenna and its thickness. The extracted path-loss exponent for all scenarios are summarized in Table 4.1. The minimum path-loss exponent is 1.43 for the case of a corridor which behaves as a waveguide structure. The global path-loss parameters for LOS are $\alpha = 1.79$ and $\sigma = 1.08$ dB and for NLOS $\alpha = 2.61$ and $\sigma = 2.61$ dB. For an industrial environment the global path-loss parameters are for LOS $\alpha = 1.89$ and $\sigma = 1.99$ and for NLOS $\alpha = 4.31$ and $\sigma = 2.17$. The path-loss exponent for the NLOS industrial environment is much higher than that for the indoor environment. This is due to the fact that in the industrial environment and for NLOS the transmitter was mostly placed behind metal stokes or behind a big metal cupboard as can be seen in Figure 4.2. The path-loss statistics for outdoor to indoor scenarios are higher than in indoor office scenarios. This is because all transmitted power is entering the building which can be confirmed by the key-hole effect. Moreover, the path-loss exponent for outdoor-indoor API is close to the free space because a lot of reflections are received due to the dense metals in this building.

For narrow-band indoor communication systems we found $\alpha = 1.6 - 1.8$ for LOS and $\alpha = 4 - 6$ for NLOS as reported in [19]. According to Table 4.1 the

obtained path-loss exponents are in the same range of narrow-band systems for the case of LOS, but they are smaller for NLOS. This is because UWB signals have a good penetration capability through the walls and experience less fading due to the high resolution provided by such signals. The results for path-loss exponent and standard deviation reported in [18] are comparable to the results obtained from our measurements. The reported values in [18] are $\alpha = 1.58$ and $\sigma = 1.91$ for LOS and $\alpha = 2.41$ and $\sigma = 3.26$ for NLOS.

The path-loss exponent for the WPAN scenarios are also given in Table 4.1. The path-loss exponent for LOS scenario was found to be 1.32 and 1.64 for wpan1 and wpan4 case, respectively. It can be concluded that the path-loss exponent is lower than in free space (i.e. $\alpha = 2$). This is mainly due to two effects. One is related to the waveguide effect of multipath components reaching the receive antenna. Another is the near-field effect which introduces extra losses at very short distances; this means that starting from such short distances the received power will decrease with distance slower than in free space. We note that the near-field effect is fully described and modeled in the next chapter. For the NLOS case the path-loss exponent is 0.08-0.09, which is very low. This is because in the wpan1 scenario, a computer monitor was placed between both antennas and for wpan4 the human body is interposing between the antennas. Clearly, the receive antenna was placed quite close to the monitor or the human body; that means that the direct path was completely blocked and hence only reflections of the objects surrounding the scenario reached the antenna.

For the wpan2 case a path-loss exponent of 0.89 and 0.04 was found for DMR and Non-DMR situations (DMR means that maximum radiation was directed to the other antenna). The dependence with distance is stronger for the DMR situation; this is because the direct path is reaching the receive antenna through the table. For short distances the behavior is not the same because when the direct path is blocked, most of the energy is reaching the antenna from far reflectors (far compared with the distance between the antennas). When the distance between the antennas is incremented, the received power will still not change very much, and in extreme situations the received power can be even higher for larger distances (i.e. a negative path-loss exponent can be expected for such case).

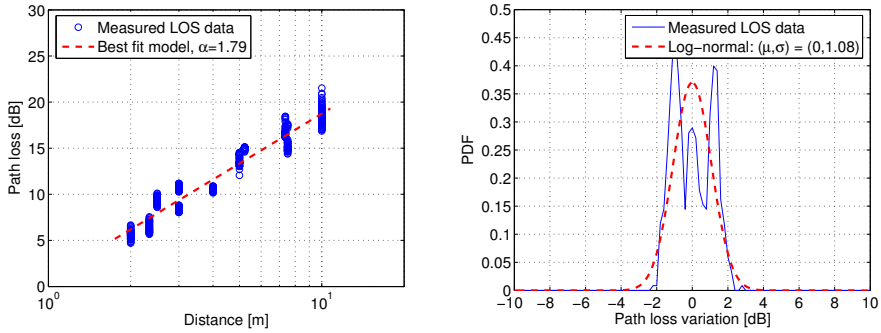

Figure 4.15: *Path-loss measurements and models for indoor LOS propagation.*

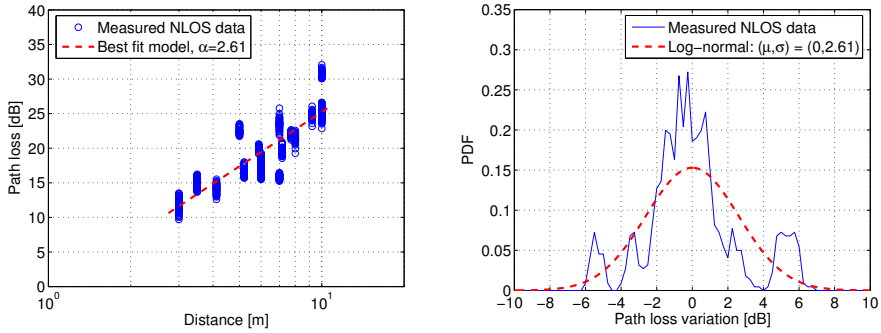

Figure 4.16: *Path-loss measurements and models for indoor NLOS propagation.*

	location		*path-loss exp.*	*std dev.*
	indoor office			
LOS	corridor		1.43	0.78
	office		1.66	0.39
	library		1.57	0.59
	Total		1.79	1.08
NLOS	corridor-office		3.35	1.56
	office-office		2.29	1.78
	library		2.43	0.62
	Total		2.61	2.61
	outdoor-indoor			
	API		1.92	2.46
	Balcony		3.06	3.27
	library		3.30	2.82
	industrial			
	LOS		1.89	1.99
	NLOS		4.31	2.17
	wpan			
	wpan1	LOS	1.32	0.79
		NLOS	0.08	0.54
	wpan2	MDR	0.89	1.01
		N-MDR	0.04	0.60
	wpan3	LOS/NLOS	-	-
		NLOS	-	-
	wpan4	LOS	1.64	0.10
		NLOS	0.09	0.67

Table 4.1: *Large-scale path-loss parameters for indoor office, outdoor-indoor, industrial environment and WPAN scenarios.*

4.3.2 Fading margin model

Small-scale fading in narrow-band communication systems describes the signal drop due to destructive interference of the multipath components at the receiver when sub-wavelength changes are made in the receiver position [19]. Clearly, the energy of the signal is measured at one single frequency and once this frequency is faded due to multipath a large signal drop may be observed. However, since an UWB signal occupies a large bandwidth, it turns out that not all frequencies will be faded. Therefore, no destructive interference will occur over the entire bandwidth of the pulse. To investigate this effect, we define the fading margin parameter γ_{FM} as:

$$\gamma_{FM} = \frac{\gamma_{FM_{(i,j)}}}{\overline{\gamma_{FM}}} \tag{4.15}$$

where

$$\gamma_{FM_{(i,j)}} = \int_{f_c-\frac{B_w}{2}}^{f_c+\frac{B_w}{2}} |R_{(i,j)}(f)|^2 df \tag{4.16}$$

is the fading margin at location i, j within the measured grid, $\overline{\gamma_{FM}}$ is the fading margin averaged over all grid locations, $R_{(i,j)}(f)$ is the FT of the received signal $r_{(i,j)}(t)$ and B_w and f_c are the bandwidth and the center frequency, respectively. This parameter gives a measure of robustness of a signal against small-scale fading. We note that this definition resembles to the signal quality and the mean power gain parameters as defined in [75] and [76], respectively. The fading margin in our case is normalized to the mean value of all measured grid locations in order to combine all data collected in different positions. The fading margin, bandwidth and center frequency can be considered as observations in a stochastic process. Based on these observations, an estimation of the CDF of such process can be made. The steepness of the fading margin CDF can be related to the robustness of the signal. Figure 4.17 shows the CDF's of the fading margin for LOS and NLOS propagation using different bandwidths. From these figures it can be observed that for both LOS and NLOS propagation, the fading margin increases with decreasing bandwidth. For example, the fading margin variation for NLOS is about 25 dB and 3 dB for a bandwidth of 10 MHz and 7.5 GHz, respectively. The results also indicate that the variation in the fading margin for bandwidths of 1 GHz and higher is almost the same which means that a bandwidth of 1 GHz is enough to receive all power and hence mitigate the multipath effect for such indoor environment. Moreover, a similar significant increase of robustness is observed for both LOS and NLOS propagation. This means that even for LOS channels the multipath components contribute remarkably to the fading margin. The statistics of the fading margin using different bandwidth for both LOS and NLOS are given in Tables 8.1 and 4.3. Furthermore, to model the fading margin the distribution of its amplitude $\sqrt{\gamma_{FM}}$ is checked for all used bandwidths. The result shows that the Nakagami distribution gives the best fit to all measured data as can be seen from Figure 4.18. Using the least square method the m-parameter of the

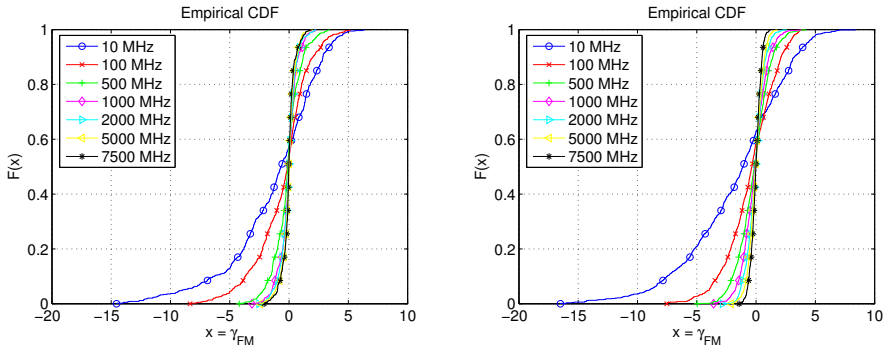

Figure 4.17: *CDF of the fading margin for LOS channels (left), and NLOS channel (right).*

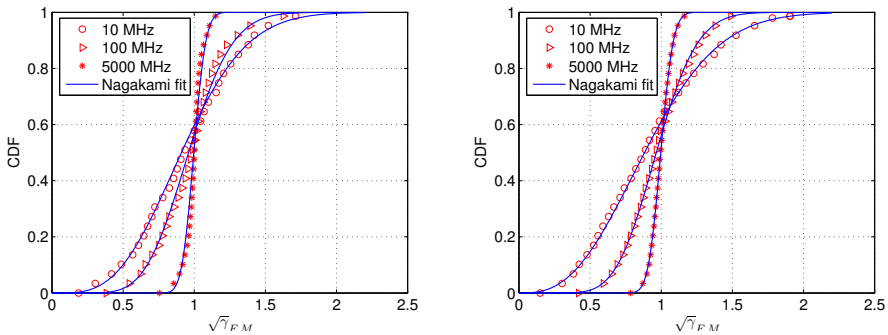

Figure 4.18: *CDF of the fading margin for LOS channels (left), and NLOS channel (right).*

Nakagami distribution is estimated for each used bandwidth. The corresponding estimates are given in Table 8.1 and 4.3 for LOS and NLOS scenario, respectively.

Table 4.2: *Fading margin statistics for LOS propagation.*

B_w [MHz]	$\min(\gamma_{FM})$ [dB]	$\max(\gamma_{FM})$ [dB]	σ [dB]	m [ ]
10	-14.54	6.35	3.75	1.86
100	-8.34	5.14	2.25	4.20
500	-4.20	3.38	1.15	14.48
1000	-3.12	2.25	0.76	33.21
2000	-2.52	2.25	0.69	39.99
5000	-2.43	1.96	0.58	56.46
7500	-2.10	1.87	0.54	64.29

Table 4.3: *Fading margin statistics for NLOS propagation.*

B_w [MHz]	$\min(\gamma_{FM})$ [dB]	$\max(\gamma_{FM})$ [dB]	σ [dB]	m [ ]
10	-16.49	8.38	4.21	1.43
100	-7.52	4.04	2.08	4.83
500	-4.96	4.22	1.32	10.90
1000	-3.57	3.76	1.02	18.09
2000	-2.82	2.58	0.74	34.62
5000	-2.11	1.76	0.60	52.00
7500	-1.43	1.19	0.42	103.78

4.3.3 Small-scale fading model

From each measured position, 49 PDPs have been recorded and averaged to obtain the small-scale averaged power delay profile (SSA-PDP). In order to perform the averaging, the first multipath component is estimated and accordingly, the measured CIR is shifted so that the first arrival time corresponds to a delay of 0 ns. Figure 4.19 shows different received SSA-PDPs for LOS and NLOS cases and different environments. From this figure it can be observed that the multipath components tend to arrive in clusters (i.e. groups).

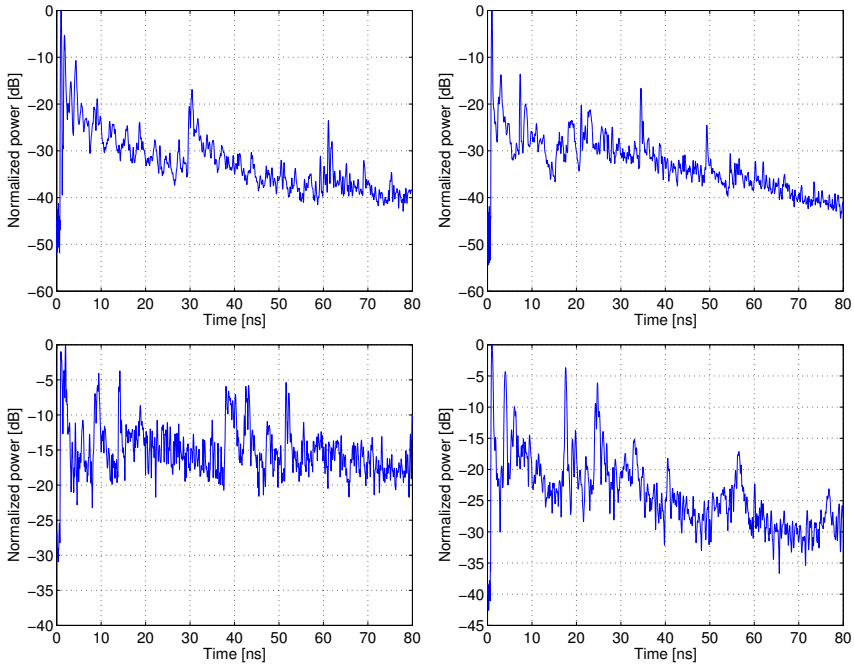

Figure 4.19: *Example of measured SSA-PDP: indoor office (up), outdoor to indoor (down) environments.*

The usual interpretation is that this clustering phenomenon is usually due to closely spaced scatterers in the channel and also is a result of the superstructure of the environment. This may be true, but we think that especially the number and type of walls in the channel are a most significant cause for the occurrence of such phenomenon. This is motivated from the idea that a short duration electromagnetic pulse is propagating toward a homogenous wall of thickness d_w (and by assuming that the duration of this pulse is less than the transient time through the wall) multiple reflections from the finite-sized wall can be observed. Thus, the superposition of all reflections coming from the wall form a behavior of a cluster. In the following, we try to analyze this statement. We assume the

situation depicted in Figure 4.20.

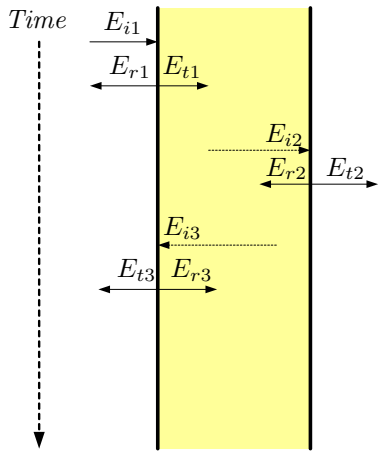

Figure 4.20: *Illustration of multiple pulse reflections inside a wall.*

Assuming a perpendicular wave incident, the reflection coefficient $\Gamma_1(f)$ at the first boundary is defined as the ratio of the first reflection $E_{r1}(f)$ to the incident pulse $E_{i1}(f)$:

$$\Gamma_1(f) = \frac{E_{r1}(f)}{E_{i1}(f)} \tag{4.17}$$

The reflection coefficient in terms of the wave impedance $\eta(f)$ in the layer and the free space wave impedance η_0 is given by:

$$\Gamma_1(f) = \frac{\eta(f) - \eta_0}{\eta(f) + \eta_0} \tag{4.18}$$

In the same way the wave transmitted across the first boundary, $E_{t1}(f)$ is determined by the transmission coefficient $T_1(f)$ across the boundary:

$$T_1(f) = \frac{E_{t1}(f)}{E_{i1}(f)} \tag{4.19}$$

From the boundary condition we know $T_1(f) = 1 + \Gamma_1(f)$:

$$E_{t1}(f) = (1 + \Gamma(f))E_{i1} \tag{4.20}$$

The wave incident to the second boundary, $E_{i2}(f)$ is related to the wave transmitted through the first boundary by:

$$E_{i2}(f) = E_{t1}(f)e^{-\gamma_w(f)d_w} \tag{4.21}$$

where d_w is the thickness of the wall and $\gamma_w(f)$ is the attenuation constant in the wall material. The added complex exponential factor is therefore due to the propagation through the material. The reflection at the rear boundary equals:

$$\Gamma_2(f) = \frac{E_{r2}(f)}{E_{i2}(f)} = -\Gamma_1(f) \tag{4.22}$$

The reflected pulse from the second boundary of the wall can be expressed as:

$$E_{r2}(f) = \Gamma_2(f)E_{i2}(f) = -\Gamma_1(f)E_{i2}(f) \tag{4.23}$$

The incident signal from inside the wall, at the first boundary becomes:

$$E_{i3}(f) = E_{r2}(f)e^{-\gamma_w(f)d_w} \tag{4.24}$$

The transmitted wave at the first boundary is now:

$$E_{t3}(f) = T_3E_{i3}(f) \tag{4.25}$$

Using the boundary condition

$$T_3(f) = 1 + \Gamma_2(f) = 1 - \Gamma_1(f) \tag{4.26}$$

$$E_{t3}(f) = (1 - \Gamma_1(f))E_{i3}(f) \tag{4.27}$$

and combining previous equations we get:

$$E_{t3}(f) = \Gamma_1(f)(1 - \Gamma_1^2(f))e^{-2\gamma_w(f)d_w}E_{r1}(f) \tag{4.28}$$

To emphasize the phenomena we have assumed contributions from the first $E_{r1}(f)$ and second $E_{t3}(f)$ reflection terms only. From a similar approach, a closed form for all reflections can be derived. In the following, we try to verify whether such phenomena occur when a real wall is present. To this end, a wall made of plaster with a thickness $d_w = 7$ cm has been used as shown in Figures 4.21 and 4.22. First the propagation delay of the pulse through the wall has been measured. This was done by measuring the LOS path between the antennas without and with the wall. The results are shown in Figure 4.21 (right) from which an additional through wall propagation delay $\Delta\tau$ of about 180 ps is found.

The case of a single wall as depicted in Figure 4.22 (left) gives the measured signal as shown in Figure 4.23 (left). This signal consists of a series of reflected pulses from the wall forming a behavior which looks like a cluster. For instance, the first pulse is reflected from the first wall boundary and a second one is reflected after its propagation inside the wall and reflected back from the second wall boundary. The time difference between these two pulse reflections is about 800 ps. The expected one yields:

$$\widehat{\Delta t} = 2\left(\Delta\tau + \frac{d}{c}\right) = 2 \cdot \left(180 \cdot 10^{-12} + \frac{7 \cdot 10^{-2}}{3 \cdot 10^8}\right) \simeq 826 \text{ ps} \tag{4.29}$$

which is near the measured value. Next, we assume the scenario of two walls separated by 25 cm from each other as depicted in Figure 4.22 (right). In this case, two clusters are expected according to the previous analysis. The results of two walls are given in Figure 4.23 (right). Indeed, from this figure two separate clusters are observed. Because the walls are separated by $d = 25$ cm, it means that the time difference $\widehat{\Delta t}$ between the second reflected pulse from the first wall and the first reflection from the second wall should be equal to:

$$\widehat{\Delta t} = 2\left(\frac{d_w}{c}\right) = 2 \cdot \left(\frac{25 \cdot 10^{-2}}{3 \cdot 10^{8}}\right) \simeq 1.5 \text{ ns} \tag{4.30}$$

which is near the 1.48 ns value indicated in Figure 4.23 (right). According to this, it can be concluded that the number of clusters in an UWB power delay profile is related to the number of walls seen by the antennas. However, strong reflections due to large reflectors along the channel, e.g. metal cupboard, can also result into a cluster. It turns out that it is hard to prove that only walls are the cause for the clustering phenomena. For this reason, all clusters caused by whatever reflectors (walls, furniture, ..) are considered in our analysis connected to the modeling of the UWB channel.

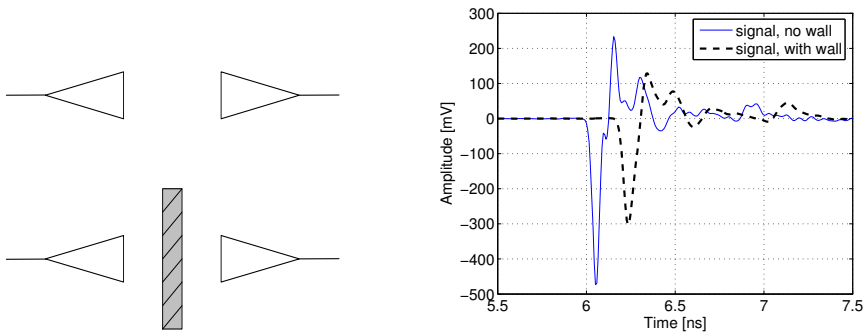

Figure 4.21: *Measured LOS signal without and with wall between the antennas.*

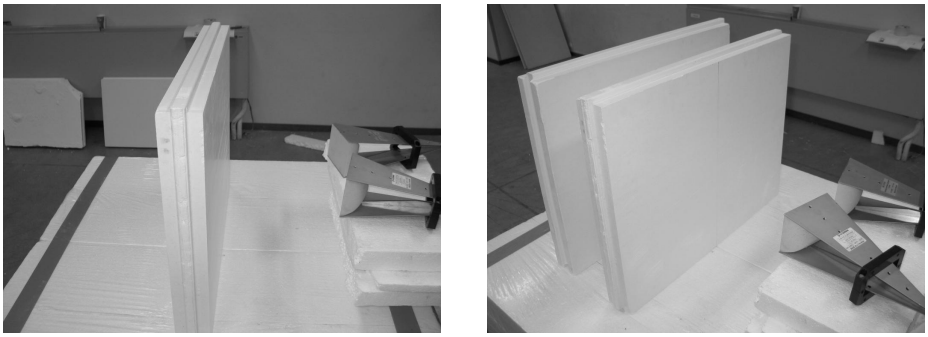

Figure 4.22: *Illustration of a single wall scenario (left) and two walls scenario (right).*

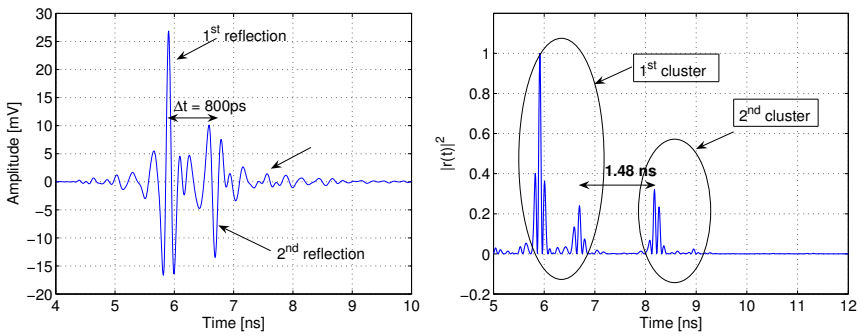

Figure 4.23: *Measured signal reflected from a single wall (left) and a two walls (right) model and filtered from 3.1 to 10.6 GHz. $|r^2(t)|$ is used in the figure (right), rather than $r(t)$ in the figure (left), to show clear clusters.*

Clustering channel model

Based upon the apparent existence of those clusters in our measurement data, we adopt the well-known Saleh-Valenzuela (S-V) model as a starting point in our UWB channel modeling. This model has been proposed for wide-band channels [30,31], and has been adopted later by the IEEE 802.15.3a channel modeling subgroup as an UWB channel model for small-scale fading [77]. In the S-V model the multipath components are modeled as a number of rays arriving within different clusters, which can be expressed as follows:

$$h(t) = \sum_{l=0}^{L-1} \sum_{k=0}^{K_l-1} a_{l,k} \delta \left(t - T_l - \tau_{l,k}\right) \tag{4.31}$$

where $\delta(.)$ is the Dirac delta function, L is the number of clusters, K_l is the number of multipath components within the lth cluster, $a_{l,k}$ is the multipath gain coefficient of the kth component in the lth cluster, T_l is the delay of the lth cluster which is defined as the time of arrival of the first arriving multipath component of the cluster, $\tau_{l,k}$ is the delay of the kth multipath component relative to cluster arrival time T_l.

Statistics of channel model parameters

To complete the clustering channel model given in equation (4.31), the statistics of its parameters have been extracted from the measured data. The parameters can be categorized as inter-cluster parameters (i.e. L, T_l) and intra-cluster parameters (i.e. K_l, $\tau_{l,k}$, $a_{l,k}$). To retrieve these parameters, it is necessary to identify the clusters in each power delay profile. Different ways exist to identify the clusters [44], however, these methods are not robust. Here, the clusters are identified by visual inspection of the measured SSA-PDP similar to [11, 30, 31, 40, 44].

Distribution of the number of clusters and multipath components

The average number of clusters $\overline{L}$ is about 3.3 and 5.5 for LOS and NLOS scenarios, respectively. A higher number of clusters for NLOS might be due to the furniture in the environment especially for the measurements performed from office to office. Figure 4.24 shows the histogram of the number of clusters for both LOS and NLOS propagation. Figure 4.25 gives the CDF of the number of paths K_l per cluster for LOS and NLOS cases. These graphs reveal that the parameter K_l can be closely modeled by an exponential distribution where μ_{K_l} is its mean. The value of μ_{K_l} are given in Figure 4.25 and also in Table 4.4. The obtained μ_{K_l} is lower than that reported in [40]. This might be due to the fact that in the reported analysis they used the D-CIR method and not the MD method which is used here. In general, μ_{K_l} increases from LOS and NLOS and it depends on the separation distance between the transmit and receive antennas, the physical structure of the channel and of course on the threshold level setting as discussed earlier.

Cluster and ray power decay constants

The average power decay profile $\overline{a_{l,k}^2}$ at $T_l + \tau_{k,l}$ is given by:

$$\overline{a_{l,k}^2} = \overline{a_{0,0}^2} \exp\left[-\frac{T_l}{\Gamma}\right] \exp\left[-\frac{\tau_{k,l}}{\gamma}\right] \tag{4.32}$$

where $\overline{a_{0,0}^2}$ is the expected value of the power of the first arriving multipath component, Γ and γ are the power decay constant for the clusters and rays, respectively.

In order to extract the cluster power decay constant Γ, the received PDP is normalized to the received power of the first multipath of the first cluster $a_{0,0}^2$. Then,

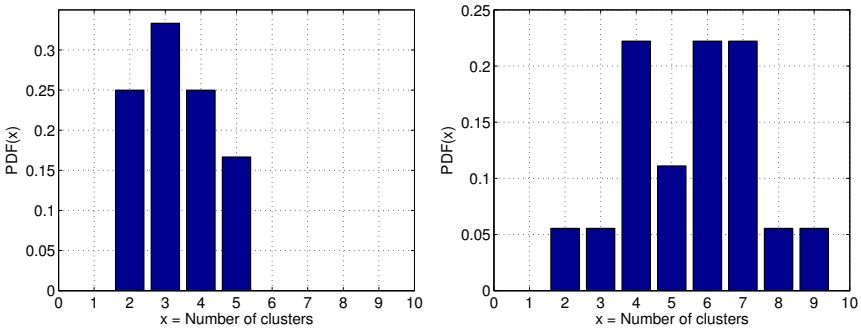

Figure 4.24: *Histogram of the number of clusters for LOS (left) and NLOS (right) scenarios.*

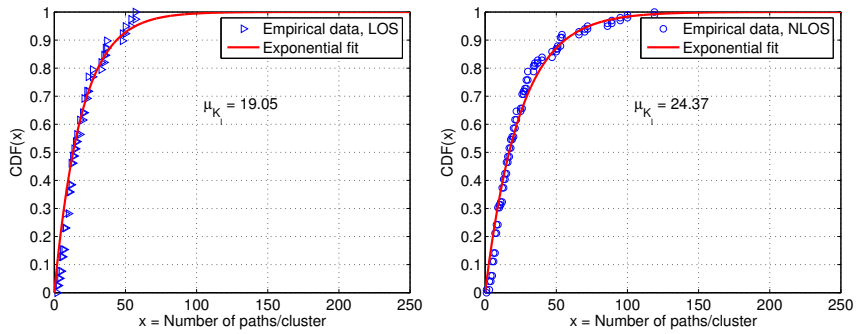

Figure 4.25: *CDF of the number of multipath components per cluster for LOS (left) and NLOS (right) scenarios.*

the cluster arrivals of the PDPs are combined together and plotted. The value of Γ is estimated from the plot by using least square curve fitting. Figure 4.26 shows the obtained results for cluster power time decay constants for LOS and NLOS propagation. The power decay constants in case of LOS and NLOS propagation are given in Table 4.4. From the figure it can be observed that the obtained value of Γ for the NLOS case is higher than for LOS. This is due to: 1) the fact that for the LOS case the first path is usually the strongest path and 2) the fact that the first path for a NLOS channel is more attenuated, and even when it is the strongest path, the difference between the received power of the clusters within a PDP is often small when compared to the LOS case. The reported values of Γ are in the range of 22-24 ns for LOS and 36-52 ns for NLOS [68]. The UWB channels recovered in our measurements exhibit higher decay rates which means that this parameter depends on the building architecture, as also confirmed in [11].

From the measured data the ray power decay constant is extracted by normalizing each cluster to its first multipath component: the first arrival of each

Table 4.4: *The estimated parameters for different proposed models.*

Parameter	LOS	NLOS
$\overline{L}$	3	5
μ_{K_l}	19.05	24.37
Γ [ns]	9.93	20.15
γ [ns]	12.01	9.76

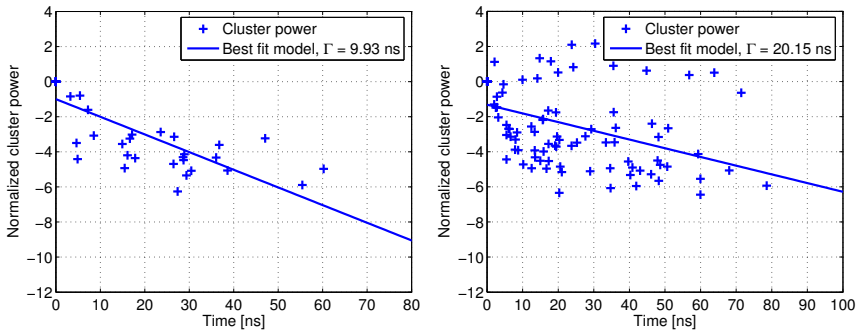

Figure 4.26: *Normalized cluster relative power as a function of relative cluster delay for LOS (left) and NLOS (right) propagation.*

cluster is set to a time zero and amplitude one. Accordingly, all other ray arrivals within the cluster are adjusted and combined together. Again, the value of γ is estimated using minimum least square error curve fitting. The results for LOS and NLOS propagation are shown in Figure 4.27. From this figure we see that the retrieved γ are higher for NLOS cases because the received paths within a cluster experience almost the same attenuation. In addition to this, we noticed that the ray power decay constant is higher than the cluster decay constant. This might be due to the structure of the channel, but we think it is also due to the superposition of all clusters because the time window as well as the number of multipath components within each cluster are totally different. This will provide some interference between multipath components. This interpretation can be used to explain the similar behavior for γ as given in [11]. For this purpose we estimated the parameter γ for each cluster separately. Plots of the CDF of γ and its mean are shown in Figure 4.28. From these results it can be concluded that a huge difference, 16.37 ns to 12.01 ns for LOS and 24.18 ns to 9.76 ns for NLOS, exists between the two methods for extracting the value of γ which is given in Table 4.4. Moreover, in the S-V model the ray power decay constant is considered to be the same for all clusters and hence an average of γ can be considered as a good estimate. However, inspection of some data shows that in our scenarios this

is not the case, namely γ will vary with the delay. This has been also observed in [44]. This effect can be modeled as a linear relationship between γ and the delay, that is:

$$\gamma = \alpha_{TDC}\tau \tag{4.33}$$

where α_{TDC} is a constant to be determined. Using the minimum least-square error method, the value of α_{DTC} is estimated for both LOS and NLOS channels as shown in Figure 4.29.

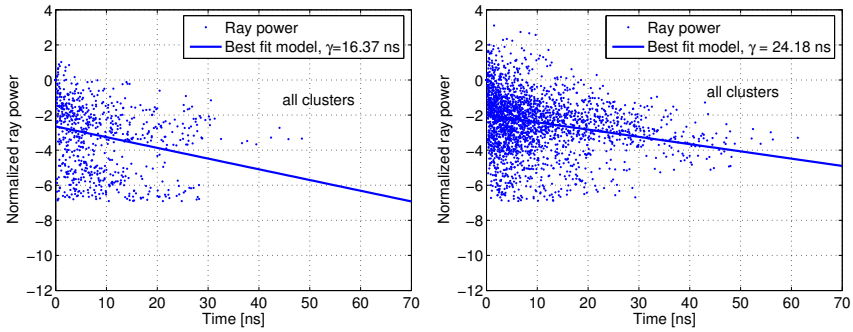

Figure 4.27: *Normalized ray power as a function of relative ray delay for LOS (left) and NLOS (right) propagation.*

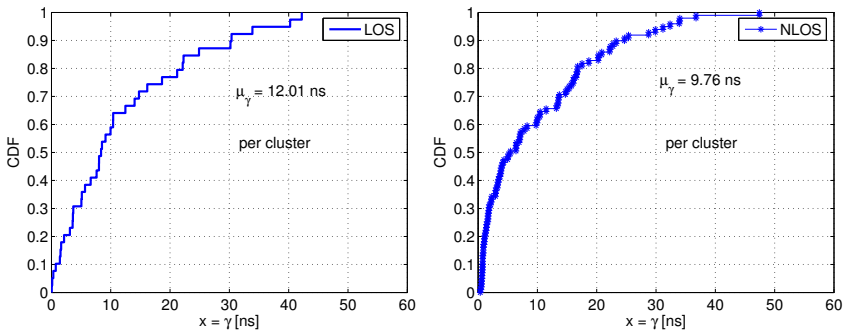

Figure 4.28: *The CDF of the ray power decay constant γ for LOS (left) and NLOS (right) propagation.*

Cluster and ray arrival rates

The inter-cluster arrival times T_l and the intra-cluster arrival times $\tau_{l,k}$ are usually modelled as Poisson processes according to the distribution:

$$p(T_l|T_{l-1}) = \Lambda \exp\left[-\Lambda(T_l - T_{l-1})\right] \tag{4.34}$$

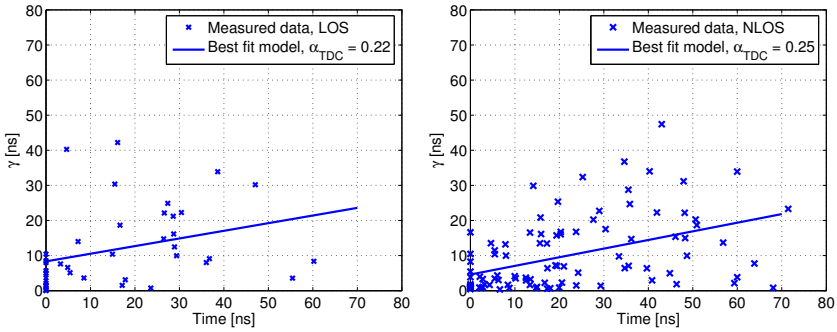

Figure 4.29: *The ray power decay constant γ as a function of delay for LOS (left) and NLOS (right) propagation.*

$$p(\tau_{l,k}|\tau_{l,k-1}) = \lambda \exp\left[-\lambda(\tau_{l,k} - \tau_{l,k-1})\right] \tag{4.35}$$

where Λ is the mean cluster arrival rate and λ is the mean ray arrival rate. The cluster inter-arrival times are obtained by subtracting the arrival times of each two consecutive clusters. Consequently, the conditional probability distribution given in equation (4.34) is estimated. Estimates of the cluster arrival rate is done by fitting the cluster arrival times to an exponential distribution and the corresponding results are given in Table 4.5. However, it seems that this model does not fit well the measured data. Therefore, different distributions have been applied to the data and the Gamma distribution seems to give the best fit and hence this distribution is proposed to model the cluster arrival times. The Gamma distribution model is expressed as:

$$f(x) = \frac{(x/\beta)^{\alpha-1}}{\beta G(\alpha)} \exp\left[-\frac{x}{\beta}\right] \tag{4.36}$$

where $G(\alpha)$ is the Gamma-function, given by

$$G(\alpha) = \int_0^\infty \alpha^{m-1} e^{-t} dt \qquad m >= 0 \tag{4.37}$$

and α, β are model parameters to be estimated. Their extracted values for both LOS and NLOS are given in Table 4.5. Figure 4.30 shows that the measured cluster inter-arrival times agree well with the proposed model. The measured ray intra-arrival times are shown in Figure 4.31. Using the single Poisson process, the arrival rate is estimated and given in Table 4.5. The results show that the measured ray intra-arrival times deviate much more from the single Poisson process model and hence a model based on a mixture of two Poisson processes is proposed [68]. The probability density function of two mixed Poisson processes is expressed as:

$$p(\tau_{l,k}|\tau_{l,k-1}) = b\lambda_1 \exp\left[-\lambda_1(\tau_{l,k} - \tau_{l,k-1})\right]$$

$$+(1-b)\lambda_2 \exp\left[-\lambda_2(\tau_{k,l}-\tau_{k,l-1})\right] \tag{4.38}$$

where λ_1 and λ_2 are the ray arrival rates, while the constant b is the so-called mixing probability which is less than or equal to unity. These parameters are extracted using least squares curve fitting and the corresponding parameters are cited in Table 4.5. Figure 4.31 compares the single and mixed Poisson process models. From this figure it can be observed that the Mixed Poisson model provides a better estimation of the ray intra-arrival times. According to [68], the discrepancy between the single and mixed Poisson models are due to the frequency dependency of the UWB propagation channels, i.e. different frequency components of the UWB signal experience a different attenuation across the bandwidth, or a frequency selectivity in the channel or both. However, it may also be due to the fact that the cluster does not end immediately when the next cluster starts. This means that some multipath components belonging to a cluster are received or considered as multipath components of the next cluster. Thus, it seems that the multipath components are mixed together and hence a mixed model will give a better description.

Table 4.5: *The estimated parameters for different proposed models.*

Parameter	LOS	NLOS
$1/\Lambda$ [ns]	16.49	10.35
$1/\lambda$ [ns]	0.88	0.51
(α,β)	(2.03,8.1)	(2.02,5.12)
$(b,1/\lambda_1,1/\lambda_2)$	(0.91,0.53,3.51)	(0.96,0.39,2.17)

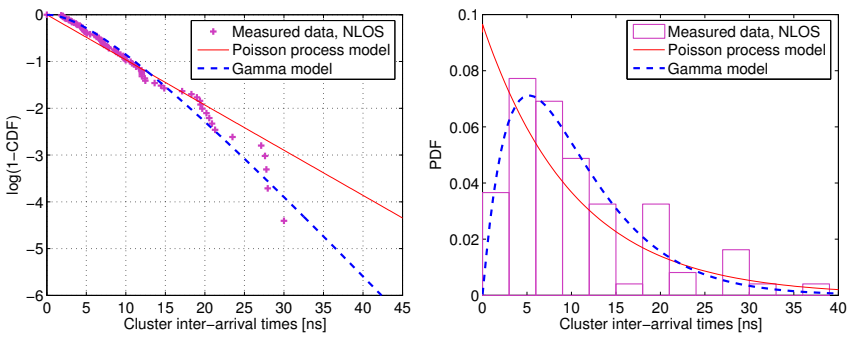

Figure 4.30: *The cluster inter-arrival times: Logarithmic CDF (left) and its PDF (right).*

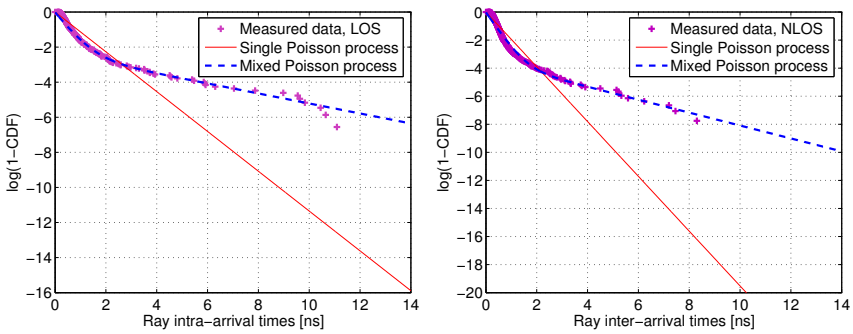

Figure 4.31: *Logarithmic CDF of the ray intra-arrival times, LOS and NLOS*

Statistics of the fading envelope

To evaluate the small-scale amplitude fading statistics, the amplitudes over small-scale areas (i.e. measured over the grid) are used. As in our analysis the MD method has been used, the channel path gain seems to be estimated with an infinite bandwidth. This put a limitation in the evaluation of the amplitude fading since we have to combine different channel path gains for different measured CIR within the grid. Therefore, we have divided the time axis into bins and each estimated path is put in one bin according to its delay. The width of each bin is equal to 134 ps (i.e $1/B_w$). Moreover, since for each location 49 measurements were performed, we only have a maximum of 49 samples in each bin (usually less because of the higher time resolution). Therefore, to perform a good statistical analysis of the amplitude fading, all data is combined, resulting in a so-called global distribution. Clearly, the distribution fitting is conducted by normalizing the random variables $a_{k,l}^2$ by the expected power $\overline{a_{k,l}^2}$ associated to the same location. With this normalization, the samples in all locations can be combined and approximated as one sufficiently large homogenous data pool. According to this approach, the path-loss and shadowing effects are excluded from the data. We note that we preferred this normalization rather than normalizing the energy of each measured CIR to unity. This is because by using the first normalization we still keep the effect of small-scale fading over the whole grid which is not the case when normalizing the CIR energy.

A fitting test on the statistics of the fading envelope for each bin has been performed using some widely known theoretical models such as: Rayleigh, Rice, Log-normal, Nakagami and Weibull distributions. For the fitting test we used both the Kolmogorov-Smirnov (K-S) and Chi-square (χ^2) hypothesis tests to elaborate the goodness of fit of these distributions with 5% significance level [78]. The average passing rates of the K-S and χ^2 for both LOS and NLOS are given in Table 4.6. From this table we can see that the Log-normal distribution has the highest passing rate and hence the small-scale fading can be modeled by such

Table 4.6: *Passing rates of K-S and χ^2 hypothesis tests at a 5% significance level for LOS and NLOS propagation.*

Distribution	LOS		NLOS	
	K-S (%)	χ^2 (%)	*K-S* (%)	χ^2 (%)
Rayleigh	7.12	1.42	8.33	1.50
Rician	31.35	9.73	25.83	7.83
Lognormal	81.23	50.59	83.50	58.50
Nakagami	55.81	28.02	36.16	16.66
Weibull	55.10	15.43	37.66	8.166

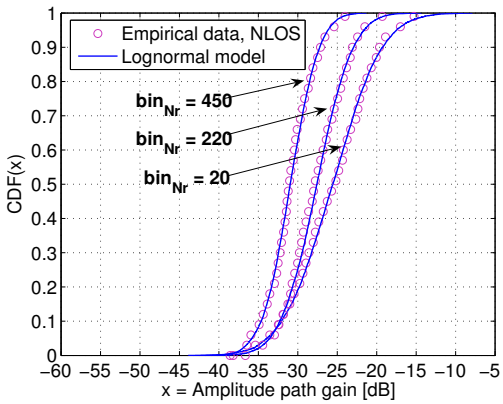

Figure 4.32: *CDFs of the global empirical small-scale amplitude fading fitted to a Log-normal distribution for different delay bins.*

distribution. This result confirms the fading distribution of the channel model proposed by the IEEE [77]. The measurement results reported in [79] show that the fading amplitudes can be well modeled by Log-normal, Weibull as well as Nakagami distributions. Figure 4.32 shows the CDFs of the global empirical small-scale amplitude fading fitted to the Log-normal distribution for different delay bins for NLOS propagation. The variation of the mean and the standard deviation of the Log-normal distribution is investigated and the result is shown in Figure 4.33. From this figure it can be observed that the Log-normal statistics linearly decrease with excess delay.

4.3.4 Roughness model

In this section, the results of the roughness scenario described in section (4.1) are given. The UWB received power is investigated using stones with different sizes, types and volumes. For the measurements, an acquisition time window of 5 ns is used with 1024 measuring points which means that the received signal is sampled

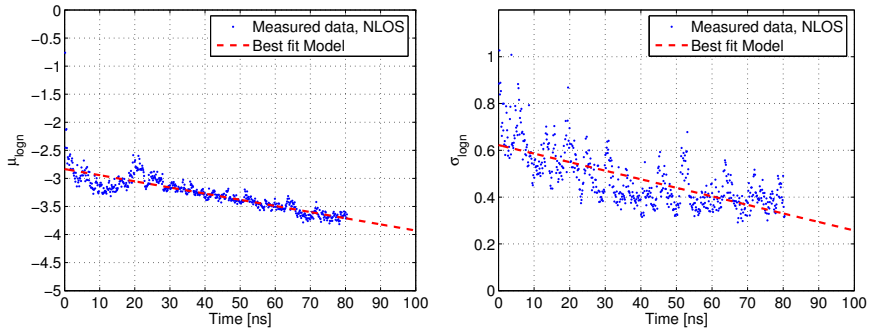

Figure 4.33: *Variation of the Log-normal statistics as a function of the excess delay, mean (left) and standard deviation (right).*

at a rate of 1 sample per 5 ps. Figure 4.34 (left) shows the received signal when no stones are present. From this figure it can be seen that the signal consists of two main pulses. The first pulse is due to coupling between the antennas which is used to correct any time shift of the signal as the position of the antennas is kept the same. The second pulse is the reflection coming from the surface and is used as a reference for different rough surfaces. The measured signal is first filtered over the antenna bandwidth, i.e. 2-8 GHz and only the reflection from the surface is selected for further analysis using time gating. Figure 4.34 (right) shows an example of the measured surface reflection when quartz stones are used with a volume of 0.5 l.

The measured power, averaged over all repeated trials, as function of volume and size of the stones is shown in Figure 4.35. From this figure it can be observed that the received power decreases when the volume of the stones increases. Due to scattering from the stones, the scattered signals will have different phases and their summation rises to a destruction of the total signal power. Experiments also learn that the received power is smaller for large stones because in case of large stones the field is scattered in all directions. This means that the received waves will experience large variations in phase which influence the received power, while the antenna collects the energy only in its pattern region. However, for small stones the length of the scattering vectors is smaller plus the signal penetration through stones is easier than for large stones and hence more reflection from the surface is received. From the results it can concluded that the type of stones influences the received power. Clearly, for a fix stone size of 4-8 mm, the broken quartz stones show a stronger effect than the quartz stones. This effect is because when broken stones are used more diffraction is occurring due to the sharp edges.

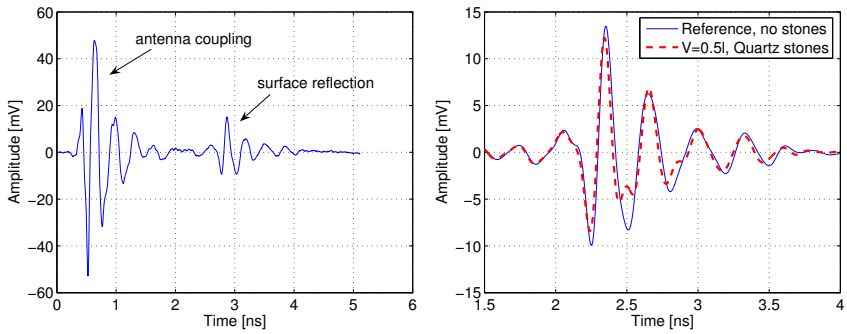

Figure 4.34: *Measured signal: reference (left), reflected from Quartz stones of 0.5 l volume (right).*

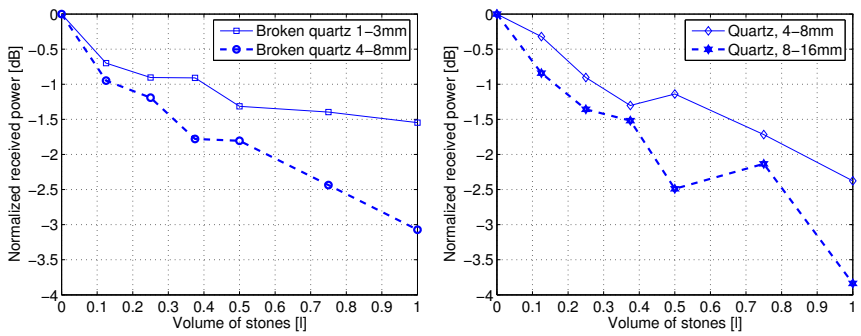

Figure 4.35: *The average measured power as a function of stone volume for different sizes and types of the stones.*

4.3.5 Time dispersion model

The time dispersion parameters indicate how the received power is distributed with respect to time. Delay spreads restrict transmitted data rates and could limit the capacity of the system. The definition of the time dispersion parameters have been given in Chapter 2. Figure 4.36 gives the CDFs of the RDS for LOS and NLOS indoor office environments. From this figure it can be seen that the data fits very well with the normal distribution. The RDS statistics for all environments are extracted and given in Table 4.7.

From this table we observe that for the LOS case the RDS is smaller than for office and library rooms. This is because the corridor can be seen as wave-guide which means that all important reflections are received at the same time in the beginning of the PDP. Moreover, the RDS for the library (LOS) is higher than that in the office. This can be explained by the fact that the dimensions of the library room are larger than those for the office room. Clearly, in the library room the

multipath components arrive much later than the LOS components. This result confirms our expectation of the dependency of the RDS on the dimensions of the rooms where the measurements were taken. The obtained RDS values for NLOS are higher than those for LOS because the direct path is usually not the strongest path due to the obstructions. The mean RDS for LOS and NLOS are about 8.61 ns and 13.40 ns for the office environment, and 14.17 ns and 21.03 ns for the industrial area, respectively. The RDS in an industrial area is much higher than that for the office environment and this is because of high reflections received from densely placed metal objects. This can also be justified for the outdoor-to-indoor API measurements. Moreover, the obtained RDS for the LOS WPAN scenario is very small (i.e. 1.2 ns) because the antennas are very close to each other which means that the direct path is expected to be much stronger than all reflections surrounding the channel. In fact these reflections can be neglected regarding their powers relative to the direct path and hence the RDS converges to very small values.

From Table 4.7 it can be concluded that under the same channel conditions the RDS has a strong relation with distance. This is because when the distance is incremented a large number of multipath components is received. This might also be the case for smaller distances but those multipath components have small strengths compared to the LOS component. Figure 4.37 shows the variation of RDS with distance for both LOS and NLOS. This variation can be linearly modeled and the best fit model is given in the same figure. It can be observed that the RDS-distance dependency is higher for NLOS than LOS. This is because for NLOS cases the number of objects surrounding the channel is much more and hence more reflections can occur.

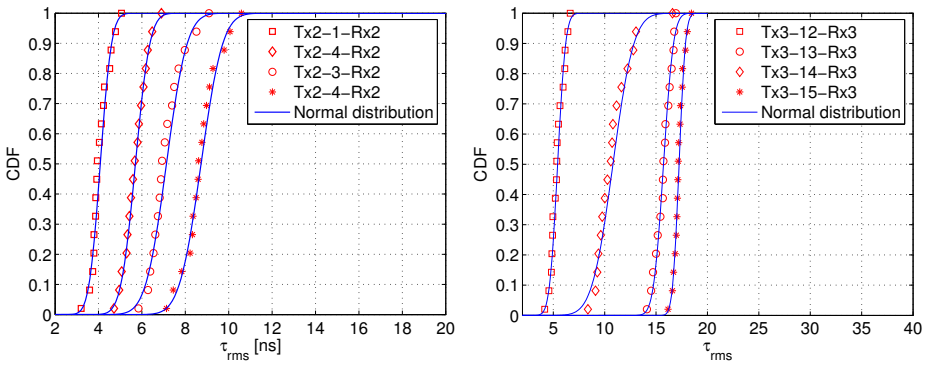

Figure 4.36: *The obtained CDF of the RDS for indoor office LOS (corridor) and NLOS (corridor-office) propagation. Positions are indicated in Figure 4.1*

location		*d*	*mean*	*std dev.*	*min*	*max*
indoor office						
LOS	corridor	2.50	4.081	0.407	3.202	5.058
		5.00	5.699	0.524	4.713	6.897
		7.50	7.129	0.750	5.841	9.090
		10.00	8.725	0.7134	7.134	10.583
	office	2.00	6.020	0.472	5.001	7.395
		4.00	9.119	0.411	8.273	9.933
		3.00	7.791	0.299	7.047	8.348
		2.34	7.889	0.569	6.793	8.988
	library	3.00	7.638	0.633	6.438	9.773
		5.22	10.862	1.0262	8.662	13.456
		7.36	14.445	1.289	12.039	17.638
		10.00	13.969	1.134	12.310	17.173
total		2.00-10.00	8.614	3.095	3.202	17.638
NLOS	corridor-office	3.00	5.421	0.6178	4.166	6.647
		5.00	15.725	0.764	14.111	16.929
		7.00	10.804	1.601	8.371	16.602
		10.00	17.237	0.491	16.160	18.444
	office-office	3.00	7.509	0.857	5.730	9.756
		4.12	10.403	0.958	8.281	13.556
		5.20	12.515	1.070	10.707	14.957
		3.50	10.783	1.240	8.439	12.695
		6.00	11.631	0.772	9.906	13.055
		7.00	11.868	0.698	10.484	13.950
		6.00	13.518	0.944	11.266	14.872
		7.16	12.247	0.851	10.621	13.991
		8.00	15.021	0.781	13.590	16.842
		9.22	16.594	0.861	14.979	18.268
		10.00	15.431	0.851	13.300	16.973
	library	5.88	16.175	0.588	14.915	17.422
		7.73	18.033	0.739	16.238	19.418
		10.00	20.404	1.096	18.766	22.736
total		3.00-10.00	13.407	3.792	4.166	22.736
industrial						
LOS		2.22-22.36	14.172	3.732	5.877	23.260
NLOS		5.75-29.69	21.031	2.418	12.280	24.932
outdoor-indoor						
API		9.51-15.2	13.039	6.990	1.897	24.107
Balcony		6.34-13.7	5.963	3.348	1.000	14.041
library		6.35-8.74	4.714	2.897	0.981	11.973
wpan						
LOS		0.05-1.00	1.256	0.616	0.096	2.428
NLOS		0.30-1.27	10.544	4.656	1.673	17.506

Table 4.7: *RDS and its statistics for all measured environments, all units are in [ns] except d in [m].*

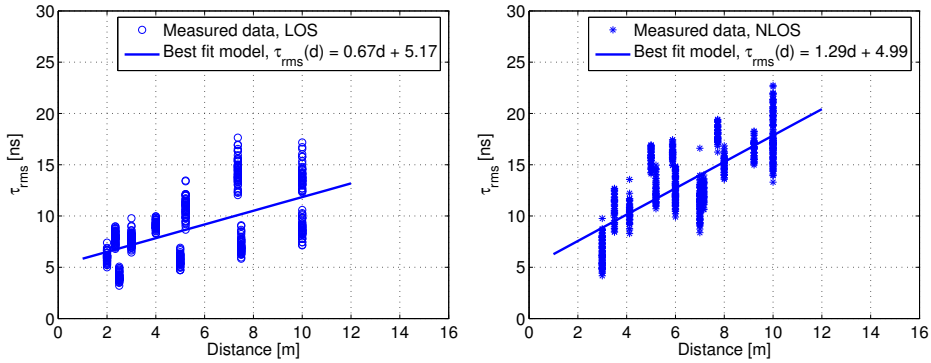

Figure 4.37: *RDS as function of distance for indoor office LOS and NLOS propagation (all data).*

4.4 Chapter summary

In this chapter, the results of extensive UWB measurements carried out in different environments have been presented and statistical propagation models for the UWB channel covering the frequency band from 3.1 to 10.6 GHz have been proposed. The measurements were conducted in different environments at the TU Delft campus: indoor office, industrial area, outdoor to indoor and WPAN applications, for both LOS and NLOS. In total around 3000 channel impulse responses have been gathered which allows for a good statistical analysis.

The UWB-CIR can be estimated using inverse filtering together with the maximum detection method. This method provides better results than the conventional D-CIR method adopted by most researchers. The D-CIR is more convenient for the wide-band channel because the chance that all delay bins are occupied is high and hence a tapped delay line model is more applicable. It turns out that if the D-CIR method is used for a dense multipath channel, the concept of the ray arrival rate will lose its meaning and also the concept of high bandwidth resolution. This aspect has an important effect on the statistics of the UWB channel, however has been ignored by other researchers.

The UWB signals are robust against fading. The difference in the fading margin was found to be around 20 dB when the bandwidth is decremented from 7.5 GHz to 10 MHz. The results also indicate that using a bandwidth of about 1 GHz is enough to resolve all paths and hence mitigate the multipath fading effect. The amplitude of the fading margin can be accurately modeled by the Nakagami distribution.

Large and small-scale fading of the UWB channel have been modeled. For instance, the proposed path-loss model shows a good agreement with the measured

data for all measured locations including LOS and NLOS propagation paths. The variations of the path-loss around the proposed model follow a lognormal distribution. The path-loss exponent for the LOS case is less than 2 (value of 2 corresponds to free space spatial expansion) for all environments. The path-loss exponent for WPAN is smaller because of the near-field effect, however for the NLOS it is around 0 because the direct path is totally blocked and the power is received from wall reflections only or from objects near the antennas. This aspect of UWB signal propagation for short-range applications is analyzed in the next Chapter 5.

Statistical analysis of the measured data has learned that the UWB-CIR can be modeled by the S-V model but with some modifications. It has been shown that the number of clusters is related to the number of walls seen by the transmit and receive antennas. This effect has an important impact on the UWB channel clustering statistics and consequently for the UWB system design. The parameters of the clustering model are carefully extracted. The cluster power decay constant for NLOS is higher than that for LOS. This is because the first path is usually not the strongest path. The ray power decay constant strongly depends on the method used to extract it. The superposition of all clusters might give an overestimation of this parameter. Our evaluation can be confirmed by extremely higher values reported in the literature. The best way to retrieve such parameter is to compute it for each cluster and then combine the results by taking its mean. The ray intra-arrival times are modeled by a mixture of two Poisson processes rather than a single Poisson process. The small-scale amplitude fading distribution was determined by using the K-S and χ^2 goodness of fit tests with a confidential level of 5% and is modeled by the lognormal distribution.

The RDS for indoor office environment is found to be 8 and 13 ns for LOS and NLOS propagation and it is higher for rooms with larger dimensions. The RDS statistics for industrial areas are higher than those for the office environment due to the multipath density caused by dense metal objects in the channel. The RDS is lower for the WPAN LOS scenario because the difference in the travel time between the direct path and the reflection is large. Strong dependency was found between the RDS and the distance for indoor office environments.

Roughness measurements have been conducted using stones with different sizes and types. Obtained results confirm the capability of using UWB signals to recognize rough surfaces.

Chapter 5

Analysis and Modeling of Short-Range UWB Channels

5.1 Introduction

The restriction in the maximum transmitted power spectral density (PSD) imposed by the FCC makes UWB technology suitable for many applications such as wireless personal area networks (WPAN). However, in these applications, transmit and receive antennas can be very close to each other and the far-field condition assumed in most of the link budget models may not be satisfied. Clearly, the common link budget models are not valid in this case because the near-field behavior of the antennas is quite different from the behavior in the far-field. In the far-field, plane wave propagation and a constant ratio between the electric and magnetic field, given by the wave impedance, is assumed. In the near-field region, however different effects such as reactive fields, phase errors, and even reradiation between antennas may become important and hence variations in the link budget and change of pulse shape when compared to the far-field, can be observed.

The design and implementation of short-range UWB communication systems need accurate channel models in order to optimize the transmit power and to estimate the coverage. Several UWB measurement results for WPAN applications are reported in the literature [45–55, 72]. In [46], the human body effect on UWB signal propagation is investigated, but only for the receive antenna near the body and the transmit antenna is in the far-field. In [47], UWB channel measurements for a Body Area Network (BAN) are presented where transmit and receive antenna are placed directly on the body; but only the 3-6 GHz band was measured. Reference [72] shows the results of a set of time-domain UWB measurements for very short distances. In spite of plenty of UWB measurement efforts for short-range UWB applications, the analysis of near-field aspects and

its effect on the link budget model has not received much attention.

In this chapter, an empirical UWB link budget model for short-range applications is proposed and validated with measurements and simulations using different types of antennas. The near-field effects and its consequences on the UWB link budget are analyzed and its behavior is modeled.

5.2 Near-field effects analysis

Different near-field criteria have been established based on several effects that may appear in this region [80]. In this section, the effect of these phenomena on the received power is analyzed.

5.2.1 Phase error

The near-field criterion associated to phase error is restricted to the fact that an incident spherical wave differs from a plane wave in a given fraction of the wavelength λ_w. When transmit and receive antennas are close to each other, the rays of the spherical wave produced by the transmit antenna reach different parts of the receive antenna aperture with different ray path lengths (maximum Δr_{max} not negligible compared to λ_w and so with phases as shown in Figure 5.1. This affects the received power because the rays do not sum up coherently at

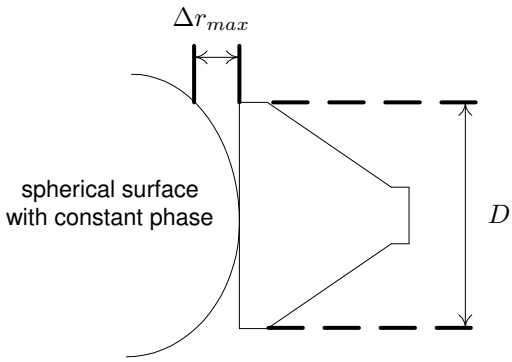

Figure 5.1: *Phase error criterion at a receive antenna with maximum cross section (D is the antenna dimension).*

the receive antenna. The phase of each ray is a function of the distance between the antennas, frequency and antenna dimensions. This effect causes variations in the received power as function of distance between the antennas and frequency and may cause distortion in the received signal. In the following, the near-field effect associated to the phase error is analyzed. Without loss of generality and for

simplicity of the analysis, a "thin" dipole antenna with full matching is assumed in the following.

Phase error for a dipole

Let's assume the situation of a thin dipole as depicted in Figure 5.2. The param-

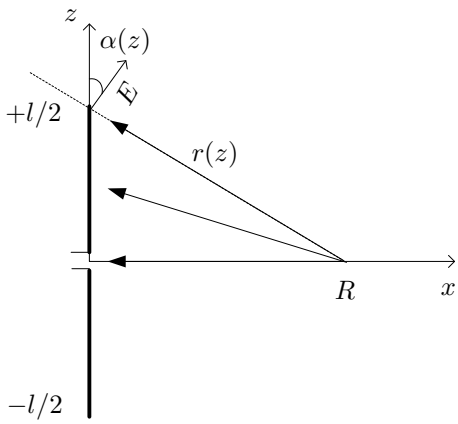

Figure 5.2: *Receive dipole.*

eter l is the length of the dipole, R is the position of a point source (infinitesimal dipole), $r(z)$ is the distance between the point source and every point of the dipole and α is the angle between the electric field E direction and the z-axis. The voltage V in the terminals of the dipole as a function of distance can be expressed as:

$$V \propto \int_{-l/2}^{+l/2} E_{rz}(z) I(z) dz \tag{5.1}$$

where $E_{rz}(z)$ is the z component of the electric field on the surface of the dipole and $I(z)$ is the current distribution on the surface of the dipole. For some constant c', equation (5.1) becomes:

$$\begin{aligned} V = c' \int_{-l/2}^{+l/2} I(z) \frac{e^{-jkr(z)}}{r(z)} \cos(\alpha(z)) dz = \\ c' e^{-jkR} \int_{-l/2}^{+l/2} I(z) \frac{e^{-jk(r(z)-R)}}{r(z)} \cos\left(\arctan\left(\frac{z}{R}\right)\right) dz \end{aligned} \tag{5.2}$$

where $k = 2\pi/\lambda_w$ is the wave number and z is the position along the dipole. The voltage can be expressed as:

$$V = c'' \int_{-l/2}^{+l/2} I(z) \frac{e^{-j\frac{2\pi}{\lambda_w}\left(\sqrt{R^2+z^2}-R\right)}}{\sqrt{R^2+z^2}} \cos\left(\arctan\left(\frac{z}{R}\right)\right) dz \tag{5.3}$$

where c'' is a constant different from c'. Assuming a uniform current distribution ($I(z)$ = constant), the received power for several distances as a function of frequency at the terminal of a 16 cm dipole is shown in Figure 5.3 [1]. The received power ($20\log_{10}(V)$) is normalized to distance assuming a power distance dependence of $1/R^2$. From this figure it can be observed that the received power at very short distances is less than expected for the far-field region of the antenna. The main reason is that different rays picked up by the antenna are not in-phase, and therefore the total received power is less. Another reason is that when a source point is very close to the dipole at distance R, the rays of the received spherical wave have traveled outside the terminal points a distance larger than R.

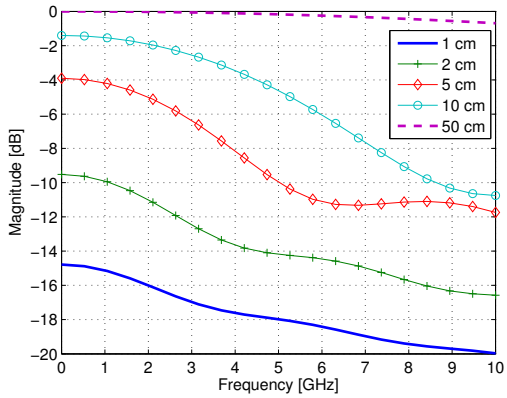

Figure 5.3: *Normalized received power vs. frequency for several distances R, for a 16 cm dipole with a uniform current distribution.*

Assuming now a sinusoidal current distribution (the current in a center-fed wire antenna has a sinusoidal form with nulls at the end points [80]) and different dipole lengths, the received power for several distances as a function of the frequency is shown in Figure 5.4. In this case, the normalized power received at short distances is also smaller than for large distances at low frequencies. Moreover, the null points (in frequency) in the far-field, are not null in the near-field. This is because the radiation pattern in the near-field is different from the radiation pattern in the far-field. This effect is depicted in Figure 5.5 which shows two dipoles of $2\lambda_w$ lengths. The antenna to the left is situated in the far-field, so, in this case the received voltage V_{FF} using equation (5.3) will be zero. The second dipole (right) is placed in the near-field. The z/R terms now deviate from zero. Despite of the sinusoidal current distribution with zero at the terminals, the receive voltage V_{NF} using the same equation is not zero anymore.

[1] Please note that a hypothetical uniform current distribution and a 16 cm dipole have been assumed here only to emphasize the effect.

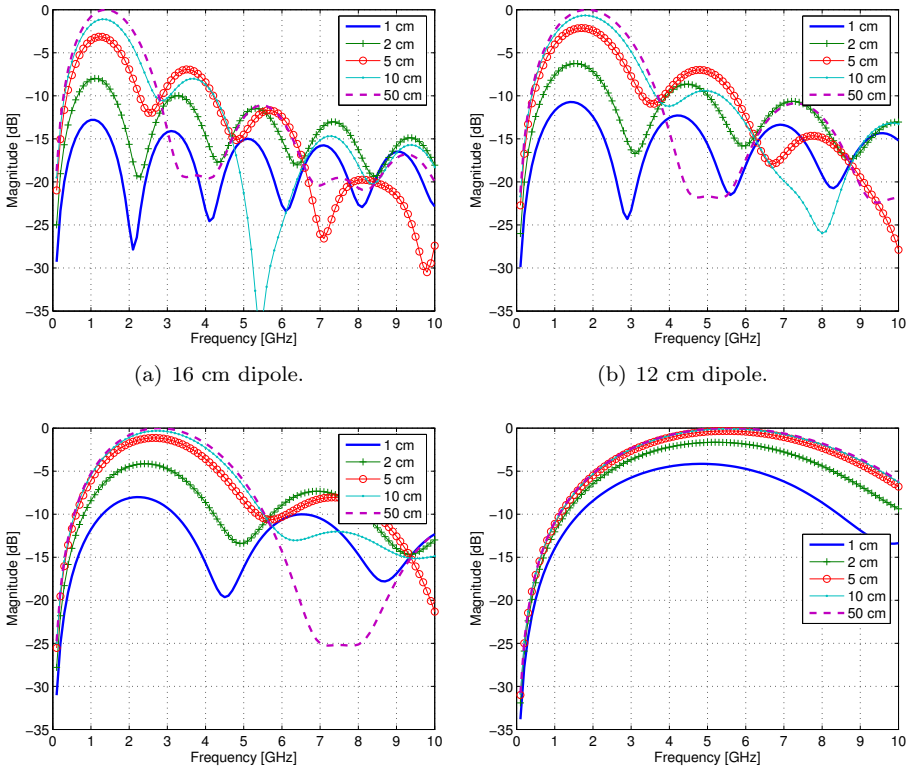

(a) 16 cm dipole.

(b) 12 cm dipole.

(c) 8 cm dipole.

(d) 4 cm dipole.

Figure 5.4: *Normalized magnitude (excluding the $1/R^2$ dependence) of the electric field vs. frequency for different distances perpendicular to the axis of the dipole.*

In the above formulas, the electric field radiated from an infinitesimal dipole is modeled as:

$$E_\theta \propto \frac{e^{-jkr}}{r}\hat{\theta}, \tag{5.4}$$

where $\hat{\theta}$ is a unitary vector in the θ direction, which is actually an approximation of the electric field for far-field regions. In the near-field this approximation is not valid anymore and the total electric field has to be considered using the equations for an infinitesimal dipole given by [80]:

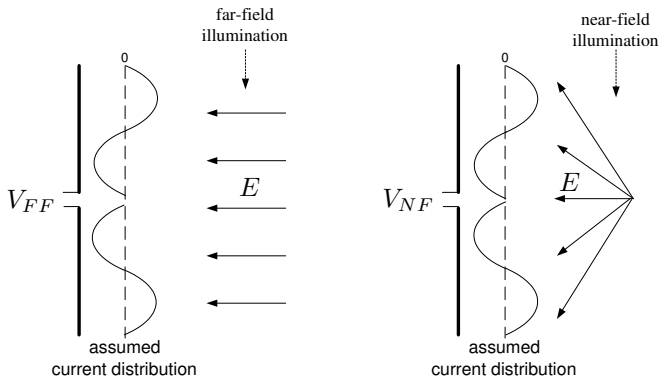

Figure 5.5: *Radiation pattern distortion.*

$$E_r = \eta \frac{I_0 l \cos\theta}{2\pi r^2}\left[1 + \frac{1}{jkr}\right] e^{-jkr}, \tag{5.5}$$

$$E_\theta = j\eta \frac{k I_0 l \sin\theta}{4\pi r}\left[1 + \frac{1}{jkr} - \frac{1}{(kr)^2}\right] e^{-jkr}, \tag{5.6}$$

$$H_\phi = j \frac{k I_0 l \sin\theta}{4\pi r}\left[1 + \frac{1}{jkr}\right] e^{-jkr}, \tag{5.7}$$

where I_0 is the excitation current, η is the free space impedance ($120\pi\,\Omega$), θ is the elevation angle with respect to the dipole axis assumed along the zenith, ϕ is the azimuth angle with respect to the x-axis in a rectangular coordinate system with its z-axis pointing to zenith and r is the distance from the dipole. Considering the situation depicted in Figure 5.6, the electric and magnetic fields at R in the z and y (entering into the paper) directions respectively, become:

$$E_{rz} = \left[\begin{array}{c} \int_{-l/2}^{+l/2} E_\theta(z)\cos(\alpha)dz + \\ \int_{-l/2}^{+l/2} E_r(z)\cos\left(\frac{\pi}{2}-\alpha\right)dz \end{array}\right]\hat{z} \tag{5.8}$$

$$H_{ry} = \left[\int_{-l/2}^{+l/2} H_\phi(z)dz\right]\hat{y} \tag{5.9}$$

Using the fields described in equations (5.5) to (5.7), the total electric and magnetic fields can be expressed as:

$$E_{rz} = \left[\begin{array}{c} \int_{-l/2}^{+l/2} j\eta \frac{kI(z)l\sin\theta}{4\pi r(z)}\left[1 + \frac{1}{jkr(z)} - \frac{1}{(kr(z))^2}\right]\cdot \\ e^{-jkr(z)}\cos(\alpha)dz + \\ \int_{-l/2}^{+l/2} \eta \frac{I(z)l\cos\theta}{2\pi r(z)^2}\left[1 + \frac{1}{jkr(z)}\right]\cdot \\ e^{-jkr(z)}\cos\left(\frac{\pi}{2}-\alpha\right)dz \end{array}\right]\hat{z} \tag{5.10}$$

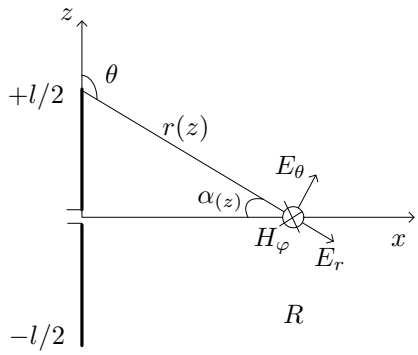

Figure 5.6: *Near-fields (Electric and magnetic) along the x-axis and generated by a dipole antenna of length l.*

$$H_{ry} = \left[\int_{-l/2}^{+l/2} j \frac{kI(z) l \sin\theta}{4\pi r(z)} \left[1 + \frac{1}{jkr(z)} \right] e^{-jkr(z)} dz \right] \hat{y} \tag{5.11}$$

Using the above equations, the electric field as a function of frequency for several points along the x axis are shown in Figure 5.7. The figure learns that the magnitude of the electric field decreases when the distance becomes smaller.

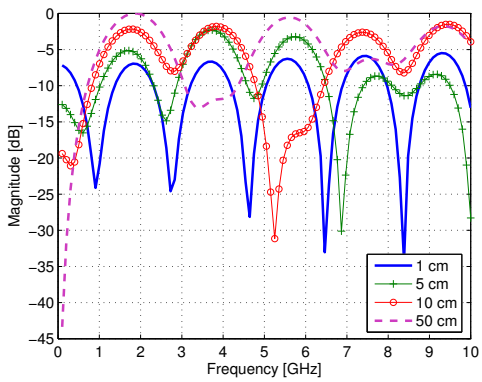

Figure 5.7: *Normalized magnitude of the electric field vs. frequency for different distances which are perpendicular to the axis of the dipole (normalized to received magnitude at 50 cm distance, excluding $1/R^2$ dependence.*

Phase error for two dipoles

In the previous paragraph, the phase error for one dipole has been evaluated, when the source is a point source. In this paragraph, the same effect will be in-

vestigated when transmit and receive antenna are dipoles. Assuming the situation depicted in Figure 5.8, the voltage V_{rx} at the terminals of the receive dipole can be expressed as [80]:

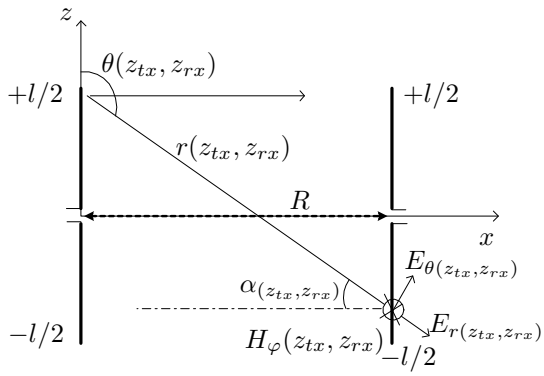

Figure 5.8: *Geometry of determining phase error effects between two dipoles.*

$$V_{rx} \propto \frac{1}{I_{rx_i}} \int_{-l/2}^{+l/2} E_{rz}(z_{rx}) I_{rx}(z_{rx}) dz_{rx} \tag{5.12}$$

where I_{rx_i} is the current at the feed point of the receive antenna, I_{rx} is the current induced in the receive dipole, z_{rx} is the position along the receive dipole and l is the length of the dipole. The electric field along the receive dipole is given by:

$$E_{rz}(z_{rx}) = \begin{bmatrix} \int_{-l/2}^{+l/2} E_{\theta}(z_{tx}, z_{rx}) \cos(\alpha(z_{tx}, z_{rx})) dz_{tx} + \\ \\ \int_{-l/2}^{+l/2} E_{r}(z_{tx}, z_{rx}) \cos\left(\frac{\pi}{2} - \alpha(z_{tx}, z_{rx})\right) dz_{tx} \end{bmatrix} \hat{z} \tag{5.13}$$

Substituting equation (5.13) into equation (5.12), the voltage in the receive antenna can be expressed as:

$$V_{rx} \propto \frac{1}{I_{rx_i}} \int_{-l/2}^{l/2} \begin{bmatrix} \int_{-l/2}^{l/2} \Big(j\eta \frac{kI(z_{tx}) l \sin\theta(z_{tx}, z_{rx})}{4\pi r(z_{tx}, z_{rx})} \\ \left[1 + \frac{1}{jkr(z_{tx}, z_{rx})} - \frac{1}{(kr(z_{tx}, z_{rx}))^2}\right] \\ e^{-jkr(z_{tx},z_{rx})} \cos(\alpha(z_{tx}, z_{rx})) \Big) dz_{tx} + \\ \int_{-l/2}^{l/2} \Big(\eta \frac{I(z_{tx}) l \cos\theta(z_{tx}, z_{rx})}{2\pi r(z_{tx}, z_{rx})^2} \\ \left[1 + \frac{1}{jkr(z_{tx}, z_{rx})}\right] \\ e^{-jkr(z_{tx},z_{rx})} \cos\left(\frac{\pi}{2} - \alpha(z_{tx}, z_{rx})\right) \Big) dz_{tx} \end{bmatrix} I_{rx}(z_{rx}) dz_{rx} \tag{5.14}$$

To verify expression (5.14), simulations were done using the IE3D Electromagnetic simulator. To this end, different dipoles associated to different frequencies (i.e. different lengths) have been simulated. Figure 5.9 compares the calculated and simulated (normalized) received power as a function of distance between two dipoles (the x-axis in the middle of the figures shows the distance normalized to the wavelength λ_w).

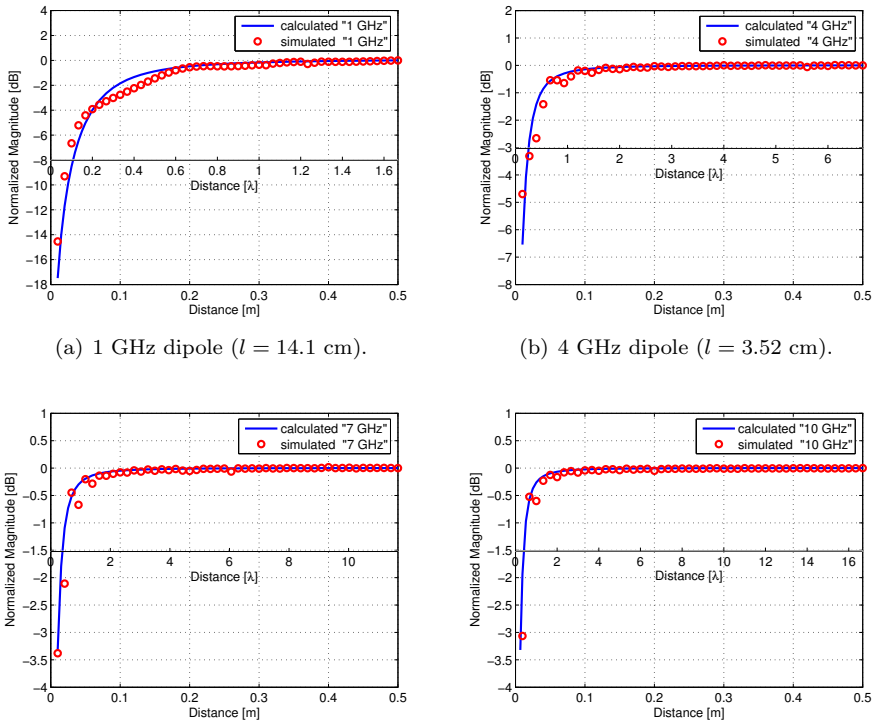

(a) 1 GHz dipole ($l = 14.1$ cm).

(b) 4 GHz dipole ($l = 3.52$ cm).

(c) 7 GHz dipole ($l = 2.01$ cm).

(d) 10 GHz dipole ($l = 1.41$ cm).

Figure 5.9: *Normalized (excluding $1/R^2$ dependence) received power as a function of the distance for different dipole lengths.*

From this figure it can also be observed that the received power at very short distances is less than expected for the far-field region of the antenna and the calculations match well to the simulations and they experience the same (exponential) behavior. Moreover, the loss is higher for larger antennas, which agrees with the phase error criterion. According to the obtained results, the received power experiences the same behavior with respect to frequency and hence the same behavior can be expected when the power is averaged over a large frequency band. Therefore, the simulation results of different dipoles at different center frequen-

cies are combined. Figure 5.10(a) shows the calculated and simulated normalized power, averaged over the frequency band 3-10 GHz (i.e. averaged over 8 dipoles operating in the band 3 to 10 GHz with a step of 1 GHz), as a function of the distance between two dipoles. Again the results match very well. However, a dipole antenna is known as a narrowband antenna. To validate whether this approach (i.e. combining different narrow-band dipoles) is correct, additional simulations with wideband antennas have been done. To this end, a diamond antenna[2] has been simulated between 3 and 10 GHz and the results were compared to those of combined dipoles in Figure 5.10(b), as can be seen, an nearly identical behavior is observed.

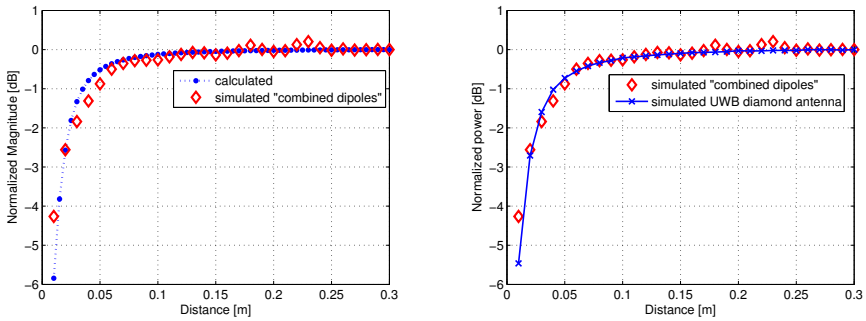

(a) combined dipoles.

(b) combined dipoles and UWB diamond antenna.

Figure 5.10: *Normalized (excluding $1/R^2$ dependence) received power, averaged over the frequency band 3 to 10 GHz, as a function of the distance.*

5.2.2 Antenna mismatch

The electric and magnetic fields for distances within the near-field region have a quite different behavior. They consist of radiating components and reactive components. For the radiating field components, the source is not affected by the observer. Once the radiating field leaves the antenna, the source is not affected if the energy is absorbed or not. For reactive or stored fields the effect is different. Any time that an observer extracts or diverts a part of the reactive field energy, it will cause a reaction in the source circuit which might change the input impedance of the antenna [81]. Figure 5.11 shows the different field components in equation (5.6) as a function of distance. In this figure, it can be seen which field predominates in the near- and far-field. All terms have the same value at $\lambda_w/2\pi$. For distances below $r = \lambda_w/2\pi$ (point of intersection) the reactive fields

[2] A diamond antenna is a planar antenna formed by two isosceles triangles. The width and height of the triangles is about $\lambda_w/4$ of the center frequency.

predominate. The coupling of the reactive static field to the receive antenna can be modeled as an electric and/or magnetic coupling and it will affect the transmit antenna by changing its input impedance. This coupling will vary with frequency. The changes in the input impedance of the transmit antenna may cause a mismatch for one or several frequencies, and a distortion in the frequency response of the antennas. To analyze this effect, simulations have been done using two identical diamond antennas placed at different distances. Figure 5.12 shows the antenna reflection coefficient S_{11} as a function of frequency for different separation distances. Different frequency bands have been simulated with correspondingly different "diamond" antenna sizes (i.e. 2x2 cm and 4x4 cm for one flair). From these figures it can be seen that for distances of 2 cm and larger the variations in S_{11} are not very big because the antenna is still matched. For distances of 1 cm (or less) a small antenna mismatch occurs.

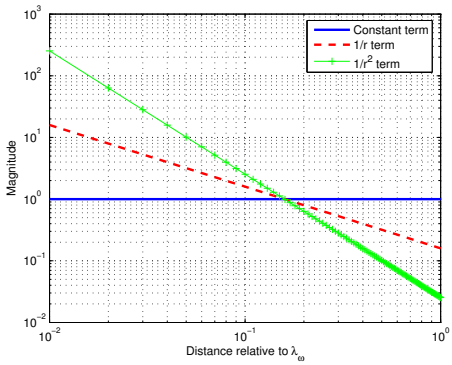

Figure 5.11: *Different field components generated by an infinitesimal dipole.*

5.2.3 Reradiation between antennas

The voltage induced in a receive antenna due to the electromagnetic field generated by a transmit antenna produces a current along the antenna and into the load impedance. Part of the power picked up by the antenna will be absorbed by the load impedance. Effects from the induced currents are different. These currents may produce reradiation from the receive antenna that can be picked up by the transmit antenna; these currents in the transmit antenna can reradiate again and may produce interference in the receive antenna. The amount of power reradiated by the receive antenna depends on the antenna mismatch and the physical antenna structure. For a given distance, the reradiation between the antennas may add constructively or destructively depending on the frequency and the phase shift introduced by both antennas. This effect causes a variation in the

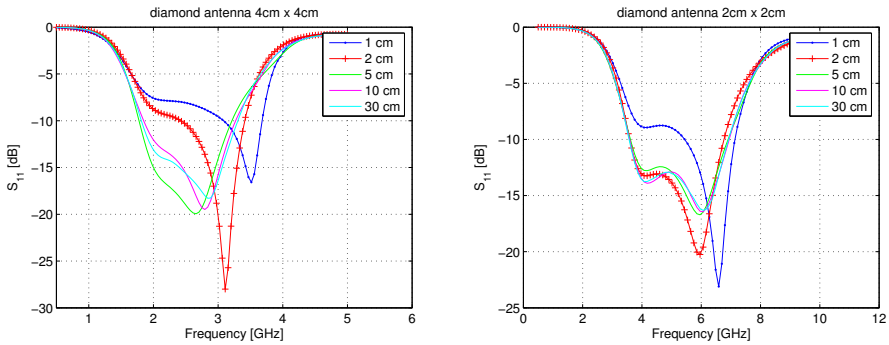

Figure 5.12: *Variations in the reflection coefficient as a function of frequency for different distances between antennas.*

received power as a function of frequency. It means that the frequency response may change for different distances, not only in level, but also the pulse shape. Simulation results (as given in previous paragraphs) have been used to investigate the received pulse waveform for different distances between two diamond antennas. Figures 5.13(a), 5.13(b) and 5.13(c) show the received pulse waveform for diamond antennas with sizes of 2 cm, 3 cm and 4 cm , respectively.

From these figures, the received pulse waveform at 2 cm and 3 cm distance is almost the same and hence the reradiation between the antennas is negligible. Clearly, for a smaller antenna the effect is smaller, due to the dependence on the surface of the antenna and the structural mode of the scattering cross section. Therefore, to highlight this effect, an additional simulation of a larger 6 cm diamond antenna was done. The corresponding results are shown in Figure 5.13(d). In this figure, two vertical dashed lines are indicated. These lines correspond to the delay times $\tau_1 = 0.125$ ns and $\tau_2 = 0.185$ ns when the antennas are separated by 2 cm and 3 cm, respectively. The spatial distance difference can be determined as: $\widehat{\Delta d} = (\tau_2 - \tau 1) \cdot c = 1.8$ cm. This value is nearly the distance of 2 cm that the wave needed to travel from receive antenna to transmit antenna and coming back $\Delta d = 2(d_2 - d_1) = 2(3 - 2) = 2$ cm. This means that some reradiation between transmit and receive antennas occurred.

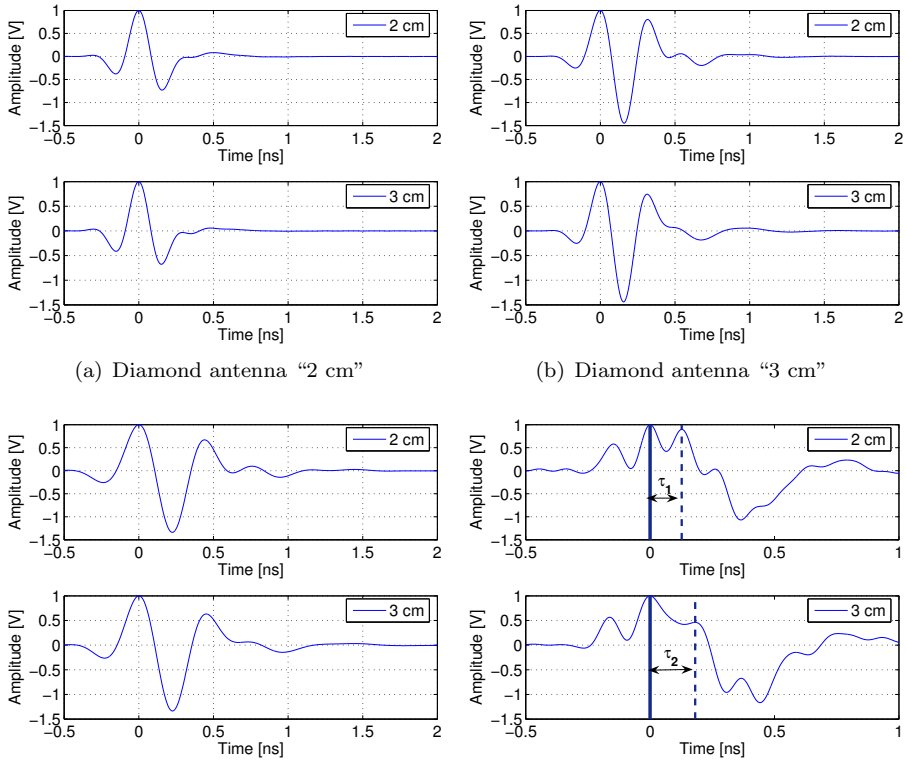

(a) Diamond antenna "2 cm"

(b) Diamond antenna "3 cm"

(c) Diamond antenna "4 cm"

(d) Diamond antenna "6 cm"

Figure 5.13: *Received pulse waveform at 2 and 3 cm distance for different diamond antennas.*

5.3 Proposed link budget model

Different effects such as antenna mismatch, reradiation between antennas and phase error can appear when transmit and receive antennas are close to each other. According to the previous section, the link budget in the near-field will be primarily affected by the phase error which is dependent on the considered bandwidth. When the received power is integrated over the large UWB bandwidth, it tends to be smaller than the expected received power using Friis law for far-field conditions, as can be seen in Figure 5.10. The Friis equation is given by:

$$P_r(f) = P_t(f)G_t(f)G_r(f)\left(\frac{\lambda_w}{4\pi r}\right)^2 \tag{5.15}$$

where $\lambda_w = c/f$ and P_t, P_r, G_t and G_r are the transmit and receive powers, and transmit and receive antenna gains, respectively. The phase error becomes important when the physical dimensions of the antennas are large compared to the distance between the antennas, i.e. for distances $r < 2D^2/\lambda_w = r_{ff}$ [80] where D is the largest dimension of the antenna and r_{ff} is the far-field limit distance. The operating frequency also plays an important role because at higher frequencies the phase errors will be larger for the same antenna dimensions; the behavior will therefore vary for different frequencies, which implies that it can result in signal distortion. Thus, these parameters should be taken into account in the channel model under near-field conditions. Modeling of near-field effects based on (5.14) is complicated. We here propose a simplified model for the link budget in the near-field. This novel model introduces an extra loss factor to the known far-field free space equation, caused by near-field effects. In this model, the total loss is expressed as:

$$L_{total}(r,f) = \frac{P_t(f)}{P_r(f)} = L_{ff}(r,f)\gamma_{nf}(r,f) \tag{5.16}$$

where

$$\gamma_{nf}(r,f) = 1 - e^{-\frac{r}{\delta_D(f,A_s,\theta)}} \tag{5.17}$$

L_{total} is the total loss of the channel, L_{ff} is the channel loss under far-field conditions, γ_{nf} is the correction factor due to near-field effects and δ_D is the distance decay constant which depends on the maximum antenna size A_s, its orientation θ and the frequency f. According to equation (5.17), the near-field correction factor $\gamma_{nf} \approx 1$ for far-field $r \gg \delta_D$. The proposed model is validated with measurements for different kinds of antennas.

5.4 Measurements, simulations and verification

5.4.1 Measurement set-up and description

In order to validate the proposed model, a set of measurements has been performed at different distances using the time-domain technique as shown in Figure 5.14(a) [82]. The generator fires a Gaussian-like pulse with a time duration of 35 ps. The sampling oscilloscope controls the sampling unit and the pulse generator, with trigger pulses each 100 ns, has an operational bandwidth up to 26 GHz. An acquisition time window of 10 ns is used with 4096 points which means that the received signal is sampled at a rate of 1 sample per 2.5 ps. The antennas are situated on Styrofoam boards in order to keep them more than one meter from the ground. Also there were no objects within 1 m around the antennas. In this way, the reflections of the walls and/or objects can be removed using the appropriate time window. In addition to time-domain measurements, a set of measurements based on the frequency-domain technique has been performed in an an-echoic chamber (see Figure 5.14(b)). To this end, a network analyzer

"Agilent-E8364B" is used and a bandwidth of 12 GHz is measured from 0.01 to 12.01 GHz with a step size of 7.5 MHz. For both set-ups, two identical transmit and receive antennas were used. One antenna was kept fixed while the other one was moved on a straight line covering a distance from 0.5 cm to 1 m. In total six pairs (6x2) of different antennas were used: three pairs are bi-conical antennas, one pair consists of planar elliptical UWB Time Domain "Schantz" antennas, one pair consists of planar UWB butterfly antennas (2-9 GHz) and the last pair consists of dielectric wedge antennas (0.5-6 GHz). The bi-conical antennas together with UWB Schantz antennas are described in Chapter 3. The butterfly and dielectric wedge antennas are shown in Figure 5.15 and more details can be found in [83] and [84], respectively. In total, about 1400 measured profiles have been gathered.

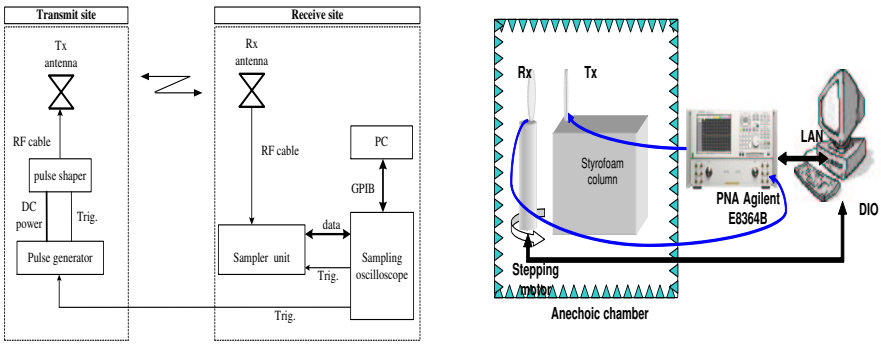

(a) Time domain set-up (b) Frequency domain set-up

Figure 5.14: *The set-up's used for the measurements.*

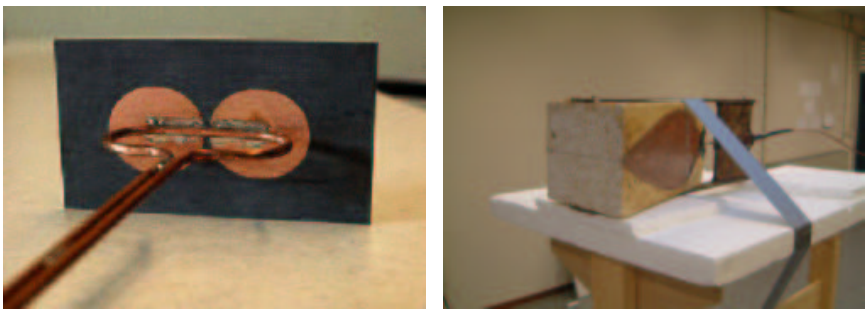

(a) Butterfly antenna [83] (b) Dielectric Wedge antenna [84]

Figure 5.15: *Different antennas used for the measurements.*

5.4.2 Data processing method

First the received time-domain signal is filtered over the entire antenna bandwidth using a digital butterworth filter in order to suppress the out-of-band noise. Then, a raised-cosine window is implemented to remove undesired signals and also to reduce the leakage problem when transforming the signal to the frequency-domain. The received signal is normalized to the free space equation as follows. The measured voltage in the far-field can be expressed using the Friis equation as:

$$V_r^{ff}(f) = V_g(f)\sqrt{G_t(f)G_r(f)G_{sys}(f)}\left(\frac{\lambda_w}{4\pi r_{ff}}\right) \tag{5.18}$$

where $V_g(f)$ is the generator output, $G_t(f)$ and $G_r(f)$ are transmit and receive antenna gains, respectively, r_{ff} is the far-field distance and $G_{sys}(f)$ is the transfer function of the measurement system which includes the cables, attenuators, etc. The measured voltage in the near-field can be expressed now as:

$$V_r^{nf}(f) = \left[V_g(f)\sqrt{G_t(f)G_r(f)G_{sys}(f)}\left(\frac{\lambda_w}{4\pi r_{nf}}\right)\right]\gamma_{nf}(r,f) \tag{5.19}$$

where r_{nf} is the near-field distance. Using (5.18) and (5.19), we get:

$$\gamma_{nf}(r,f) = \left[\frac{r_{nf}}{r_{ff}}\frac{1}{V_r^{ff}(f)}\right]V_r^{nf}(f) \tag{5.20}$$

From this equation it can be seen that the modeling results do not depend on the signal used to excite the channel which makes the model easy for use in practice.

5.4.3 Measurement and modeling results

The total normalized received power is integrated over the entire antenna bandwidth (e.g. 3-10 GHz) in order to obtain the received power as a function of distance between the antennas. From the measurements, the distance decay constant δ_D is estimated using the least squares method and the results of the model are plotted and compared to the measured results. Figure 5.16 shows the measurement results of the normalized received power as a function of distance for different antennas. For the bi-conical antennas the measured distance is determined as the distance between the edges of transmit and receive antennas. We consider the edge of the antenna as reference point because that is the point where most of the energy is radiated. As the magnitude of the received power is normalized to the far-field, the loss due to near-field effects can be seen as the difference between the curves and the horizontal 0 dB line. From this figure it is observed that for all used antennas the extra loss due to near-field conditions decreases with separation distance until r_{ff}, and it has an exponential behavior. The measurements and the proposed model match well for all antennas. Additionally, to check the validity of the model, the time-domain results are compared

to those obtained with the frequency-domain technique as shown in Figure 5.17. It is clear that the modeling results are the same for both techniques.

Moreover, the measured signal experiences all near-field effects discussed in section 5.2. In the following we try to check the impact of those effects by means of measurements rather than by simulations. Figure 5.18 shows the measured results of the reflection coefficient for the bi-conical "BC1" antenna and the Time Domain antenna. It can be seen that for the BC1 antenna the S_{11} parameter does not change with distance. The same effect is observed for the Time Domain antenna. Only a very small variation is seen at a distance of 1.5 cm, however, the S_{11} is still below -10 dB which means that the antenna is sufficiently matched. To investigate multiple antenna reflections, the measured signals at different "small" distances are compared in Figure 5.19. From this figure it is clear that multiple antenna reflections do not occur for such antennas.

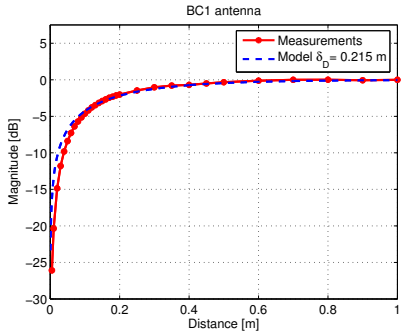

(a) Bi-conical antenna BC1

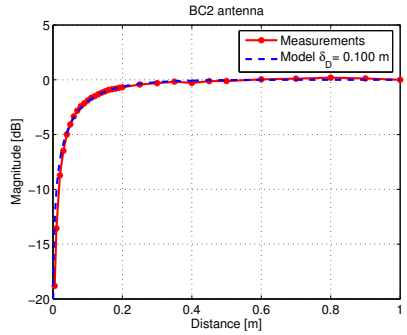

(b) Bi-conical antenna BC2

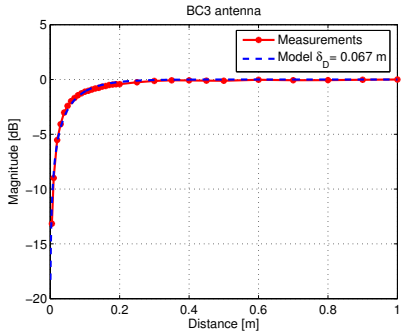

(c) Bi-conical antenna BC3

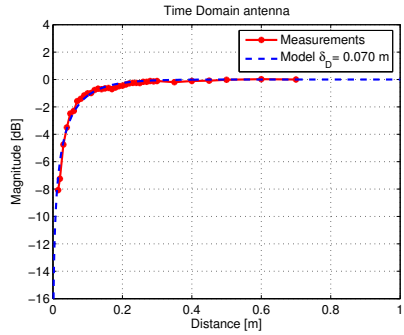

(d) Time Domain antenna

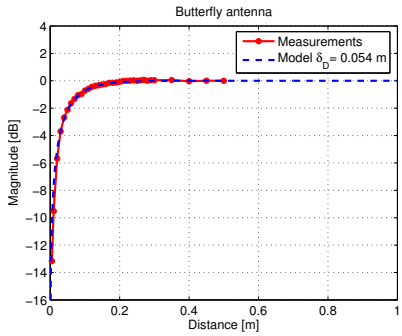

(e) Butterfly antenna

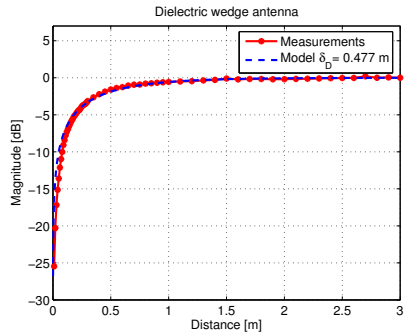

(f) Dielectric wedge antenna

Figure 5.16: *Normalized channel loss as a function of distance for different types of antennas. Comparison between measurements and model with appropriate distance decay constant* δ_D

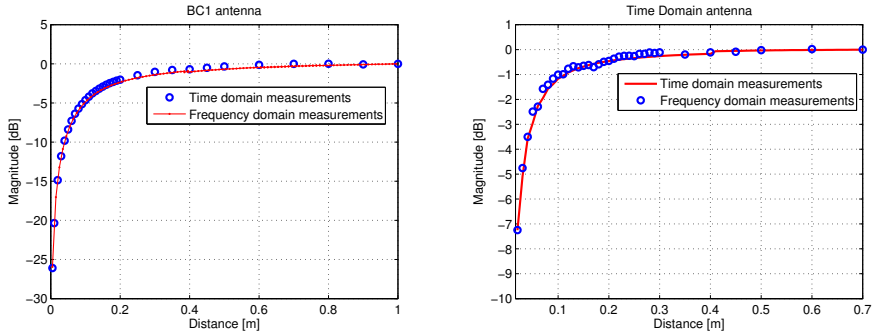

(a) Bi-conical antenna BC1 (b) Time Domain antenna

Figure 5.17: *Comparison of the measurement results using time- and frequency-domain measurement techniques.*

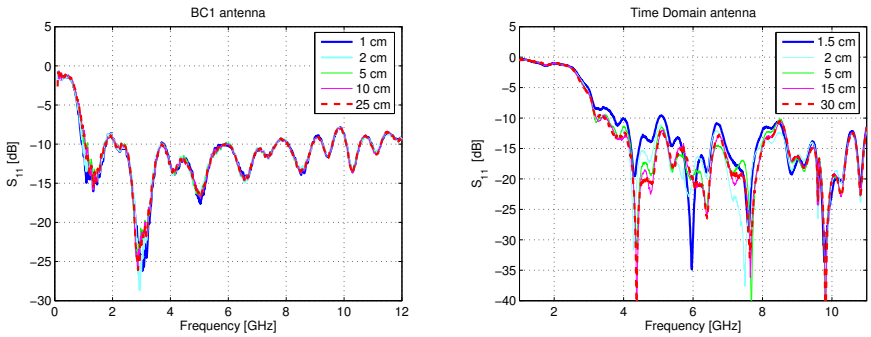

(a) Bi-conical antenna BC1 (b) Time Domain antenna

Figure 5.18: *The measured reflection coefficient as a function of frequency for different separation distances between two identical antennas.*

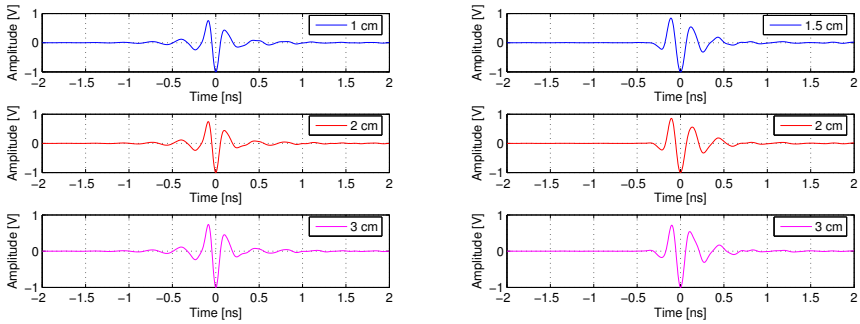

(a) Bi-conical antenna BC1

(b) Time Domain antenna

Figure 5.19: *The measured pulse waveform at different separation distances.*

5.4.4 Model parameters

Antenna size

According to the results in Figure 5.16, it can be concluded that for a fixed distance the losses are larger (higher δ_D) for larger antennas and this agrees with the phase error analysis. The distance for which the extra loss is 3 dB is about 15 cm, 7.1 cm and 4 cm for the BC1, BC2 and BC3 antennas, respectively. These values are comparable with the maximum size A_s of each antenna, that is 17.3 cm, 8.2 cm and 3.5 cm, respectively. Figure 5.20(a) shows the distance decay constant δ_D as a function of the maximum size for the bi-conical antennas BC1, BC2 and BC3. Although limited data was available, it can generally be observed that the behavior of δ_D tends to increase with the maximum antenna size A_s. The same behavior is observed for the simulated diamond antennas. Figure 5.20(b) shows the parameter δ_D versus A_s for all used antennas. The solid line represents a best fit model for the variation of δ_D with A_s. Using this model and the size of any other selected antenna, a-priori information about the parameter δ_D can be given.

Frequency dependency

As stated before, the coupling between antennas as well as the phase error will vary with the operational frequency. Therefore, it is important to check the frequency dependency of the proposed model. To this end, the large bandwidth is divided into small frequency bands (i.e. chunks), and the model parameter δ_D is estimated for each chunk (e.g. 100 MHz). Figure 5.21 gives the measurement and simulation results of δ_D as a function of frequency which show that δ_D increases slightly with frequency and the slope is almost the same for all cases. Based on

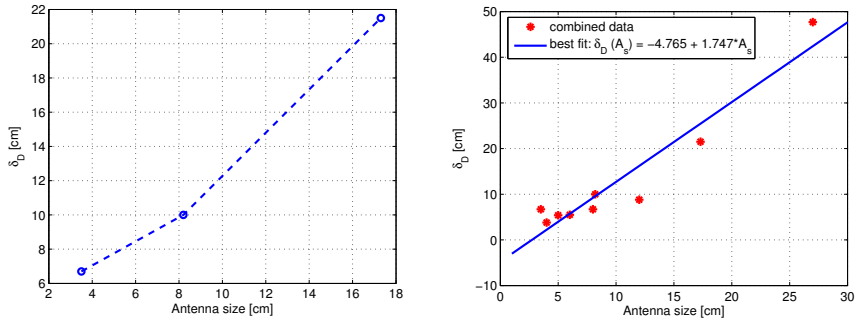

(a) Bi-conical antennas (b) Combined data of all antennas

Figure 5.20: *Distance decay constant δ_D vs. maximum antenna size A_s.*

these results, the parameter δ_D can be modeled as:

$$\delta_D(f) = a + bf \tag{5.21}$$

where the constant a depends on the size of the antenna and the slope b depends on the geometry of the antenna.

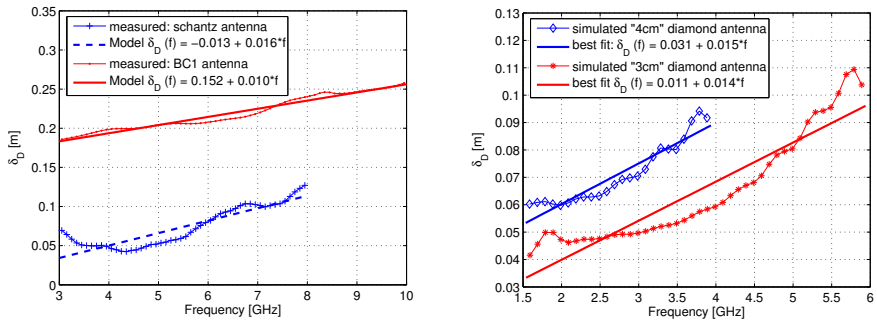

(a) Measured Bi-conical and Time domain antennas (b) Simulated diamond antennas

Figure 5.21: *Distance decay constant as a function of frequency.*

The effect of dispersion in antennas

One of the major problems in UWB transmission is the narrow-band interference (i.e. from WLAN). To suppress such interference different solutions have been proposed. One classical solution is the use of a notch filter which can be integrated

as part of the antenna. When an antenna has a notch it will become time-dispersive. The proposed model is checked for such kind of dispersive antennas by means of simulations using a diamond antenna of almost 2 cm with a notch at 5.4 GHz[3]. The reflection coefficient S_{11} and the gain S_{21} of the antenna are shown in Figure 5.22. Figure 5.23(a) gives the simulation results of the normalized power as a function of distance for the antenna with and without notch. The obtained results are almost the same and this is because the power is integrated over a large bandwidth and hence the notch hardly has an effect. However, we expect that when the power is integrated over a smaller bandwidth, the notch will dramatically influence our model parameter. To check this, we evaluate the frequency dependency of δ_D. Figure 5.23(b) gives the simulation results of δ_D as a function of frequency for the antenna with and without a notch. From this figure it is clear that the deviation of δ_D from the model is large around the notch. Exactly at the notch-frequency, δ_D is equal to zero because the received power for all distances converge to that notch point and hence the difference between the received power is zero which means no difference between near and far-field. It should also be noted that at higher frequencies there is a deviation of δ_D between the two antenna cases and this is because both antennas do not have exactly the same size.

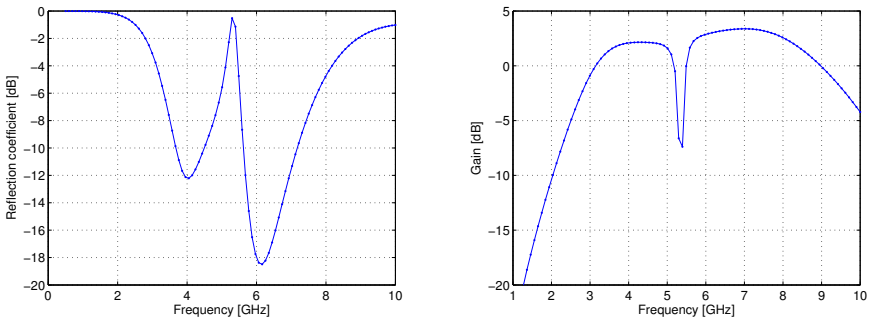

(a) Reflection coefficient. (b) Gain.

Figure 5.22: *Frequency characteristics of the UWB notch antenna.*

[3]Please note that the objective and emphasis of this part is applying the proposed model to a dispersive antenna rather than notch antenna design.

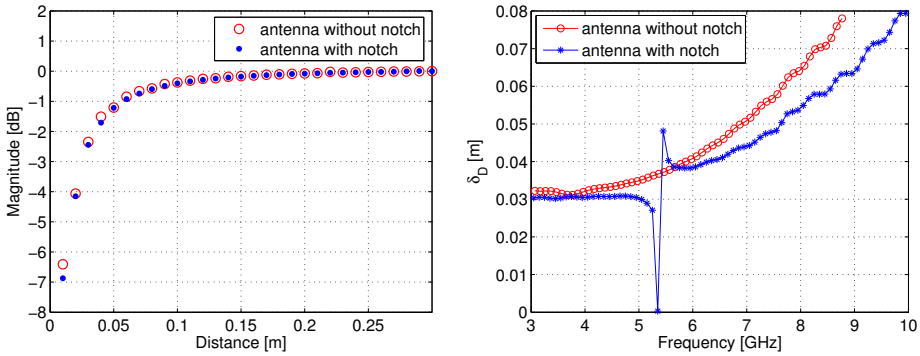

(a) Received power, integrated over the full bandwidth, as a function of distance.

(b) δ_D as a function of frequency.

Figure 5.23: *Comparison of diamond antenna with and without notch.*

Antenna orientation

For near-field applications the radiation pattern of an antenna is not complectly formed. Parameters as gain, directivity, etc. have no meaning in this region because they are specifically defined assuming far-field conditions. However, since the phase error and the coupling depend on the position of the antenna the model is checked for different antenna orientations. For this reason, a set of measurements is performed keeping one antenna fixed while changing the orientation of the other antenna from -90 to +90 degrees in steps of 5 degrees. This is repeated for all distances between transmit and receive antenna using the Time Domain antennas. Figure 5.24 shows the position of the antennas for different orientation angles. Figure 5.25 gives the measurement results of the normalized received power as a function of distance for different orientation angles for both time-domain and frequency-domain set-ups. From this figure we can see that the proposed model is still valid for all orientation angles. Moreover, the loss at 0 degree is maximum. This can be explained by the fact that when the antenna is oriented at a certain angle (for example 90 degrees) half of its aperture is situated more in the near-field region (with a lower received power) than the other half. Here its received power is higher and consequently the total received power is higher. A best fit model of the model parameter δ_D as a function of θ is given in [85].

(a) 0 degree (b) 45 degrees (c) 90 degrees

Figure 5.24: *Illustration of different orientation angles.*

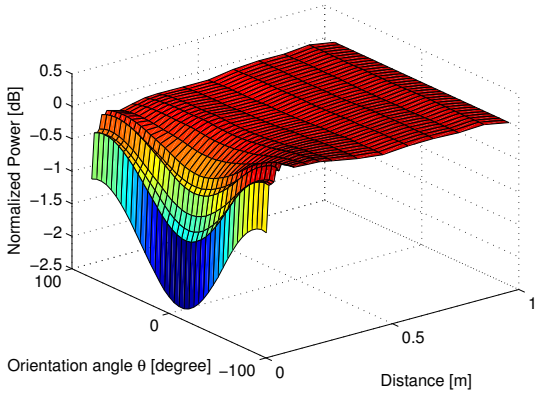

(a) Frequency-domain measurements.

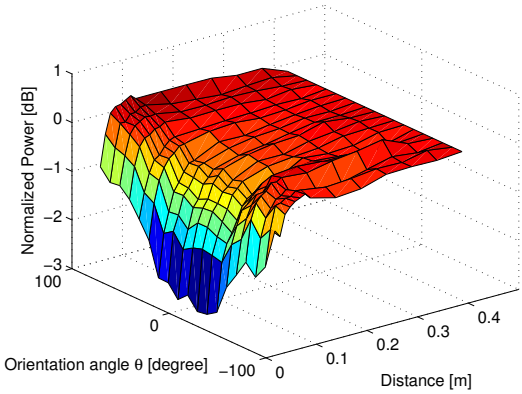

(b) Time-domain measurements.

Figure 5.25: *Normalized received power vs. distance for different orientation angles.*

5.5 Conclusions

In this chapter, a new UWB link budget model for short-range applications under near-field antenna conditions is proposed and validated by means of simulations and measurements. The model introduces a near-field modification factor for the losses as predicted under far-field conditions. The proposed model takes into account all main effects in the near-field (i.e. phase error, antenna mismatch and reradiation between antennas) and the model includes frequency, antenna size and orientation dependencies. A set of time- and frequency-domain UWB measurements covering the frequency band from 3.1-10.6 GHz was conducted using different antenna types. The model shows a good agreement with measurements and simulations and does not depend on the signal used to excite the channel which makes it easy to be used in practice. The obtained results show that the received signal for small antennas is mainly influenced by the phase error. However, for large antennas operating at low frequencies antenna mismatch and reradiation between antennas may become important as well. The near-field effect shows a strong dependency on the physical size of the antenna; it is stronger for larger antennas than for smaller antennas. The distance decay constant slightly increases with frequency and is linearly modeled.

Chapter 6

UWB Channel Estimation Based on Partially Measured Frequency Responses

6.1 Introduction

It is important to have a good understanding of the propagation channel and its characteristics in order to properly design a UWB system. Up to now, measurement campaigns and channel modeling efforts have been carried out to characterize the UWB channel. From the point of view of the measurements, a statistical analysis have been done based on the collected results, and statistical models have been proposed for the channel parameters.

Although its ultra wide bandwidth is making UWB technology very suitable for many applications, it is also requiring the development of new methods to characterize it. On the one hand, the measurement set-up for sounding the UWB band can become complex, and new parameters must be taken into consideration. On the other hand, the radio channel at small bandwidths has already been well modeled and validated by extensive measurement campaigns [7, 21, 86, 87]. This means that it is completely known how the radio channel in multiple (narrow) bands is affecting the signals. Therefore, it might be relevant to profit from available knowledge on multi-band channels in order to characterize the UWB channel.

This chapter deals with the characterization of the UWB channel based on measured chunks. The idea underlying the approach is to divide the UWB frequency band into sub-bands in the frequency-domain, where the channel in each of these sub-bands is completely known. Then, we want to combine the channel

models of each sub-band to get an UWB channel model.

In practice, it can happen that one or several sub-bands has not been measured [87]. This may put some constraints in the reconstruction of the whole UWB-CIR. In this respect, a step further is taken in this chapter to estimate the missing information of those unavailable (not measured) sub-bands by introducing a statistical frequency correlation model. This model incorporates the statistical correlation properties between all sub-band CIRs to predict the information for each missing sub-band.

This chapter is organized as follows. In section 6.2, we describe the modeling approach pointing out some advantages of employing this approach. Then, we analytically integrate the sub-band CIRs to get the UWB-CIR assuming a flat and multipath channel. Section 6.3 proposes the frequency correlation channel model to estimate the whole UWB-CIR when only partial frequency responses are known. The results are verified by using the measured data described in chapter 4. In section 6.4 important parameters of the model are discussed and evaluated with respect to the obtained estimation accuracy. In section 6.5, the proposed model is applied to obtain channel parameters like path-loss and time dispersion. Finally, in section 6.6 conclusions are provided.

6.2 A new approach for UWB channel modeling

6.2.1 Description

The novel approach discussed here is based on dividing the UWB band into sub-bands, in which the channel is already measured. Therefore, the proposed way of modeling the UWB channel can be considered by the following steps:

- dividing the UWB signal into sub-band signals,
- for each sub-band signal, a channel model is determined. This is done using known channel modeling methods,
- integration of all outputs of the channel to create the sub-band input signals,
- based on the input UWB signal and the obtained output signal after integration of the sub-band models, a proper model of the UWB channel can be provided.

This approach is illustrated in Figure 6.1. The parameters: f, λ_w, $B_{w_{uwb}}$ and $B_{w_{nb}}$ refer to frequency, wavelength, bandwidth of the UWB signal and sub-band signal, respectively.

6.2.2 Advantages

This approach may have many advantages. Intuitively, a different behavior of the radio channel is expected when a signal with an ultra wide bandwidth is

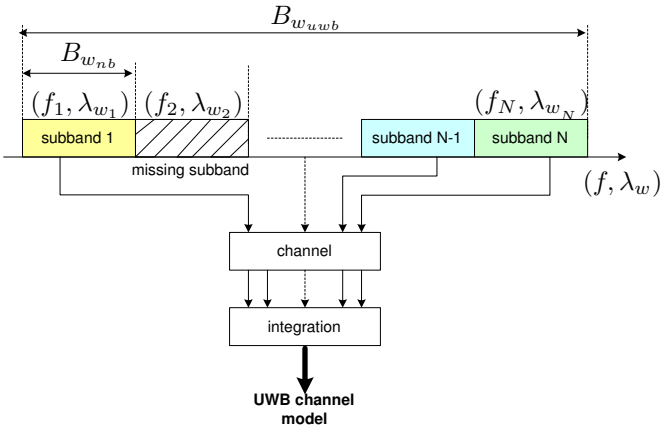

Figure 6.1: *Illustration of the modeling approach.*

transmitted. In existing sub-band channel modeling techniques (the bandwidth is relatively small) the separation between minimum and maximum frequencies is not very large. According to this, it is assumed that the channel characteristics, in terms of reflection, scattering and transmission parameters do not change over the considered frequency band. In other words, the wavelength changes slightly over the band and it can be assumed that the response of the elements in the environment is the same for the whole frequency band. However, when this frequency bandwidth increases substantially (as happens in UWB) the difference between maximum and the minimum frequencies increases and becomes not negligible. For the frequency band 3.1-10.6 GHz, the wavelength ratio becomes:

$$\frac{\lambda_{w_{max}}}{\lambda_{w_{min}}} = \frac{0.0968\,\mathrm{m}}{0.0283\,\mathrm{m}} \simeq 3.42 \tag{6.1}$$

Therefore, the response of elements in the environment in terms of propagation can no longer be considered constant over the whole bandwidth. The introduced approach might provide a physical insight into this frequency dependency of the propagation channel.

Another related aspect is the frequency dependency of the antenna. As has been said in the previous chapters (3 and 4), radio signal propagation is usually affected by the characteristics of the antennas. For conventional narrow- and medium-band communication systems, the frequency domain effects of the antenna can be well separated from the channel because the bandwidth is small and hence the antenna frequency response can be assumed to be flat over the frequency band of interest. However, this is not the case for UWB and hence the gain function of the antenna becomes:

$$G_{ant}(f) = g(f, \theta(f), \phi(f)) \tag{6.2}$$

where $g(.)$ is a function, f the frequency, θ the azimuth angle and ϕ the elevation angle. Using this approach, the effect of the antenna can be separated from each sub-band channel.

As stated in the previous section, using this approach we may estimate the whole UWB frequency response when having only information about some portions of the UWB band. From measurement point of view, having partial information about the whole UWB band would mean that only a number of sub-bands would have been sounded by means of measurement campaigns. That leads to saving time and effort in carrying out measurements. However, the main challenge in estimating the UWB frequency response based on partial information of several chunks is associated with the accuracy that can be achieved.

One of the issues regarding UWB transmission systems is the narrow-band interference. Since UWB systems operate over extremely wide frequency bands, they have to coexist with other narrow-band systems which may operate with much higher power levels. This may completely jam the UWB signals. Therefore, the introduced approach can avoid this problem on the narrow-band interference by skipping (i.e. not measuring) the frequency band in which the narrow-band interferer is active. It means that only measurements over sub-bands outside the interference band have to be measured and of course, the missing information associated to this interference band can be estimated separately.

6.2.3 Analytical integration

At first, a flat channel in the frequency-domain is considered. Although this assumption is simple, its analysis will give us some understanding on what is happening in the integration procedure. Afterwards a more realistic channel, i.e. frequency selective, will be assumed.

Integration of a flat channel

Let's assume a flat frequency response of the UWB channel as depicted in Figure 6.2. The UWB channel frequency response (UWB-CFR) can be written as:

$$H_{UWB}(f) = \prod\left(\frac{f}{2B_w}\right) = \begin{cases} 1 & \text{if } |f| < B_w \\ 0 & \text{otherwise} \end{cases} \tag{6.3}$$

where B_w is the UWB bandwidth and $\prod(.)$ denotes a step function. Taking the inverse Fourier transform (IFT) of $H_{UWB}(f)$, the UWB channel impulse response (UWB-CIR) is given by:

$$h_{UWB}(t) = \int_{-B_w}^{+B_w} e^{j2\pi ft} df = 2B_w sinc(2\pi B_w t) \tag{6.4}$$

with $sinc(x) = sin(x)/x$.

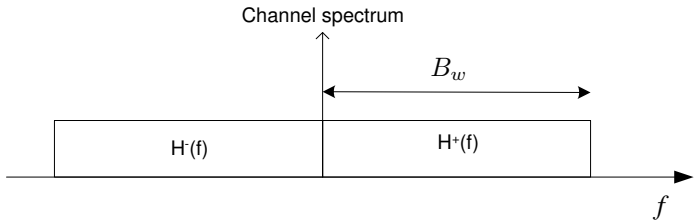

Figure 6.2: *Spectrum of the whole UWB band.*

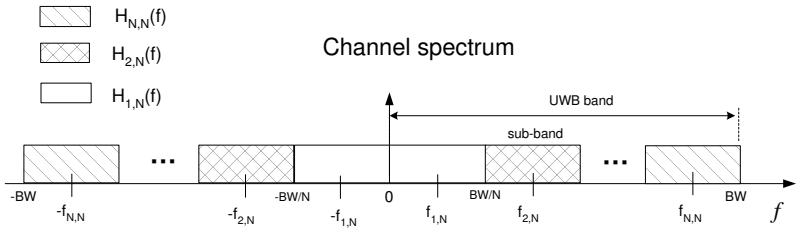

Figure 6.3: *Spectrum of the UWB band when divided into N sub-bands.*

Let's now divide the UWB bandwidth into N bands as depicted in Figure 6.3 where:

$$f_{ci,N} = \frac{B_w}{N}(2i-1), \qquad i \in [1, N] \tag{6.5}$$

refers to the center frequency of the the ith frequency chunk. The expression for the ith sub-band CFR of the positive and negative sides of the frequency axis can be expressed, respectively, as:

$$H^{+}_{i,N}(f) = \prod \left(\frac{f - f_{i,N}}{B_w/N} \right) \tag{6.6}$$

$$H^{-}_{i,N}(f) = \prod \left(\frac{f + f_{i,N}}{B_w/N} \right) \tag{6.7}$$

Using the IFT the CIR associated to the positive sub-band of the frequency axis equals:

$$\begin{aligned} h^{+}_{i,N}(t) &= \left(\int_{-\frac{B_w}{2N}}^{+\frac{B_w}{2N}} e^{-j2\pi f t} df \right) e^{j2\pi f_{i,N} t} \\ &= \frac{B_w}{N} sinc\left(\frac{\pi t B_w}{N} \right) e^{j2\pi f_{i,N} t} \end{aligned} \tag{6.8}$$

The same can be done for the negative side of the frequency axis:

$$h_{i,N}^{-}(t) = \frac{B_w}{N} sinc\left(\frac{\pi t B_w}{N}\right) e^{-j2\pi f_{i,N} t} \tag{6.9}$$

Using (6.8) and (6.9), the channel impulse response (CIR) of the ith sub-band is:

$$\begin{aligned} h_{i,N}(t) &= \text{IFT}\left\{H_{i,N}^{+}(f) + H_{i,N}^{-}(f)\right\} \\ &= \frac{2B_w}{N} sinc\left(\frac{\pi t B_w}{N}\right) \cos(2\pi f_{i,N} t) \end{aligned} \tag{6.10}$$

We now integrate the sub-bands (in terms of their frequency responses) to construct the resulting UWB channel. The integration is made as follows:

$$H_{UWB}(f) = \sum_{i=1}^{N} H_{i,N}(f) \tag{6.11}$$

Since all sub-band frequency responses have no overlapping frequencies, and making profit of the linearity property of the Fourier transform, we can take the IFT of both side of equation (6.11) and get:

$$\begin{aligned} h_{UWB}(t) &= IFT\left[H_{UWB}(f)\right] = IFT\left[\sum_{i=0}^{N} H_{i,N}(f)\right] \\ &= \sum_{i=1}^{N} IFT\left[H_{i,N}(f)\right] = \sum_{i=0}^{N} h_{i,N}(t) \end{aligned} \tag{6.12}$$

meaning that we can integrate also in time-domain. So, applying this result, including equation (6.10) in (6.12), we get:

$$h_{UWB}(t) = \frac{2}{\pi t} \sum_{i=1}^{N} \sin\left(\frac{\pi t B_w}{N}\right) \cos(2\pi f_{ci,N} t) \tag{6.13}$$

Using the trigonometric property: $\cos(x)\sin(y) = \frac{1}{2}\left[\sin(x+y) - \sin(x-y)\right]$, we get:

$$\begin{aligned} h_{UWB}(t) &= \frac{1}{\pi t}\left[\sin\left(2\pi t B_w/N\right) - \quad 0 \quad\right] + \\ &+ \frac{1}{\pi t}\left[\sin\left(4\pi t B_w/N\right) - \sin\left(2\pi t B_w/N\right)\right] \\ &+ \frac{1}{\pi t}\left[\sin\left(6\pi t B_w/N\right) - \sin\left(4\pi t B_w/N\right)\right] \\ &+ .... \\ &+ \frac{1}{\pi t}\left[\sin\left(2(N-1)\pi t B_w/N\right) - \sin\left(2(N-2)\pi t B_w/N\right)\right] \\ &+ \frac{1}{\pi t}\left[\sin\left(2\pi t B_w\right) - \sin\left(2(N-1)\pi t B_w/N\right)\right] \end{aligned} \tag{6.14}$$

Looking at the terms corresponding to each sub-CIR, we can see that the first term of the ith CIR is canceled with the second term of the (i+1)th CIR. Thus, in the end, only the first term of the Nth sub-CIR remains in the summation:

$$\begin{aligned} h_{UWB}(t) &= \frac{1}{\pi t}\sin(2\pi t B_w) \\ &= 2B_w sinc(2\pi B_w t) \end{aligned} \tag{6.15}$$

which is the same as (6.4) when the whole UWB band is assumed. It is also interesting to note that the reconstructed UWB channel does not depend on the number of sub-bands N.

Integration of a multipath channel

The UWB multipath channel is given by:

$$h_{UWB}(t) = \sum_{k=1}^{L} a_k \delta(t - \tau_k) \tag{6.16}$$

where a_k and τ_k are the amplitude and the delay of kth multipath component, respectively, and L is the number of multipath components. The frequency response corresponding to the UWB band would be:

$$H_{UWB}(f) = \sum_{k=1}^{L} a_k e^{-j2\pi f \tau_k} \tag{6.17}$$

Applying the windowing procedure (we note here that only a rectangular window is considered), we find for the frequency response of the ith sub-band:

$$H_{i,N}(f) = H_{UWB}(f)\left[\prod\left(\frac{f - f_{i,N}}{B_w/N}\right) + \prod\left(\frac{f + f_{i,N}}{B_w/N}\right)\right] \tag{6.18}$$

Taking the IFT of equation 6.18, the CIR of the ith sub-band becomes:

$$h_{i,N}(t) = h_{UWB}(t) * \underbrace{\text{IFT}\left\{\prod\left(\frac{f - f_{i,N}}{B_w/N}\right) + \prod\left(\frac{f + f_{i,N}}{B_w/N}\right)\right\}}_{A} \tag{6.19}$$

For the term A in (6.19) can be derived:

$$A = 2i\frac{B_w}{N} sinc\left(\frac{2i\pi t B_w}{N}\right) - 2(i-2)\frac{B_w}{N} sinc\left(\frac{2(i-1)\pi t B_w}{N}\right) \tag{6.20}$$

Using (6.19) and (6.20) gives:

$$\begin{aligned} h_{i,N}(t) &= \sum_{k=1}^{L} a_k \left[2i\frac{B_w}{N} sinc\left(2i\frac{B_w}{N}\pi(t - \tau_k)\right)\right] \\ &\quad - \left[2(i-1)\frac{B_w}{N} sinc\left(2(i-1)\frac{B_w}{N}\pi(t - \tau_k)\right)\right] \end{aligned} \tag{6.21}$$

Finally, integrating over all sub-CIRs results into the expression of the UWB-CIR:

$$h_{UWB}(t) = \sum_{k=1}^{L} a_k 2B_w sinc\left(2\pi B_w(t-\tau_k)\right) \tag{6.22}$$

We can see from eq. (6.22) that we get L components in terms of attenuated and delayed *sinc*'s according to the path amplitudes and delays, respectively.

6.3 UWB channel estimation methods

In the previous section, we have shown that the UWB channel can be well modeled by means of sub-band channel models (belonging to the same UWB band). It was assumed that all sub-band CIRs are known and their integration contributes into the total UWB-CIR. However, in this section we will discuss how the UWB-CIR can be estimated when not all sub-band CIRs are available.

6.3.1 Interpolation approach

One possibility regarding lack of information on some chunks can be considering them equal to zero, i.e., the frequency responses of those sub-bands are considered null. However, this approach may appear unrealistic. Hence, we can consider interpolation to estimate the sub-frequency responses in the missing chunks. For example, when information about chunks (i-1)th and (i+1)th is available, we assume that chunk ith can be estimated from them by interpolation. In the current approach, a linear interpolation between the previous and the next available chunks is performed for each missing chunk. Other interpolation like cubic one can also be used. The reason why a linear interpolation is selected in the model is because frequency responses of sub-bands are similar especially when they are close in frequency. So the closer the sub-bands, the more the interpolated UWB frequency response matches the original one.

6.3.2 Frequency correlation approach

The main idea behind the frequency correlation model is that (based on the knowledge of the channel at a basic frequency f_0, and incorporating statistically the correlations of the channel at frequency f_i with the channel at frequency f_0) the channel at another frequency (missing chunk) $f_i = f_0 + \Delta f_i$ can be predicted. It should be noted that the estimation of the missing sub-band channel can be performed in time-domain of frequency-domain. In this work, the estimation is done directly in frequency-domain and hence the estimated CIR can be obtained using the IFT.

Let's assume that $H(f_0)$ and $H(f_i)$ are the frequency response of the known and unknown sub-bands, respectively. Then the channel frequency response $\widehat{H}(f_i)$

of the missing chunks at f_i can be estimated as:

$$\widehat{H}(f_i) = w^* H(f_0) \tag{6.23}$$

where w is a desired filter which has to be designed and $(^*)$ denotes the conjugate Hermitian. For simple notation we denote $H(f_0)$ by H_0 and $H(f_i)$ by H_i. Our objective is now to minimize the error in the estimation of H_i. One way is to use the Linear Minimum Mean Square cost function $J(w)$ and we get:

$$\underset{w}{\operatorname{argmin}}\ J(w) = \underset{w}{\operatorname{argmin}}\ \ E\left\{|w^* H_0 - H_i|^2\right\} \tag{6.24}$$

where $E\{.\}$ denotes the expected value. Working out eq. (6.24) we get:

$$\begin{aligned} J(w) &= E\left\{|w^* H_0 - H_i|^2\right\} \\ &= E\left\{w^* H_0 H_0^* w - w^* H_0 H_i^* - H_i H_0^* w + |H_i|^2\right\} \\ &= w^* E\{H_0 H_0^*\} w - w^* E\{H_0 H_i^*\} - E\{H_i H_0^*\} w + E\{|H_i|^2\} \\ &= w^* R_c w - w^* r_c - r_c^* w + E\{|H_i|^2\} \end{aligned} \tag{6.25}$$

where R_c is the covariance matrix of the known chunks and r_c is the cross-covariance matrix between the known and unknown chunks. To minimize this function we have to compute its derivative with respect to w and set it to zero. It should be noted that when differentiating a complex function which depends on a parameter vector w with complex entries, there are two points which deserve extra attention. First we have to deal with the fact that w has complex entries and secondly w is a vector. The latter is not difficult to handle. The former (differentiating to a complex variables), however, is a bit different than differentiation of real functions. From literature we know [88, 89]:

$$\nabla(w^* r_c) = r_c,\ \ \nabla(r_c^* w) = 0,\ \ \nabla(w^* R_c w) = R_c w \tag{6.26}$$

Thus, by differentiating with respect to w and using eq. (6.26) we obtain:

$$\nabla J(w) \quad = \quad R_c w - r_c \tag{6.27}$$

The minimum of $\nabla J(w)$ is attained for:

$$\nabla J(w) = R_c w - r_c = 0 \quad \Rightarrow \quad w = R_c^{-1} r_c \tag{6.28}$$

This results is also known as characteristics for the Wiener filter. According to equation (6.28), if the matrix R_c and r_c are known, the missing chunks can be estimated. The estimation accuracy for the missing chunks will depend on the accuracy of R_c and r_c. As these matrices have to be statistically determined, enough measured data are required.

6.3.3 Measurements and comparison

To verify the proposed approach the time-domain measurement data described in the previous chapter are used. From this data, the matrix R_c and r_c are statistically computed and of course averaged over all measurements. Here we only focus on the indoor office environment. Without loss of generality, we assume 3 chunks H_1, H_2 and H_3 having the same bandwidth as depicted in Figure 6.4 and that the second chunk is not available. Hence our objective is to give an estimation of H_2. The vector H_0 consists of H_1 and H_3 as:

$$H_0 = \begin{bmatrix} H_1 \\ H_3 \end{bmatrix} \tag{6.29}$$

and H_i consists of H_2:

$$H_i = [H_2] \tag{6.30}$$

To quantify how accurate the missing chunk is estimated we define the following error:

$$\epsilon_H = \left| \frac{E_{H_2} - E_{\widehat{H}_2}}{E_{H_2}} \right| \tag{6.31}$$

where $\widehat{H}_2$ is the estimate of H_2 and

$$E_{H_2} = \int_{\frac{B_w}{3}}^{\frac{2B_w}{3}} |H_2(f)|^2 \, df \tag{6.32}$$

denotes the energy. For a total bandwidth of 600 MHz (i.e. the sub-band bandwidth is 200 MHz), the CDFs of the estimation error for the missing chunk H_2 are given in Figure 6.5 for the linear interpolation as well as the frequency correlation approach. From this figure it can be seen that the frequency correlation approach gives better estimation results than the linear interpolation. The linear interpolation uses only edge information (i.e. at the end of H_1 and the start of H_3), which do not provide any additional information on what is exactly happening in the missing band (i.e. the behavior of H_2). This is also the reason why no difference is obtained between LOS and NLOS cases when linear interpolation is

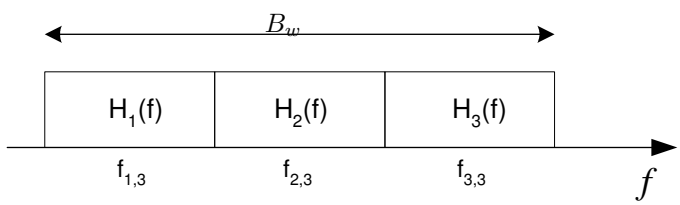

Figure 6.4: *Dividing the spectrum of $H(f)$ into three equal sub-bands.*

used. From the graphs it can also be observed that even for the case of the frequency correlation approach the mean estimation error is in the range of 20-40% which is high. This is because the bandwidth of the missing chunk is larger than the coherence bandwidth of the channel on which the channel remain constant (i.e. highly correlated). In other words, the correlation between the known and unknown chunks is low and hence the error is high. The coherence bandwidth is related the rms delay spread of the channel and is given as [90]:

$$B_{wc} = \frac{1}{2\pi\tau_{rms}} \tag{6.33}$$

According to the results presented in Chapter 4, the average τ_{rms} was found in the range of 8-13 ns for both LOS and NLOS indoor office environments. This means that the coherence bandwidth of the UWB channel is the range of 12-20 MHz. This knowledge justifies the higher estimation error obtained for NLOS when compared to LOS cases. To verify this we assume smaller bandwidths for the chunks. Figure 6.6 gives the estimation error when 100 MHz and 50 MHz bandwidth is assumed for each chunk. From this figure it can observed that the estimation remarkably depends on the width of the missing sub-band. An important question can be raised here: as the mean coherence bandwidth of the channel is about 20 MHz why such small error (e.g. 0.05%) is obtained when 50 MHz bandwidths are considered. This can be explained by the fact that the correlation is incorporated from both sides of the missing chunk as can be clearly seen in Figure 6.7.

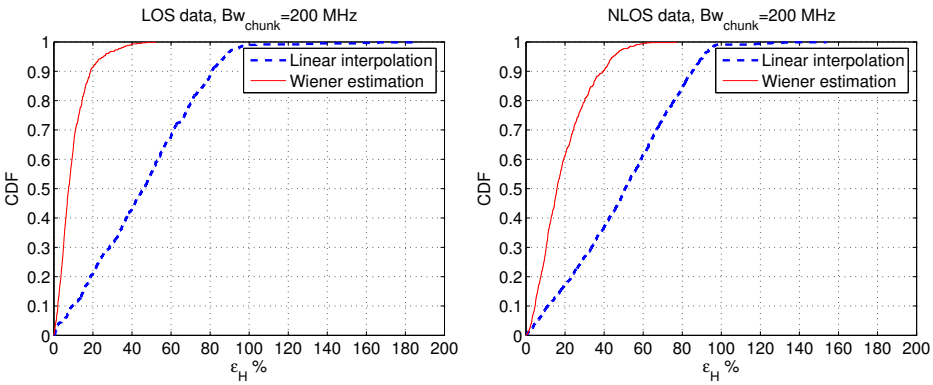

Figure 6.5: *CDF of the estimation error for $\widehat{H}_2(f)$ using the linear interpolation and frequency correlation approach with 200 MHz sub-bands (B_w = 600 MHz).*

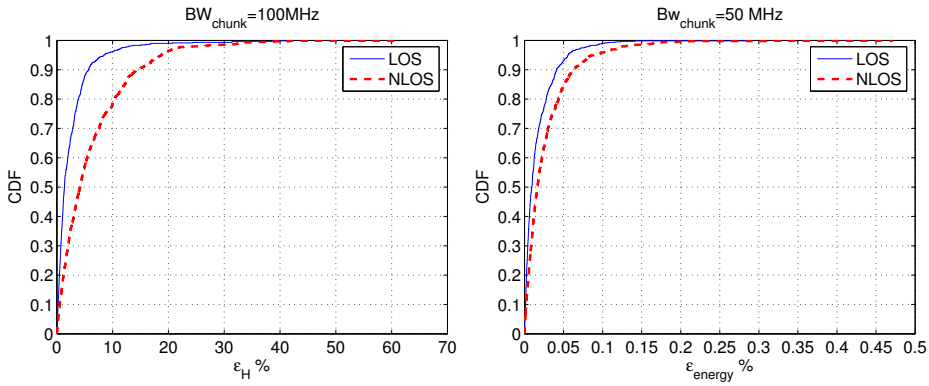

Figure 6.6: *CDF of the estimation error for $\widehat{H}_2(f)$ using the frequency correlation approach with a chunk width of: 100 MHz (left) and 50 MHz (right).*

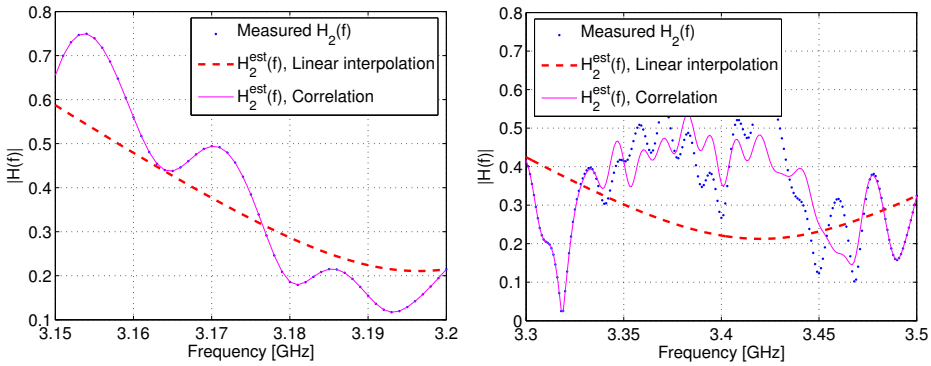

Figure 6.7: *Estimated missing chunk $\widehat{H}_2(f)$ using the frequency correlation approach with: $B_w = 50$ MHz (left) and $B_w = 200$ MHz (right).*

6.4 Important parameters of the model

In this section, some important parameters of the proposed model are introduced. Here we only discuss the frequency correlation approach to estimate the missing sub-bands as it provides better results than the linear interpolation method. More results based on the interpolation method can be found in [91, 92].

6.4.1 Effective bandwidth

We assume that the UWB band is divided into N sub-bands and the width of each sub-band (chunk) is $B_{w_{nb}}$. For a good understanding of the method, the concept of effective relative bandwidth $B^{rel}_{w_{eff}}$ is introduced. This parameter gives the percentage of effective bandwidth in the available UWB band:

$$B^{rel}_{w_{eff}} = \frac{N_c}{N} 100\% \tag{6.34}$$

where N_c is the number of useable chunks. For the simulations, we assume a bandwidth $B_w = 500$ MHz which fulfills the UWB definition and $B_{w_{nb}} = 10$ MHz which gives us a total of 50 chunks. We also assume that the starting and ending chunks are always present. For different effective bandwidths the chunks are assumed to be uniformly distributed along the frequency axis as shown in Figure 6.8. The CDF of the estimation error for different effective bandwidths are given in Figure 6.9. From this figure we observe that the larger the effective bandwidth the lower the estimation error. Clearly, when the effective bandwidth is high the number of useable chunks is also high and hence the frequency spacing between the chunks is small. This means that the correlation is higher and accurate estimation is obtained. It can also be concluded that sounding the channel with 10 MHz each 50 MHz is enough to estimate the whole UWB channel.

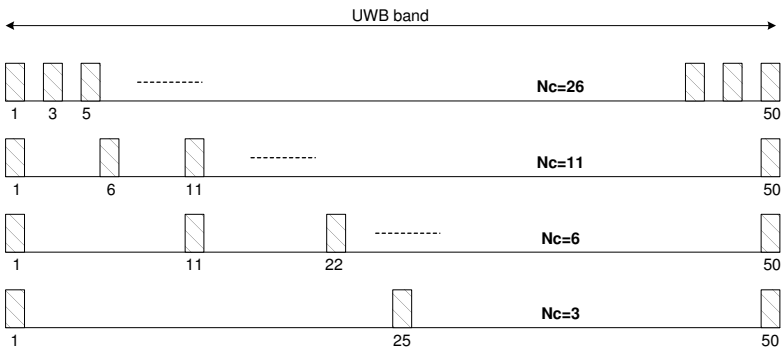

Figure 6.8: *Illustration of the Uniform pattern of the available chunks.*

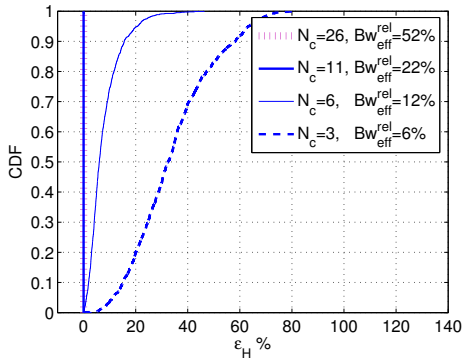

Figure 6.9: *The CDFs of the estimation error for different effective relative bandwidth using uniform chunk pattern.*

6.4.2 Chunks' pattern

The selection of useable chunks is important for the modeling approach. Beside the uniform chunk distribution we have also worked out different distributions (patterns) of the known sub-bands as visualized in Figure 6.10. The corresponding results are plotted in Figure 6.11. From this figure we learn that a lower estimation error is attained when the chunks are uniformly (equally) spaced. The results for the case of begin and end concentrated chunk patterns are the same because the frequency spacing of the missing chunks is the same.

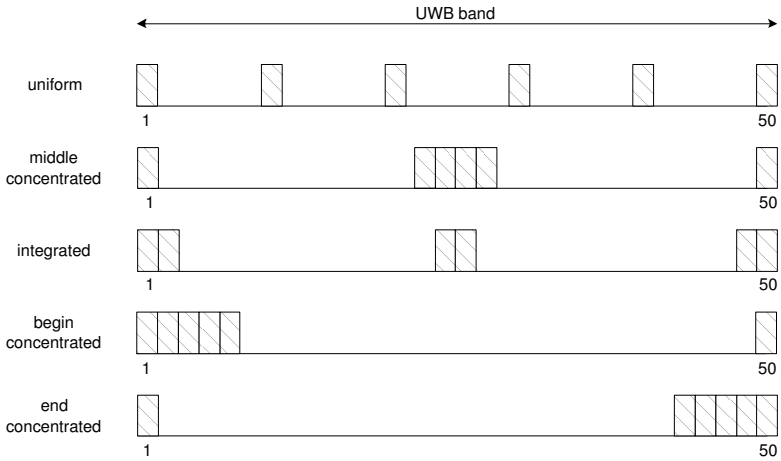

Figure 6.10: *Illustration of different patterns of available chunks.*

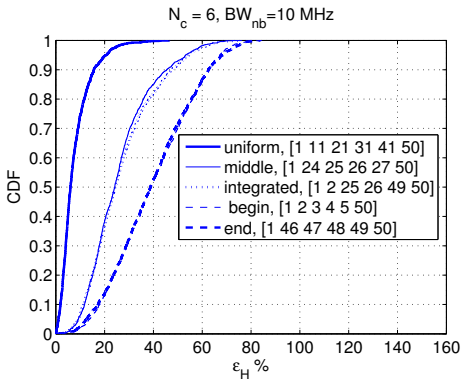

Figure 6.11: *The CDFs of the estimation error for different patterns of the chunks.*

6.4.3 Chunk width

So far, we have assumed a chunk width of 10 MHz. However, as we have seen that the correlation is so high between chunks with narrow widths, it is relevant to investigate what the minimum width of each chunk should be for a wanted estimation accuracy. This width might be important in connection to the effective bandwidth as well as the complexity of the system. For instance, performing measurements over a narrow-band seems to be easier than over a wide band. To this end, we assumed a fixed number of useable chunks $N_c = 11$ with different widths of for example, 5 MHz, 2.5 MHz, 1 MHz and 0.5 MHz, and keeping the same chunk pattern as shown in Figure 6.12. This means that the number of the total chunks is different for different widths and hence also different effective bandwidth are obtained. For example if $B_{w_{nb}} = 1$ MHz the total number of chunks is $N_c = 500$, and hence the effective relative bandwidth is $B^{rel}_{w_{eff}} = 11/500 = 2.2\%$.

The estimation error for different chunk widths is given in Figure 6.13. From this figure it can be observed that for a chunk width of 2.5 MHz or higher, the estimation error is very small. We note that by using an effective relative bandwidth of 5.5% we could retrieve the UWB-CIR with less than 1% error. However, for a chunk width of 1 MHz the error is a bit higher and is the same for 0.5 MHz. The same error is obtained because the correlation within a 1 MHz band is very high and the estimation between 2 adjacent 0.5 MHz sub-bands is accurate. The higher error for 1 MHz and 0.5 MHz is due to the frequency spacing between the chunk which is large when compared to 5 MHz. Another reason is that because the first and last chunks are assumed to be always present and hence, only one side correlation of these chunks is incorporated in the estimation. This means that it will be better to shift the first and last chunk a bit from the edge. Figure 6.14 shows the effect on the estimation error when the first and last chunk are shifted inside the UWB band. It is clear from this figure that the error is

less when shifting the two chunks with 10 MHz. For the case of using 0.5 MHz chunk width ($B^{rel}_{w_{eff}} = 1.1\%$) the estimation error is less than 10% for a CDF > 90%. One way to reduce this error is to add a few chunks and place all chunks uniformly. Figure 6.15 shows the estimation error for different number of useable chunks $N_c = 20$, 15, 11 and a chunk width of 0.5 MHz. From this figure we can see that the error decreases when increasing N_c. The average estimation error is less that 0.2% when $N_c = 15$ or $B^{rel}_{w_{eff}} = 1.5\%$. Smaller chunk widths can be used; however, the processing time dramatically increases because the matrixes R_c and r_c become huge due to the total number of chunks.

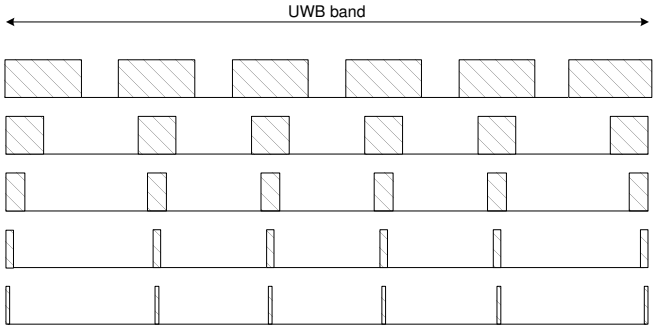

Figure 6.12: *Illustration of different pattern of the available chunks.*

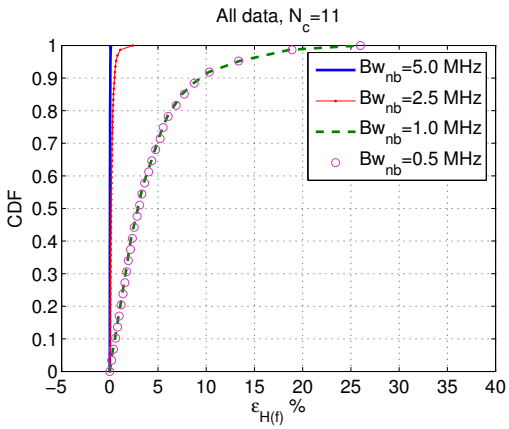

Figure 6.13: *The CDFs of the estimation error for different widths of the chunks.*

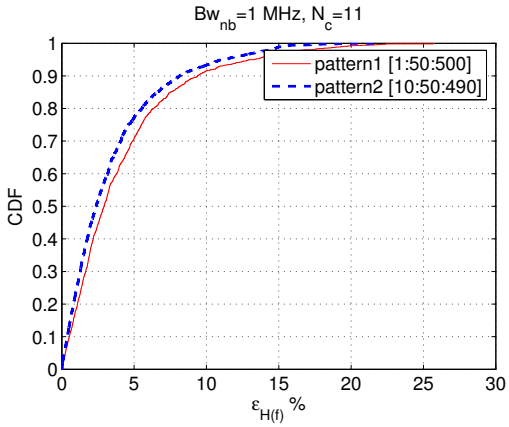

Figure 6.14: *The effect of shifting the starting and end chunks with 10 MHz towards the center frequency.*

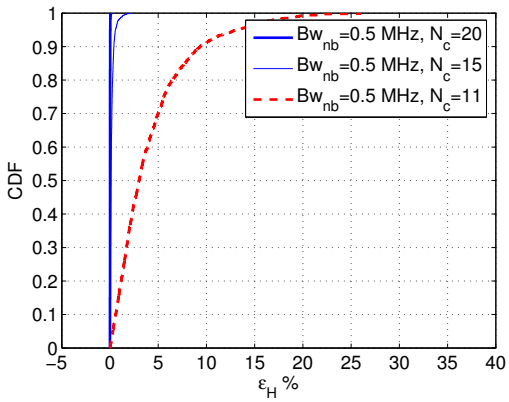

Figure 6.15: *Effect of the number of chunks using a small width of 0.5 MHz.*

6.4.4 Center frequency

The operational frequency influences transmission through objects, diffraction and scattering [93, 94]. The variation of the channel propagation properties directly influences its multipath profile. It turns out that the CIR in a given sub-band can be considerably different from another one depending on its spectral location within the UWB band. The objective of this paragraph is to check the dependence of the frequency correlation approach for different center frequencies. Up till now all results use the frequency band 3.1-3.6 GHz. To evaluate the accuracy of the model, different center frequencies are used. For instance, the total measured UWB bandwidth from 3.1 to 10.6 GHz is divided into 500 MHz bands. Then for each center frequency we have kept the model parameters like chunk pattern, effective relative bandwidth and chunk width the same for all simulations. The collected results on the estimation error are given in Figure 6.16. This figure shows that the estimation of the missing chunks does not strongly depend on the center frequency. Some small fluctuations in the results are due to the frequency selectivity of the channel.

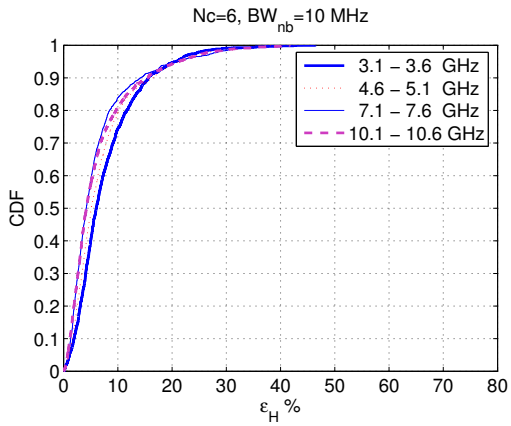

Figure 6.16: *The CDFs of the estimation error for different center frequencies.*

6.5 Impact of the model on channel parameters

In this section, we applied the proposed model to estimate some important channel parameters like large-scale path-loss and time dispersion. Here we assume a total bandwidth of 500 MHz, a chunk width of 0.5 MHz and different effective relative bandwidths. The path-loss and rms delay spread (RDS) are defined in Chapter 2. The same proposed model for path-loss in Chapter 4 is used here. Figures 6.17 and 6.18 gives the measured and estimated results of the path-loss model and its parameters using the frequency correlation approach for LOS and NLOS cases, respectively. The number of available chunks is 10 which means that $B^{rel}_{w_{eff}} = 1\%$. From these figures we can see that a very small difference is obtained between the true and estimated path-loss exponent and standard deviation of the shadowing. Collected results of the RDS are given in Figure 6.19. From this figure we can see that the error in the RDS is about 1 ns for both LOS and NLOS. Increasing the number of available chunks to only 15, or $B^{rel}_{w_{eff}} = 1.5\%$, gives perfect estimation for both path-loss and RDS, as can be seen in Figure 6.20

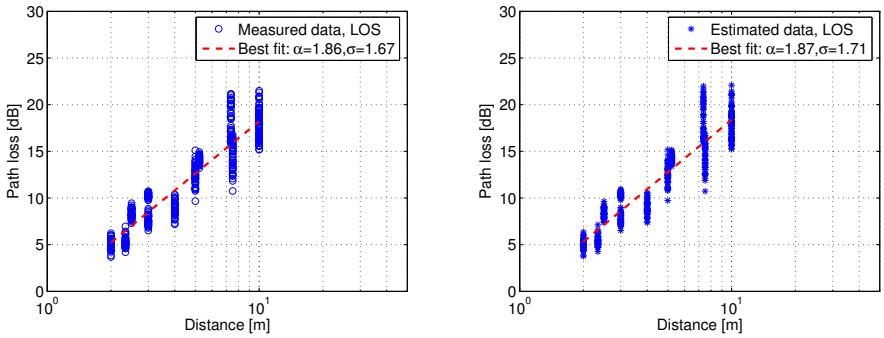

Figure 6.17: *Path-loss statistics for LOS using $N_c = 10$: measured (left), estimated (right).*

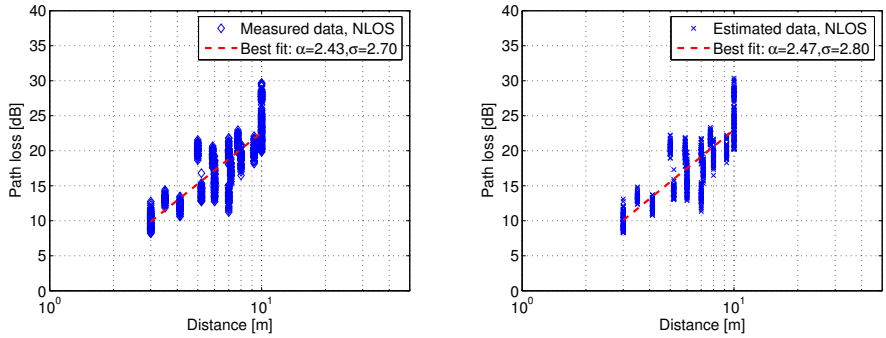

Figure 6.18: *Path-loss statistics for NLOS using $N_c = 10$: measured (left), estimated (right).*

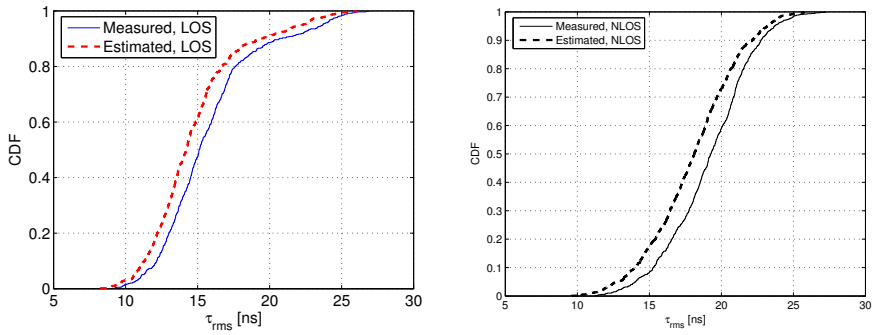

Figure 6.19: *Rms delay spread measured versus estimated: LOS (left), NLOS (right) for $N_c = 10$.*

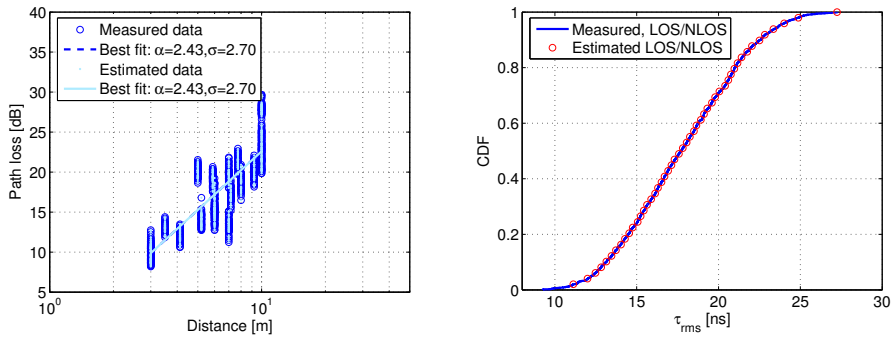

Figure 6.20: *Path loss statistics (left) and rms delay spread (right) for using $N_c = 15$.*

6.6 Conclusions

In this chapter, a new approach to estimate the UWB channel based on measured sub-channels is introduced. Different channel measurements over small bandwidths are first carried out. Then the channel impulse responses of all each sub-bands are integrated to estimate the whole UWB channel. This approach is extended to the case where not all sub-bands are available (i.e. partial information). To estimate the missing information the frequency correlation approach has been used. This approach is based on incorporating the correlation properties between all sub-bands which are needed as an a-priori knowledge. This correlation can statistically be determined from measurements.

The results show a good agreement between the model and measurements. Important parameters of the model are the effective relative bandwidth, the distribution pattern of useable chunks and the width of each chunk. Results show that by increasing the effective bandwidth the error in the UWB channel estimation decreases. This is because while increasing the effective relative bandwidth the frequency spacing between the sub-bands decreases and hence a higher correlation can be expected. In other words, if the frequency spacing is comparable to the coherence bandwidth of the channel a good estimation is obtained. The obtained results show that a uniform distribution pattern of the chunks over the UWB frequency band is the best choice to obtain a good channel estimation. It can be concluded that measuring small chunks can provide more or less the same performance as measuring large chunks. The proposed model is applied to estimate major channel parameters like path-loss and rms delay spread. Results are more than satisfactory for an effective relative bandwidth of 1.5% and leading to no error in the channel statistics.

From the point of view of system design, the proposed approach can reduce the complexity of the UWB system as only knowledge on a small number of chunks is needed. This also means that the transmit energy can be remarkably reduced. Measuring over small bands may reduce the high sampling rates needed for the implementation of UWB systems.

Chapter 7

Application of UWB for Ranging in Dense Indoor Multipath Environments

7.1 Introduction

Positioning information in indoor environments is becoming more important and attractive especially for wireless ad-hoc networks and area dependent services, logistics and emergency managing. One of the main issues in positioning is how to achieve a good range estimation. Usually, the range accuracy depends on the application and can range from a few centimeters to tens of meters.

Current positioning systems, like GPS, or future systems, like the European GALILEO, may not be available or do not have sufficient accuracy in specific areas where these future applications will operate, e.g. in city-centers and indoor locations. The poor performance of these satellite systems for supporting those applications is mainly caused by attenuation due to signal blocking and/or multipath signals which cause distortion of the direct signal [1].

UWB radio seems to be a prone solution for achieving a high accuracy [95–102]. Clearly, the extremely large bandwidth offered by UWB systems allows a fine time resolution of the multipath components of the received signal. Accordingly, it is possible to reach accurate range estimation when TOA/TDOA (Time Of Arrival/Time Difference Of Arrival) techniques are used to detect the first path of the received signal. However, the implementation of the receiver remains chal-

[1] The primary reason of performance degradation is not the presence of multipath itself but the fact that multipath can not be resolved due to the (relatively) small signal bandwidth used by current positioning systems.

lenging since usually very high sampling rates are required. To make the system feasible a trade-off between receiver complexity and range accuracy has to be addressed regarding the system design.

The aim of this chapter is to investigate ranging using UWB signals for indoor dense multipath environments based on measured channel impulse responses. Two different estimation methods to detect the time of arrival of the first path are evaluated, and the effect of the bandwidth on range estimation is analyzed. The ranging results obtained with time-based estimation methods are compared to those based on signal strength. In addition to this, ranging based on partial measured frequency responses is investigated. This chapter is organized as follows. In section 7.2, different estimation methods are discussed. In section 7.3, the ranging results are presented followed by a discussion. In section 7.4, ranging based on measuring partial chunks is addressed. In section 7.5, concluding remarks are provided.

7.2 Range estimation methods

Two different range estimation methods are considered below.

7.2.1 Time of Arrival estimation

This method is based on the estimation of the time of arrival of the first path, which is usually assumed as the one corresponding to the direct ray path coming from the transmitter.

If two nodes have a common clock, the node receiving the signal can determine the ToA of the incoming signal which is time-stamped by the reference node. From the travel time the distance d can be derived:

$$d = c \cdot \tau, \tag{7.1}$$

where c is the speed of light and τ is the travel time. Relying on a path-loss model, the distance between two nodes can be estimated by measuring the energy of the received signal at one node. The estimated distance defines a circle around the reference node with a radius of the estimated distance.

Two different algorithms have been implemented and compared according to their complexity and performances. The former is based on the deconvolution in the frequency domain of the received signal, to detect the time of arrival of the first path, the latter is based on the energy detection of the first component of the received signal. The second approach offers the possibility to implement the receiver in the analogue domain, thus greatly reducing its complexity.

Frequency deconvolution of the received signal

Figure 7.1 shows the block diagram for the proposed receiver. It consists of a bandpass filter (BPF), a low noise amplifier (LNA) and an analogue to digital

converter. To allow a reconstruction of the signal, it is necessary to sample the received waveform at least at the Nyquist rate. The drawback of such a receiver is that a very high sampling rate (i.e. in the order of GHz) is needed. To retrieve

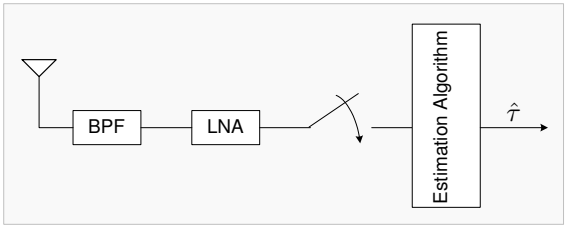

Figure 7.1: *Digital implementation of the receiver for estimating the travel time $\hat{\tau}$.*

the time of arrival of the first path from the measured signal, it is necessary to estimate the channel impulse response. The received UWB signal is affected by both transmitter and receiver antenna characteristics and by the measurement system (i.e. cables, filter and LNA). To exclude these effects from the measured signal, a reference signal measured at 1 m is used. The impulse response of the UWB channel is obtained by deconvolving the received signal with the reference signal. The deconvolution is done in the frequency domain using the inverse filtering (IF) technique. This algorithm is based on dividing the spectrum of the received signal by that of the template. The division is done only for parts of the spectrum in which the power of the template is non-zero and within the desired frequency band (e.g. 3.1-10.6 GHz). The rest of the spectrum is filled with zeros. Taking the complex baseband IFFT, the complex impulse response of the channel is obtained. To reduce the leakage problem of transforming the signal back to the time domain, a Hamming window which provides side-lobes less than -43 dB is used. The paths are estimated by detecting local maxima. A cut-off (i.e. threshold) of 20 dB from the strongest path is used to avoid the detection of side-lobes or noise. Then the time of arrival of the first path is estimated, by choosing the first local maximum.

Energy detection of the received signal

To avoid very high sampling rates required by the previous solution, we can use an algorithm based on the energy detection of the first component of the received signal together with the analogue receiver depicted in Figure 7.2. The observation window is divided into $N = \frac{T_w}{T_b}$ bins, where T_b is the bin size and T_w is the acquisition time window. To detect the time of arrival of the first path, a bank of N integrators is used. Each integrator calculates the energy of one of the N bins every T_w seconds, as shown in Figure 7.3. We choose as estimation of the time of arrival of the first path the center of the first bin whose energy E exceeds

a given threshold ξ:

$$\hat{\tau} = T_0 + (\min(n|E(n) > \xi) - 0.5)T_b \tag{7.2}$$

where

$$E(n) = \int_{T_0+(n-1)T_b}^{T_0+nT_b} |r(t)|^2 dt \tag{7.3}$$

$r(t)$ is the received signal, T_0 the starting integration time and the index n varies between 1 and N. In the following we fix $T_w = 150$ ns and $T_b = 1$ ns. With the proposed receiver, there is no need of sampling the signal at the Nyquist rate since the integrators work in the analogue domain and processing requirements are largely relaxed.

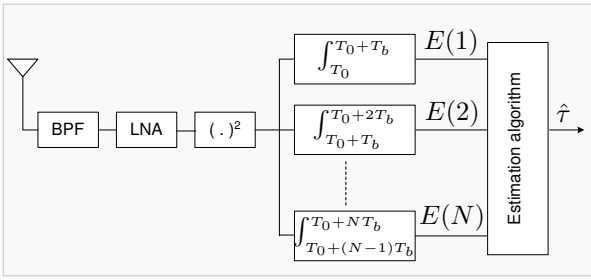

Figure 7.2: *Analogue implementation of the receiver.*

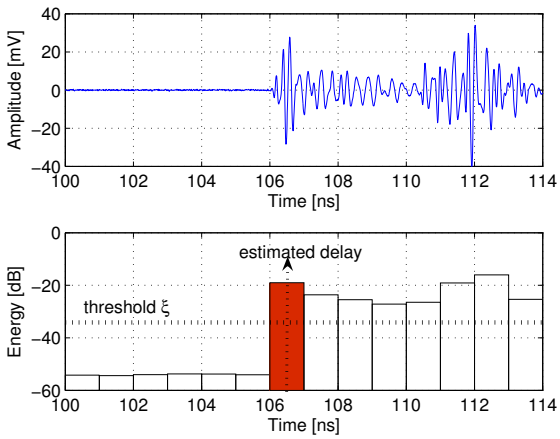

Figure 7.3: *Received signal and integrators output using 1 ns bin size.*

7.2.2 Signal Strength estimation

The signal strength measurement approach might be an alternative to time-based ranging. It does not require the signal time of flight calculation either accurate clock synchronization between transmitter and receiver. Range estimation $\hat{d}$ is performed according to the following formula:

$$\hat{d} = d_0 \left(\frac{P_r(d_0)}{P_r(d)} \right)^{\frac{1}{\alpha}} \tag{7.4}$$

where $P_r(d)$ is the measured power at distance d, d_0 is the reference distance and α is the path-loss exponent. The results provided by this technique are strictly related to the accuracy of the model for the path-loss exponent. Reference [103] provides a characterization of α for the locations considered. We expect acceptable performance provided by this technique, mainly for short distances, since the large bandwidth used allows for a considerable reduction of fading effects. On the contrary, for narrow-band systems, fading in indoor environments can cause a variation of more than 10 dB in the received power, thus greatly limiting the accuracy of the range estimation based on signal strength measurements.

7.3 Results and discussion

7.3.1 Time of Arrival estimation

From the time of arrival of the first path, the distance is estimated and compared to the true measured distance. The error made in the range estimation is defined as:

$$\varepsilon = |d - \hat{d}| \tag{7.5}$$

Frequency deconvolution of the received signal

Figure 7.4 gives the cumulative distribution function (CDF) of the range error using the proposed inverse filtering with first path detection algorithm both for LOS and NLOS propagation, when the full bandwidth from 3.1 to 10.6 GHz is used. From this figure it can be seen that the obtained range error for LOS is considerably smaller than for NLOS. The mean and the standard deviation of the range error are respectively about 2.16 cm and 1.12 cm for LOS, and 15.78 cm and 6.91 cm for NLOS. It is clearly visible that the standard deviation of the NLOS range error is remarkably higher. This is confirmed by the changeover of the data from region A to B and from region B to C as indicated in Figure 7.4. This changeover is related to some physical features of the propagation channel like walls. Therefore, to investigate this effect, the data are divided into groups according to the number of walls situated between the transmitter and the receiver. According to the measurement scenario depicted in Figure 4.1, only data

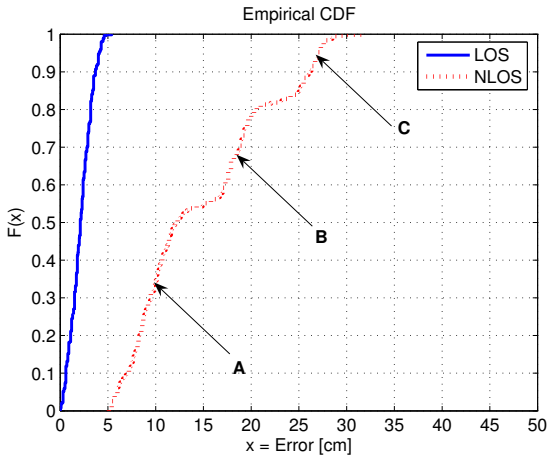

Figure 7.4: *Range error using frequency deconvolution with first path detection algorithm for LOS and NLOS propagation.*

from office to office are considered because the walls for this scenario are the same regarding the thickness and the construction material. It should be noted that the thickness of each wall is about 15 cm and they are made of concrete. In total three cases (see Chapter 4, Figure 4.1) can be distinguished: 1 wall propagation (Rx3-Tx3,1, Rx3-Tx3,2, Rx3-Tx3,3, Rx3-Tx3,4, Rx3-Tx3,5, Rx3-Tx3,6), 2 walls propagation (Rx3-Tx3,7, Rx3-Tx3,8, Rx3-Tx3,9) and 3 walls propagation (Rx3-Tx3,10, Rx3-Tx3,11). The range error for office to office propagation as function of the number of walls is presented in Figure 7.5. The additional range error $\Delta\varepsilon$ provided by the propagation through a single wall is (for perpendicular incidence):

$$\Delta\varepsilon = \frac{d_w}{c}(\sqrt{\varepsilon_r} - 1) \tag{7.6}$$

where d_w is the thickness of the wall, c is the speed of the light in vacuum and ε_r is the dielectric constant of the material. Reference [104] provides a characterization of the dielectric constant for walls made of different materials. From this reference we have taken $\varepsilon_r \simeq 2.4$ for a concrete wall for the frequency band of interest; the additional range error per wall becomes $\Delta\varepsilon \simeq 8.24$ cm. This agrees well with the values shown in Table 7.1.

As a further step we analyzed the effect of the bandwidth on the range estimation error. The obtained results are given in Figure 7.6. From this figure it can be underlined that the error increases when the bandwidth decreases. However, the results also show that a 2 GHz bandwidth appears to be enough in order to achieve maximum accuracy provided by the algorithm, since there is almost no difference between the CDF of the error when 2 GHz or the full bandwidth of

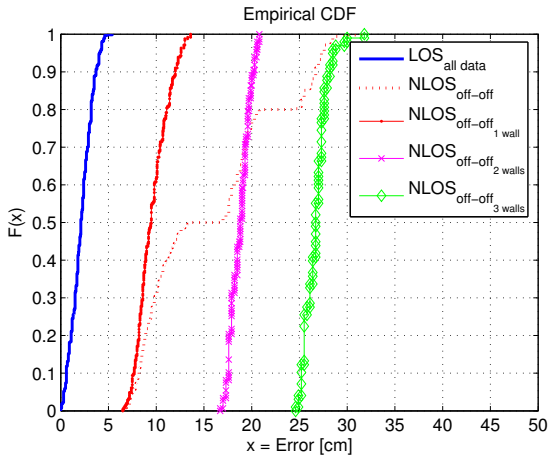

Figure 7.5: *Range error using frequency deconvolution with first path detection algorithm for LOS and NLOS office to office propagation.*

Table 7.1: *The mean and standard deviation (std) of range error for different propagation conditions.*

range error / propagation	mean [cm]	std. [cm]
1 wall	9.61	1.61
2 walls	18.78	1.00
3 walls	26.73	1.20
LOS	2.16	1.12
NLOS	15.78	6.91

7.5 GHz is used. In this situation, the main source of error is the additional delay introduced by walls. Decreasing the bandwidth to 1 GHz or less, the proposed algorithm provides additional errors. On average, the increase in error due to a reduced bandwidth is limited to 7 cm, also in most critical situations. However, for 5% of the measurements the error is really large especially for NLOS propagation, and reaches a value of 1.5 m when 500 MHz is used. This is due to the fact that in some cases the described algorithm is not able to distinguish multipath components which arrive within a time interval which corresponds to the inverse of the bandwidth. This causes the missed detection of the first path, and wrong detection of a different one.

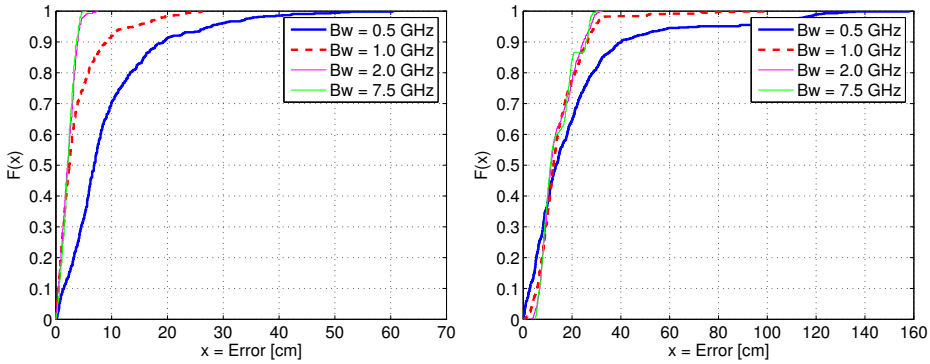

Figure 7.6: *Range error for LOS (left) and NLOS (right) propagation using frequency deconvolution with first path detection algorithm for different bandwidths.*

Energy detection of the received signal

Figure 7.7 gives the CDF of the range error using the energy detection algorithm described in the previous section, both for LOS and NLOS propagation and for different bandwidths. When the full bandwidth is used, the mean and the standard deviation of the range error are respectively 8.05 cm and 5.69 cm for LOS, and 15.87 cm and 10.45 cm for NLOS. The worse performances compared to the first algorithm described are mainly due to the choice of the bin size. In fact taking $T_b = 1\ ns$, introduces a maximum error of 15 cm in range estimation. Also for this approach the use of small bandwidths introduces an acceptable degradation in the range estimation. For LOS propagation the obtained performances remain almost identical when the bandwidth is reduced to 500 MHz. For NLOS the average error increases by about 3 cm for 2 GHz bandwidth and by 7 cm for 500 MHz. The larger errors in Figure 7.7 appear in those scenarios in which the SNR of the received signal is lower. However, when the SNR is high, decreasing the bandwidth doesn't affect the range estimation accuracy notably. It is worth underlining that the second proposed algorithm appears to be more robust to the bandwidth reduction since it does not estimate the single multipath components of the received signal, but it looks for the time of arrival of the first energy components of the received signal. Thus, it does not suffer so much from the problem of missed path detection like the first approach.

The possibility of using relatively small bandwidths appears an interesting feature for both described receivers. Using smaller bandwidths is useful for digital implementation, since it allows for a reduced sampling rate required to correctly process the signal. The energy detector scheme proposed in the second approach can profit from this feature. In fact it is very sensitive to noise and interference, which in this way can be more easily avoided by selecting an interference free

bandwidth.

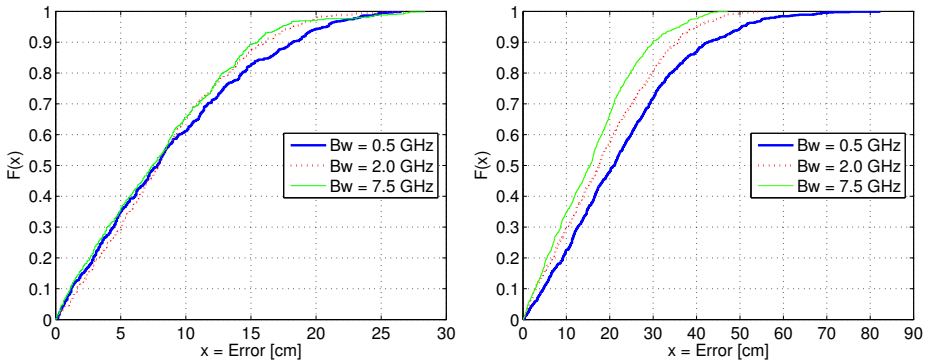

Figure 7.7: *Range error for LOS (left) and NLOS (right) propagation using an energy detector receiver; parameters: different bandwidths.*

7.3.2 Signal Strength estimation

Before estimating the distance the path-loss exponent should be retrieved from the measured data. This can be done by combining all data for each LOS and NLOS measurements (see section 4.3). The distance is accordingly estimated. Figure 7.8 shows the range error with error bands as a function of distance. From the results it can be seen that the variance of the estimation error increases with distance. This agrees with the behavior predicted by the Cramer Rao bound for signal strength based ranging [95]. In addition to this, several biased errors in the range estimates can be observed. This is because we have used a path-loss exponent model for all combined locations. It turns out that for some locations the received power does not match perfectly the model. In principle it is possible to reduce the bias error by having a more detailed description of the environment and accordingly using different values of α depending on the position [103]. However, this does not appear as a correct way to proceed, since in order to select the correct value of α it is necessary to have partial knowledge about the location of the user, which has to be determined. With this technique the 90% probability gives a range error less than 2.5 m. This error is much higher when compared to that obtained by time of arrival estimation. However, for some applications this may be a sufficient accuracy which is then a cost-effective implementation.

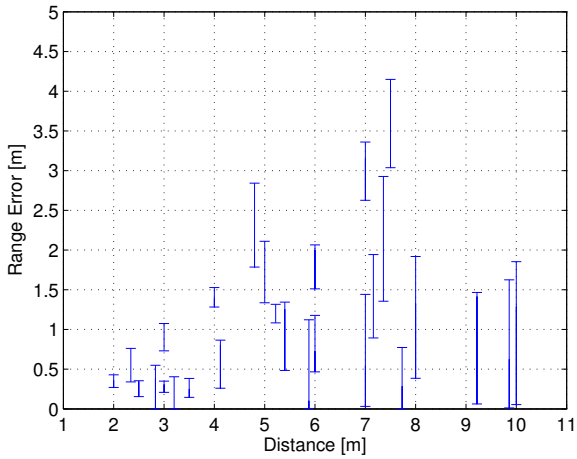

Figure 7.8: *Range error for all data using the signal strength method.*

7.4 Ranging based on partially measured frequency responses

In Chapter 6, we have shown that the UWB channel can be estimated based on partially measured frequency responses. In this section, this approach is applied to UWB ranging. To this end, the obtained range error for a full UWB bandwidth is compared to that obtained when partial chunks are measured and the missing chunks are estimated using the frequency correlation approach described in Chapter 6. Here, only the time of arrival estimation with the maximum peak detection method is used to investigate the ranging accuracy. For the signal strength estimation method the results can be concluded from Figure 6.10 of section 6.5. There, we have shown that the total received power estimated using partial measured frequency responses is the same as for a full bandwidth. To quantify the use of this approach in UWB ranging applications, we define an estimation error $\Delta\varepsilon$ as the difference between the range error when a full and partial bandwidth are measured:

$$\Delta\varepsilon = |\hat{d}_{FB} - \hat{d}_{PB}| \tag{7.7}$$

where $\hat{d}_{FB}$ and $\hat{d}_{PB}$ are the estimated distance using the full and partial bandwidth, respectively. For the simulation we assumed a total bandwidth of 500 MHz and a width of 500 KHz for each chunk (i.e. 1000 chunks in total). Figure 7.9 gives the CDF of $\Delta\varepsilon$ for different effective relative bandwidths (see eq. (6.33)). From this figure it can be concluded that the larger the effective relative bandwidth the smaller is the difference in the error range. According to these results, an effective relative bandwidth of 2% seems to be enough to get the same UWB range

accuracy as when a full bandwidth is used, which confirms the results obtained in Chapter 6. Moreover, for $B^{rel}_{w_{eff}} = 1\%$ the range error gets higher values (between 0.5-10 m) for a probability greater than 0.6. This can be explained by the fact that the frequency spacing between the available chunks is large and hence the estimation of the UWB channel is less accurate. Thus, errors can be observed in the magnitude of the UWB frequency response as well as in the phase. Errors in the phase may lead to delay shifts of the UWB-CIR and hence the TOA of the first multipath components. Another reason of these higher errors might be due to the threshold setting. Clearly, spurious peaks (i.e. side-lobes) can be expected in the reconstructed CIR as a consequence of imperfect estimation. The effect of the threshold setting on the range error has been investigated, see Figure 7.10. From this figure we can see that by increasing the threshold the error increases. A threshold setting between 5-10 dB from the peak provides better estimation results.

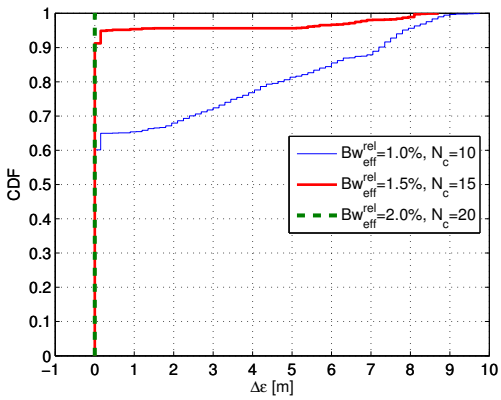

Figure 7.9: *The difference in range error using different effective bandwidths for all data.*

7.5 Conclusions

In this chapter, we investigated ranging based on measured UWB channel impulse responses in indoor dense multipath environments. The obtained results show that very high accuracy can be achieved when UWB is used. Ranging based on time of arrival estimation gives a better performance than that based on signal strength measurements. Using algorithms based on the estimation of the time of arrival of the first path, errors of less than 5 cm can be achieved for LOS. NLOS propagation causes a degradation in range estimation of several centimeters due to additional delays introduced by the propagation of the signal through e.g. walls. This

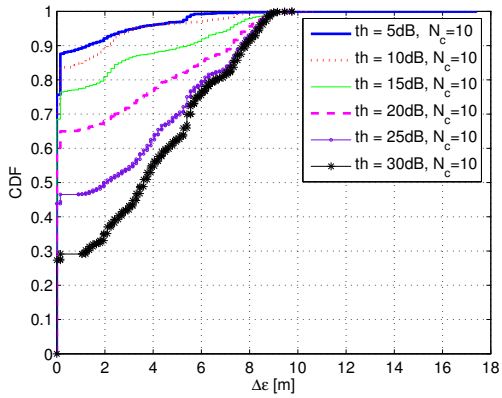

Figure 7.10: *The difference in range error as a function of the threshold.*

phenomenon appears to be a main factor limiting the range estimation accuracy. The additional range error is about 8-9 cm per wall made of concrete with a thickness of about 15 cm.

The investigation of a lower cost, analogue receiver based on energy detection, shows that it appears as a viable alternative for the complex digital implementations. In fact the proposed receiver shows slightly inferior performance, but computational requirements to process the signal are largely relaxed. The analysis shows that the range error increases when the bandwidth decreases. However, a 2 GHz bandwidth appears enough to get the same range accuracy as for a system which exploits the full 7.5 GHz bandwidth. When the bandwidth is further reduced down to 500 MHz, the algorithm based on energy detection of the first component experiences only small performance degradation (few decimeters). On the contrary, the approach based on the estimation of single multipath components (frequency deconvolution) may produce large errors due to difficulties in resolving these paths when a too small bandwidth is used.

Ranging based on partially measured channel frequency responses was investigated. The results show the potential of this method in accurate ranging for dense multipath environments. Measuring 2% of the total UWB bandwidth of 500 MHz, provides the same accuracy as the case in which the full UWB bandwidth is known.

Chapter 8

Conclusions and Recommendations

In this thesis, we have developed relevant channel models to support UWB communication systems design and evaluation. The statistical channel models have been developed based on measurements. Another modeling approach based on deterministic methods can also be used; however, it is not the focus of this thesis. To study and develop the UWB channel models, several measurement campaigns were performed. For instance, a large set of UWB channel measurements, covering the frequency band 3.1-10.6 GHz, has been conducted in different environments which has been used to provide a good statistical analysis. Different kinds of signal variations, e.g. large, middle and small-scale fading, have been modeled. In most available UWB channel models it is assumed that the far-field conditions of the antennas are satisfied. However, in some short-range high-speed UWB applications, e.g. WPAN or WBAN, this assumption is not valid and hence the reported models in the literature are not accurate. In this thesis, we have analyzed the near-field problem and modeled its effects on the link budget using different antennas. In addition, we have investigated the possibility of using partial measured frequency responses to estimate the whole UWB channel impulse response. Finally, we have applied the measured data to investigate the application of the UWB for ranging in indoor dense multipath environments.

In this chapter, the main contributions and conclusions of this thesis are outlined, and some recommendations for open research topics are given.

8.1 Conclusions

The conclusions are classified according to the UWB measurements, channel modeling and applications.

8.1.1 UWB measurements

- The UWB channel measurements can be performed either in time- or frequency-domain. In principle, there should be no difference in the modeling results between these two techniques. However, there are some engineering trade-offs to be made between them.

  The frequency-domain technique provides a higher dynamic range than the time-domain technique. For the time-domain technique, the spectrum of the transmitted pulse is not uniform over all frequencies (e.g. usually decreases with frequency) due to practical difficulties in designing transient UWB time domain pulses which have a flat spectrum over a large frequency band (e.g. 3.1-10.6 GHz). This results in a limited signal to noise ratio for higher frequencies which causes measurement difficulties.

- A major challenge in UWB channel measurements is that the measurement bandwidth is open to any signal. For instance, when a narrow-band interferer is active during the UWB channel measurements, under-sampling applied in the stroboscopic sampling receiver (which is a typical solution for a time-domain channel sounder) results in a spreading of the energy of non synchronized (to the stroboscope) narrow-band signals over the whole measured spectrum as quasi-white noise. The level of this additional noise is relatively high and its suppression is required in order to increase the dynamic range.

  To suppress the in-band and out-of-band narrow-band interference an analogue bandpass filter has to be used directly after the receive antenna. This decreases the noise and results in a substantial improvement of the dynamic range of the measurements (e.g. 25 dB in our measurements).

- The acquisition time window in the time-domain measurements is usually limited. One way to solve this limitation is to measure successive time windows and combine them to get a larger time window. However, this may introduce errors due to the inaccuracy of the delay setting of the oscilloscope.

  To avoid this problem, we have introduced a new method "Overlap Time Interval", which allows measurements over larger time windows eliminating the error introduced by the oscilloscope delay setting.

- In case of mismatch between generator and transmit antenna, multiple antenna reflections will occur in UWB measurement systems. They result in distortion of the measured channel impulse response and may lead to erroneous modeling of the UWB channel's power delay profile because extra "artificial" paths are measured. This phenomenon, which causes overestimation of the channel statistics e.g., arrival rates, rms delay spread and excess delay, should be carefully considered and distinguished from actual multipath effects which are modeled by the double exponential model.

A simple way to exclude the effect of multiple antenna reflections is to use a long cable between the pulse generator and the antenna; however, this solution is at the cost of additional attenuation, depending on the cable characteristics.

8.1.2 UWB channel modeling

- The measured UWB signal is affected by the characteristics of the antennas. This effect can be *partially* compensated by deconvolving the measured UWB signal with a reference signal.

  All proposed UWB channel models are antenna dependent. In this thesis, omni-directional antennas have been selected for the measurements, which are most often used in practice. It turns out that the proposed models still provide a good description of the UWB channel.

- To estimate the channel impulse response, the inverse filtering deconvolution method was used rather than the CLEAN algorithm. Due to the iterative approach of the CLEAN algorithm artificial paths are produced for cases in which the received pulses overlap with each other and/or the pulse shape is not the same as the reference, which is usually the case. Using inverse filtering the obtained channel impulse response is continuous in nature. Therefore, to estimate the multipath components we have used the maximum detection method which is based on the detection of local maxima.

  The maximum detection method provides better and more accurate results than the conventional discrete channel impulse response method for estimating the multipath components of the UWB channel. This is due to the representation of one pulse by 2 or more paths by the latter method, and thus overestimates the statistics of the multipath components.

- The UWB signals are robust against fading. The fading margin strongly depends on the signal bandwidth and a difference of 20 dB can be expected when the bandwidth is decremented from 7.5 GHz to 10 MHz. Furthermore, the amplitude of the fading margin can be accurately modeled by the Nakagami distribution.

  For indoor office environments, the use of a measurement bandwidth of about 1 GHz is enough to resolve all paths and hence mitigate the multipath fading effect.

- The path-loss models used for narrow-band channels can also be used to model the path-loss for the UWB channels. However, the power variations around the UWB path-loss model are smaller than those for narrow-band channels. This is because UWB signals experience less fading and also have a good penetration capability through walls.

The path-loss exponent for very short range LOS scenarios (e.g. within 1 m) is less than 2 (value for free-space propagation) because of the near-field effect. For NLOS scenarios the value is around 0 because the direct path is totally blocked and the power is received either from wall reflection or from objects near the antennas.

- The small-scale fading can be modeled by the S-V model but with some modifications. In this model, the multipath components are modeled as a number of rays arriving within different clusters.

  The number of cluster is a function of the number of walls seen by both transmit and receive antennas. The cluster inter-arrival times and ray intra-arrival times can be modeled by a Gamma distribution and a mixture of two Poisson processes, respectively.

- The RDS for indoor office environments strongly depends on the room dimensions as well as the separation distance. The RDS statistics for industrial areas are higher than those for the office environment due to a higher multipath density caused by the metal structures in the channel.

- A new approach to estimate the UWB channel based on partially measured frequency responses is introduced. The main issue of this method is how to accurately estimate the frequency response of the channel at not-measured parts.

  The missing information is estimated based on the a-priori knowledge of the correlation information between the known and unknown chunks.

  - The estimation error of the whole UWB channel based on partially measured frequency responses depends on the effective relative bandwidth, the distribution pattern of the available measured chunks and the width of each chunk.
  - By increasing the effective relative bandwidth the error in the UWB channel estimation decreases.
  - The uniform pattern distribution of the chunks over the UWB frequency band is the best choice to obtain a good channel estimation.
  - Measuring small chunks can provide more or less the same performance as measuring large chunks.
  - The proposed approach can be applied to estimate major channel parameters like path-loss and rms delay spread.
  - From system design point of view, the proposed approach can reduce the complexity of the modeling of the UWB channel as only the knowledge of a small number of chunks is needed.

- A novel UWB link budget model for short-range applications under near-field antenna conditions has been proposed and validated.

  The near-field path-loss can be modeled as a modification factor for the losses as predicted under far-field antenna conditions. This correction factor takes into account all main effects due to the near-field conditions (i.e. phase error, antenna mismatch and reradiation between antennas) and includes frequency, antenna size and orientation dependencies.

  - For small antennas the received signal at short distances is mainly influenced by the phase error; however, for large antennas operating at low frequencies antenna mismatch and reradiation between antennas may become important as well.

8.1.3 UWB application for ranging

In this thesis, we have investigated ranging based on measured UWB channel impulse responses. The following major conclusions can be given.

- UWB signals provide a very high ranging accuracy in dense multipath indoor environments.
- Ranging based on ToA estimation gives a better performance than that based on signal strength measurements. Using algorithms based on the estimation of the time of arrival of the first path, range errors less than 5 cm can be achieved for LOS. NLOS propagation causes a degradation in range estimation accuracy of several centimeters due to additional delays introduced by the signal propagation through walls. This phenomenon appears to be a main factor limiting the range estimation accuracy.
- A low-cost receiver based on energy detection is a viable alternative to more complex digital implementations. In fact such receiver shows a slightly inferior performance, but computational requirements to process the signal are largely relaxed.
- The ranging error strongly depends on the operational frequency bandwidth and increases for decreasing bandwidth due to multipath effects.

  It was found that for indoor office environments a 2 GHz bandwidth is sufficient to get the same range accuracy (5-15 cm) as a system which exploits the full 7.5 GHz bandwidth. This is mainly due to resolving all multipath components when such bandwidth is used.

8.2 Recommendations

- The statistical analysis of the measured data was done using only one dimension (time) and hence the clusters were determined after visual inspection.

Therefore, we suggest to add a second (spatial) dimension using the angle of arrival of the multipath components. This approach will not only recognize each cluster but also all multipath components belonging to each cluster. This might provide more accurate models of the channel parameters e.g. cluster and ray arrival times.

- In this thesis, we have introduced a new approach to estimate UWB channels based on partially measured chunks of the frequency response. This approach can be extended to modeling of UWB channels based on already known medium/wide-band channel models.

- In this thesis, ranging based on measured UWB channel impulse responses has got initial investigations. Analysis and modeling of the range error and its statistics are suggested for further study.

Bibliography

[1] K. Siwiak, "Ultra-wide band radio: a new PAN and positioning technology," *IEEE Vehicular Technology Soc. News*, pp. 4–9, Feb. 2002.

[2] K. Siwiak, P. Withington, and S. Phelan, "Ultra-wide band radio: the emergence of an important new technology," *IEEE Vehicular Technology Conference, VTC-Spring*, vol. 2, no. 53, pp. 1169–1172, 2001.

[3] K. Siwiak, "Ultra-wide band radio: introducing a new technology," *IEEE Vehicular Technology Conference, VTC-Spring*, vol. 2, no. 53, pp. 1088–1093, 2001.

[4] G. Olhoeft, "The new ground penetrating radar regulatory environment," *9th International Conference on Ground Penetrating Radar*, pp. 1–6, Apr. 2002.

[5] FCC, "Revision of part 15 the commission's rules regarding ultra-wideband transmission systems," *ET Docket*, 2002.

[6] K. Pahlavan and A.H. Levesque, *Wireless Information Networks.* John Wiley, 1995.

[7] H. Hashemi, "The indoor radio propagation channel," *IEEE Proceeding*, vol. 81, no. 7, pp. 943–968, July 1993.

[8] Z. Irahhauten, H. Nikookar, and G.J.M. Janssen, "An overvieuw of ultra wide band indoor channel measuremenst and modeling," *IEEE Microwave and Wireless Components Letters (WMCL)*, vol. 14, no. 8, pp. 386–388, Aug. 2004.

[9] S.M. Yano, "Investigating the ultra-wideband indoor wireless channel," *IEEE Vehicular Technology Conference, VTC-Spring*, vol. 3, no. 55, pp. 1200–1204, 2002.

[10] D. Cassioli, M.Z. Win, and A.R. Molisch, "A statistical model for the UWB indoor channel," *IEEE Vehicular Technology Conference, VTC-Spring*, vol. 2, no. 53, pp. 1159–1163, Oct. 2001.

[11] R.J.M. Cramer, R.A. Scholtz, and M.Z. Win, "Evaluation of an ultra-wide-band propagation channel," *IEEE Transactions on Antennas and Propagation*, vol. 50, no. 5, pp. 561–570, May 2002.

[12] S.S. Ghassemzadeh, R. Jana, V. Tarokh, C.W. Rice, and W. Turin, "A statistical path loss model for in-home UWB channels," *IEEE Conference on Ultra Wideband Systems and Technologies, Digest of Papers*, pp. 59–64, May 2002.

[13] L. Hentila, A. Taparungssanagorn, H. Viittala, and M. Hamainen, "Measurement and modelling of an UWB channel at hospital," *IEEE International Conference on Ultra-Wideband*, vol. 1, no. 5, pp. 113–117, Sept. 2005.

[14] V. Hovinen, M. Hamalainen, and T. Patsi, "Ultra wideband indoor radio channel models: preliminary results," *IEEE Conference on Ultra-Wideband Systems and Technologies, Digest of Papers*, pp. 75–79, May 2002.

[15] J. Keignart and N. Daniele, "Subnanosecond UWB channel sounding in frequency and temporal domain."

[16] J. Kunisch and J. Pamp, "Measurement results and modeling aspects for the UWB radio channel," *IEEE Conference on Ultra Wideband Systems and Technologies, Digest of Papers*, pp. 19–24, May 2002.

[17] A. Muqaibel, A. Safaai-Jazi, A. Bayram, and S.M. Riad, "Ultra wideband material characterization for indoor propagation," *IEEE International Symposium on Antennas and Propagation*, vol. 4, pp. 623–626, June 2003.

[18] A.H. Muqaibel, A. Safaai-Jazi, A.M. Attiya, A. Bayram, and S.M. Riad, "Measurement and characterization of indoor ultra-wideband propagation," *IEEE Conference on Ultra Wideband Systems and Technologies*, vol. 1, no. 9, pp. 295–299, Nov. 2003.

[19] T.S. Rappaport, *Wireless Communications: Principles and Practice.* New Jersey: Prentice Hall, 1996.

[20] A. Bohdanowicz, G.J.M. Janssen, and S. Pietrzyk, "Wideband indoor and outdoor multipath channel measurements at 17 ghz," *IEEE Vehicular Technology Conference, VTC-Fall*, vol. 4, pp. 1998–2003, 1999.

[21] S. Howard and K. Pahlavan, "Measurement and analysis of the indoor radio channel in the frequency domain," *IEEE Transactions on Instrumentation and Measurement*, vol. 39, no. 5, pp. 751–755, Oct. 1990.

[22] M. Yacoub, "Fading distributions and co-channel interference in wireless systems," *IEEE Antennas and Propagation Magazine*, vol. 2, no. 1, pp. 150–160, Feb. 2000.

[23] L. Fenton, "The sum of log-normal probability distributions in scatter transmission systems," *IRE Trans. on Communication System, COM-8*, pp. 57–67, Mar. 1960.

[24] J.-I. Chuang, "The effect of time delay spread on portable radio communications channels with digital modulation," *IEEE Journal on Selected Areas in Communications*, vol. 5, no. 5, pp. 879–889, Jun. 1987.

[25] B. Glance and L. Greenstein, "Frequency selective fading effects in digital mobile radio with diversity combining," *IEEE Transaction on Communications*, vol. 31, no. 9, pp. 1085–1094, Sep. 1983.

[26] G.J.M. Janssen, P.A. Stigter, and R. Prasad, "Wideband indoor channel measurements and BER analysis of frequency slective channels."

[27] J. Pierce and S. Stein, "Multiple diversity with nonindependent fading," *Proc. IRE*, vol. 48, pp. 89–104, Jan. 1960.

[28] A. Papoulis, *Probability, Random Variables, and Stochastic Processes.* Third Edition, McGraw-Hill International Editions, 1991.

[29] H. Suzuki, "A statistical model for urban radio propagation," *IEEE Transaction on Communications*, vol. 25, no. 2, pp. 673–680, Jul. 1977.

[30] A. Saleh and R. Valenzuela, "A statistical model for indoor multipath propagation," *IEEE Journal on Selected Areas in Communications*, vol. 5, pp. 128–137, Feb. 1987.

[31] Q. Spencer, M. Rice, B. Jeffs, and M. Jensen, "A statistical model for angle of arrival in indoor multipath propagation," *IEEE Vehicular Technology Conference*, vol. 3, no. 47, pp. 1415–1429, May 1997.

[32] H. Hashemi, "Impulse response modeling of indoor propagation channels," *IEEE Journal on Selected Areas in Communications*, vol. 11, no. 7, pp. 967–978, Sep. 1993.

[33] H. Hashemi and D. Tholl, "Statistical modeling and simulation of the rms delay spread of indoor radio propagation channels," *IEEE Transaction Vehicular Technology*, vol. 43, no. 1, pp. 110–120, Feb. 1994.

[34] G.L. Turin, et al., "A statistical model of urban multipath propagation," *IEEE Transaction on Vehicular Technology*, vol. 21, pp. 1–9, Feb. 1972.

[35] H. Zaghbul, M. Fattouche, G. Morrison, and D. Tholl, "Comparison of indoor propagation channel characteristics at different frequencies," *Electronics Letters*, vol. 27, no. 22, pp. 2077–2079, Oct. 1991.

[36] H. Nikookar and H. Hashemi, "Statistical modeling of signal amplitude fading of indoor radio propagation channels," *IEEE Transactions on Vehicular Technology*, vol. 49, no. 2, pp. 594–606, Mar. 2000.

[37] R.A. Scholtz and M.Z. Win, "Impulse radio," *IEEE PIMRC97, invited paper*, pp. 245–267, 1997.

[38] A. Muqaibel, A. Safaai-Jazi, A. Attiya, B. Woerner, and S. Riad, "Path-loss and time dispersion parameters for indoor UWB propagation," *IEEE Transactions on Wireless Communications*, vol. 5, no. 3, pp. 550–559, Mar. 2006.

[39] A. Muqaibel and A. Safaai-Jazi, "A new formulation for characterization of materials based on measured insertion transfer function," *IEEE Transactions on Microwave Theory and Techniques*, vol. 51, no. 8, pp. 1946–1951, Aug. 2003.

[40] C.C. Chong and S.K. Yong, "A generic statistical-based UWB channel model for high-rise apartments," *IEEE Transactions on Antennas and Propagation*, vol. 53, no. 8, pp. 2389–2399, Aug. 2005.

[41] W. Turin, R. Jana, S. Ghassemzadeh, and C. Ricee, "Autoregressive modeling of indoor UWB channel," *IEEE Conference on Ultra Wideband Systems and Technologies*, pp. 71–74, May 2002.

[42] V. Erceg, et al., "A model for the multipath delay profile of fixed wireless channels," *IEEE Journal on Selected Areas in Communications*, vol. 17, no. 3, pp. 399–410, Mar. 1999.

[43] C.C. Chong, Y. Kim, and S.S. Lee, "Statistical characterization of the UWB propagation channel in various types of high-rise apartments," *IEEE Wireless Communications and Networking Conference*, vol. 2, pp. 944–949, Mar. 2005.

[44] J. Karedal, S. Wyne, P. Almers, F.Tufvesson, and A.F. Molisch, "Statistical analysis of the UWB channel in an industrial environment," *IEEE Vehicular Technology Conference, VTC-Fall*, vol. 1, no. 5, pp. 1058–1069, Sept. 2004.

[45] Y. Suzuki and T. Kobayashi, "Ultra wideband signal propagation in desktop environments," *IEEE Conference on Ultra Wideband Systems and Technologies*, vol. 47, pp. 493–497, Nov. 2003.

[46] T.B. Welch, R.L. Musselman, B.A. Emessiene, P.D. Gift, D.K. Choudhury, D.N. Cassadine, and S.M. Yano, "The effects of the human body on UWB signal propagation in an indoor enviroment," *IEEE Journal on Selected Areas in Communications*, vol. 20, no. 9, pp. 1778–1782, Dec. 2003.

[47] T. Zasowski, F. Althaus, M. Stager, A. Wittneben, and G. Troster, "UWB for noninvasive wireless body area networks: channel measurements and results," *IEEE Conference on Ultra Wideband Systems and Technologies*, pp. 285–289, Nov. 2003.

[48] S.S.M. Wong, F.C.M. Lau, and C.K. Tse, "Propagation characteristics of UWB radio in a high-rise apartment," *The 8th International Conference on Advanced Communication Technology (ICACT)*, vol. 2, pp. 914–918, Feb. 2006.

[49] K. Leechaikitjaroen, S. Promwong, P. Supanakoon, S. Chensirikul, and S. Kaewmechai, "Indoor measurement results of UWB impulse radio for shot-range wireless systems with RMS delay spread and path loss," *IEEE International Symposium on Communications and Information Technology (ISCIT)*, vol. 1, pp. 684–688, Oct. 2005.

[50] J. Choi, N-G. Kang, Y-S. Sung, and S-C. Kim, "Empirical ultra wide band path loss model in office environments," *IEEE Vehicular Technology Conference, VTC-spring*, vol. 4, pp. 1956–1960, Oct. 2006.

[51] A. Fort, C. Desset, J. Ryckaert, P.D. Doncker, L.V. Biesen, and S. Donnay, "An ultra-wideband body area propagation channel model from statistics to implementations," *IEEE Transactions on Microwave Theory and Techniques*, vol. 4, no. 4, pp. 1820–1826, June 2006.

[52] A. Molisch, "A comprehensive standarized model for ultrawideband propagation channels," *IEEE Transactions on Antennas and Propagation*, vol. 54, no. 11, pp. 3151–3166, Aug. 2006.

[53] P.C. Richardson, X. Weidong, and W. Stark, "Modeling of ultra-wideband channels within vehicles," *IEEE Journal on Selected Areas in Communications*, vol. 24, no. 4, pp. 906–912, Apr. 2006.

[54] A.V. Vorobyov, A.G. Yarovoy, P. Aubry, and L.P. Ligthart, "UWB propagation channel measurements for wpan scenarios," *IEEE European Conference on Wireless Technology*, pp. 221–224, Oct. 2007.

[55] A.V. Vorobyov, A.G. Yarovoy, and L.P. Ligthart, "Study of short-range trasmission of UWB signals," *IEEE European Conference on Wireless Technology*, pp. 1687–1690, Spt. 2006.

[56] J.D. Parsons, D.A. Demery, and A.M.D. Turkmani, "Sounding techniques for wideband mobile radio channels: a review," *IEE Proceedings-I*, vol. 138, no. 5, pp. 437–446, Oct. 1991.

[57] F.J. Harris, "On the use of windows for harmonic analysis with the discrete fourier transform," *Proc. IEEE*, vol. 66, no. 1, pp. 51–83, Jan. 1978.

[58] Z. Irahhauten, H. Nikookar, G.J.M. Janssen, and L.P. Ligthart, "UWB channel modeling based on wideband indoor channel measurements at 2.4, 4.75 and 11.5 GHz," *IEEE Symposium Communications and Vehicular Technology, SCVT*, vol. 1, no. 1, p. 23, wer. 2003.

[59] A. Muqaibel, *Characterization of Ultra Wideband Communication Channels.* USA: PhD thesis, 2003.

[60] Z. Irahhauten, A. Yarovoy, H. Nikookar, G.J.M. Janssen, and L. Ligthart, "Measurement setup for ultra wide band indoor radio channel characterization," *IEEE Symposium on Communications and Vehicular Technology, SCVT, Gent, Belgium*, Nov. 2004.

[61] R.V. de Jongh, M. Hajian, and L. P. Ligthart, "Antenna time domain measurement techniques," *IEEE Antennas and Propagation Magazine*, vol. 39, no. 5, pp. 7–11, Oct. 1997.

[62] Z. Irahhauten, "Measurement scenarios and procedures for ultra-wideband channel characterization," *Internal report, TUD*, Apr. 2004.

[63] R.V. de Jongh, M. Hajian, and L.P. Ligthart, "Time domain antenna measurement: implementation and verification of a novel technique," *European Microwave Conference*, vol. 1, pp. 470–475, Oct. 1997.

[64] H.G. Schantz, "Bottom fed planar elliptical UWB antennas," *IEEE Conference on Ultra Wideband Systems and Technologies*, pp. 219–223, Nov. 2003.

[65] Z. Irahhauten, A. Yarovoy, G.J.M. Janssen, H. Nikookar, and L.P. Ligthart, "Ultra-wideband indoor propagation channel: measurements, analysis and modeling," *IEEE European Conference on Antennas and Propagation, EuCap*, vol. 1, no. 1, pp. 1–6, Nov. 2006.

[66] Q. Li and W.S. Wong, "Measurements and analysis of the indoor UWB channel," *IEEE Vehicular Technology Conference, VTC*, vol. 1, pp. 1–5, Oct. 2003.

[67] Z. Irahhauten and G. Janssen, "Ultra-wideband channel measurements in the laboratory for "Apparatenbouw en Proces Industrie" (API)," *Report, carried out as part of the "Haalbaarheidsstudie UWB Test Bed", TUD*, Apr. 2005.

[68] C-C. Chong, Y. Kim, and S-S. Lee, "A modified S-V clustering channel model for the UWB indoor residential environement," *IEEE International Conference on Ultra-Wideband*, vol. 1, no. 5, pp. 113–117, Sept. 2005.

[69] C. Kim, X. Sun, L. Chiam, B. Kannan, F. Chin, and H. Garg, "Characterization of ultra-wideband channels for outdoor office environment," *IEEE Wireless Communications and Networking Conference*, vol. 2, pp. 950–955, Mar. 2005.

[70] F. Ramirez-Mireles, M. Win, R. Scholtz, and M. Barnes, "Ultrawide bandwidth (UWB) signal propagation for outdoor wireless communications," *IEEE Vehicular Technology Conference*, vol. 1, pp. 251–255, May 1997.

[71] G. Janssen and Z. Irahhauten, "Description of the environment for the EuropCom UWB channel measurements," *Internal Report, carried out as part of the EuropCom project, TUD*, Jun. 2005.

[72] Z. Irahhauten, J. Dacuña, G. J. M. Janssen and H. Nikookar, "UWB channel measurements and results for wireless personal area networks applications," *IEEE European Conference on Wireless Technology*, pp. 209–212, Oct. 2005.

[73] R. Vaughan and N. Scott, "Super-resolution of pulsed multipath channels for delay spread characterization."

[74] A. Molisch, K. Balakrishnan, D. Cassioli, C.C. Chong, S. Emami, A. Fort, J. Karedal, J. Kunisch, H. Schantz, U. Schuster, and K. Siwiak, "IEEE 802.15.4a channel model: final report," *IEEE P802.15-04/662r0-SG4a*, Mar. 2003.

[75] M.Z Win and R.A. Scholtz, "On the robustness of ultra-wide bandwidth signals in dense multipath environments," *IEEE Communications Letters*, vol. 2, no. 2, pp. 51–53, Feb. 1998.

[76] J. Romme and B. Kull, "On the relation between bandwidth and robustness of indoor UWB communication," *IEEE Conference on Ultra-Wideband Syetems and Technologies, UWBST*, pp. 255–259, Nov. 2003.

[77] J. Foerster, "Channel modeling sub-committee: Final report," *IEEE P802.15-02/490rl-SG3a*, Mar. 2003.

[78] H. Nikookar, *Wireless Channel Modeling and Code Division Multiple Access for Indoor Communications.* The Netherlands: PhD thesis, 1995.

[79] C.C. Chong and S.K. Yong, "A statistical based UWB multipath channel model for the indoor environments wpan applications," *Personal Indoor and Mobile Radio Communications (PIMRC)*, vol. 2, pp. 916–920, Sept. 2005.

[80] C.A. Balanis, *Antenna Theory: Analysis and Design.* Canada: John Wiley and Sons, 1997.

[81] R. Schmitt, *Electromagnetics Explained.* Newnes, 2002.

[82] Z. Irahhauten, J. Dacuna, G.J.M. Janssen, H. Nikookar, A. Yarovoy, and L.P. Ligthart, "Link budget analysis and modeling of short-range UWB channels," *IEEE Transaction on Antennas and Propagation*, vol. 56, no. 8, p. 2008, Aug. 2008.

[83] A.V. Vorobyov, J.H. Zijderfeld, A.G. Yarovoy, and L.P. Ligthart, "Impact common mode currents on miniaturized UWB antenna performance," *IEEE European Conference on Wireless Technology*, Oct. 2005.

[84] A.G. Yarovoy, A.D. Schukin, I.V. Kaploun, and L.P. Ligthart, "The dielectric wedge antenna," *IEEE Transactions on Antennas and Propagation*, vol. 50, no. 10, pp. 1460–1472, Oct. 2002.

[85] Z. Irahhauten, J. Dacuna, G.J.M. Janssen, H. Nikookar, A. Yarovoy, and L.P. Ligthart, "Analysis and modeling of near-field effects on the link budget for UWB-WPAN channels," *IEEE International Conference on Communications, (ICC)*, p. 2008, May 2008.

[86] D. Hawbaker and T. Rappaport, "Indoor wideband radio wave propagation measurements at 1.3 GHz and 4.0 GHz," *Electronics Letters*, 1990.

[87] G.J.M. Janssen and R. Prasad, "Wideband indoor channel measurements and ber analysis of frequency selective multipath channel at 2.4, 4.75, and 11.5 GHz," *Vehicular Technology Conference*, vol. 2, no. 42, pp. 617–620, May 1992.

[88] D. Brandwood, "A complex gradient operator and its application in adaptive array theory," *IEE Proc., Parts F and H*, vol. 130, pp. 11–16, Feb. 1983.

[89] A.J van der Veen and G. Leus, *Signal Processing for Communications.* Course ET4-147, TU-Delft, 2007.

[90] W.C. Jakes, *Microwave mobile communications.* New York: John Wiley and Sons, 1974.

[91] Z. Irahhauten, P.R. Alvaro, G.J.M. Janssen, and H. Nikookar,, "A new approach for characterization of ultra wide band wireless channels," *IEEE Symposium on Communications and Vehicular Technology, SVCT*, Nov. 2004.

[92] Z. Irahhauten, G.J.M. Janssen and H. Nikookar, "Characterization of UWB wireless based on random partially known frequency responses," *IEEE International Conference on UWB, ICUWB*, Spt. 2005.

[93] R.C. Qiu, "A generalized time domain multipath channel and its applications in ultra-wideband (UWB) wireless optimal receiver design - part ii: physics-based system analysis," *IEEE Transaction on Wireless Communications*, vol. 3, no. 6, pp. 2312–2324, Nov. 2004.

[94] K. Heidary, "Ultra-wideband (UWB) incidence on multiple diectric interfaces," *IEEE International Symposium on Antennas and Propagation*, vol. 2, pp. 1315–1318, june 2004.

[95] S. Gezici, Zhi Tian, G.B. Giannakis, H. Kobayashi, A.F. Molisch, H.V. Poor, and Z. Sahinoglu, "Localization via ultra-wideband radios: a look at positioning aspects for future sensor networks," *IEEE Signal Processing Magazine*, vol. 22, no. 4, pp. 70–84, July 2005.

[96] Z.N. Low, J.H. Cheong, C.L. Law, W.T. Ng, Y.J. Lee, "Pulse detection algorithm for line-of-sight (los) UWB ranging applications," *IEEE Antennas and Wireless Propagation Letters*, vol. 4, pp. 63–67, 2005.

[97] W. Chung and D. Ha, "An accurate ultra wideband (UWB) ranging for precision asset location," *IEEE Conference on Ultra Wideband Systems and Technologies*, pp. 389–393, Nov 2003.

[98] K. Yu and I. Oppermann, "Synchronization, TOA and position estimation for low-complexity ldr UWB devices," *IEEE International Conference on Ultra-Wideband*, pp. 480–484, Sept. 2005.

[99] B. Denis, J. Keignart, and N. Daniele, "Impact of nlos propagation upon ranging precision in UWB systems," *IEEE Conference on Ultrawideband Systems and Technologies*, pp. 379–383, Nov. 2003.

[100] J.Y. Lee and R. A. Scholtz, "Ranging in a dense multipath environment using an UWB radio link," *IEEE Journal on Selected Areas in Communications*, vol. 20, no. 9, pp. 1677–1683, Dec. 2002.

[101] C. Mazzucco, U. Spagnolini, and G. Mulas, "A ranging technique for UWB indoor channel based on power delay profile analysis," *IEEE Vehicular Technology Conference, VTC*, vol. 5, no. 59, pp. 2595–2599, May 2004.

[102] Z. Sahinoglu and I. Guvenc, "Threshold-based TOA estimation for impulse radio UWB systems," *IEEE International Conference on Ultra-Wideband*, pp. 420–425, 5-8 Sept. 2005.

[103] Z. Irahhauten, G.J.M. Janssen, H. Nikookar, A. Yarovoy, and L.P. Ligthart, "UWB channel measurements and results for indoor office and industial environments," *IEEE International Conference on Ultra-Wideband (ICUWB), Boston, USA*, pp. 225–260, Sept. 2006.

[104] A. Muqaibel, A. Safaai-Jazi, A. Bayram, A.M. Attiya, and S.M. Riad, "Ultrawideband through-the-wall propagation," *IEE Proceedings Microwaves, Antennas and Propagation*, pp. 581–588, 9 Dec 2005.

List of Abbreviations

API	Apparatenbouw & Proces Industrie
CIR	Channel Impulse Response
D-CIR	Discrete CIR
CDF	Cumulative Distribution Function
dB	Decibel
DC	Direct Current
DS	Direct Sequence
DUCAT	Delft University Chamber for antenna under Test
EEMCS	Electrical Engineering, Mathematics and Computer Science
EIRP	Effective Isotropic Radiated Power
FCC	Federal Communications Commission
FD	Frequency Domain
FT	Fourier Transform
FFT	Fast Fourier Transform
GPS	Global Positioning System
GPIB	General Purpose Information Bus
IFT	Inverse Fourier Transform
IFFT	Inverse Fast Fourier Transform
IR	Impulse Radio
IRCTR	International Research Centre for Telecommunication and Radar
K-S	Kolmogorov-Smirnov test
LOS	Line of Sight
LNA	Low Noise Amplifier
MAR	Multiple Antenna Reflection
MD	Maximum Detection method
MP3	Media Player
MB	Multi-Band

MPC	Multipath component
NLOS	Non Line of Sight
OBS	Obstructed Line of Sight
QoS	Quality of Service
PC	Personal Computer
PDA	Personal Display Assistant
PDF	Probability Density Function
PDP	Power Delay Profile
PRF	Pulse Repetition Frequency
PRI	Pulse Repetition Interval
RDS	RMS Delay Spread
RMS	Root Mean Square
RF	Radio Frequency
SF	Sucoflex
SNR	Signal-to-Noise Ratio
TD	Time Domain
TDC	Time Decay Constant
TU	Technical University
TW	Time Window
TOA	Time of Arrival
TDOA	Time Difference of Arrival
UWB	Ultra Wide band
WPAN	Wireless Personal Area Networks
WLAN	Wireless Local Area Networks
WBAN	Wireless Body Area Networks

List of Symbols

$a_{l,k}$	multipath gain coefficient of the kth component in the lth cluster
A_s	maximum size of the antenna
B_w	bandwidth
$B^{rel}_{w_{eff}}$	effective bandwidth
c	speed of light
d	distance
d_0	reference distance
d_w	thickness of a wall
D	largest antenna dimension
E	electric field
E_i	incident electromagnetic pulse
E_r	reflected electromagnetic pulse
E_t	transmitted electromagnetic pulse through a medium
E^i_n	energy in the ith bin
f_s	sampling frequency
f_c	center frequency
G_t	gain of transmit antenna
G_r	gain of receive antenna
$h(t)$	channel impulse response
$h_{Tx}(t)$	transmit antenna response
$h_{Rx}(t)$	receive antenna response
$h_{sys}(t)$	impulse response of the measurement system
$H(f)$	channel transfer function
$I(.)$	current distribution
I_0	excitation current

$I_0(x)$	zero-order modified Bessel function
K	number of multipath components
l	dipole length
l_c	RF cable length
L	number of clusters
L_{total}	total channel loss
L_{ff}	far-field channel loss
N	number of bins
N_s	number of samples
N_c	number of measured chunks
OTI	overlap time interval
$P(\tau)$	channel power delay profile
$p_g(t)$	generator output
$PL(d)$	path-loss
$P_r(d)$	measured power
$p_{rx-los}(t)$	direct unobstructed LOS signal
$p_g(t)$	generator output
$r(t)$	received signal
r	distance, used only in chapter 5
r_c	cross-covariance matrix
r_{ff}	far-field distance
r_{nf}	near-filed distance
R	distance between two dipole antennas
R_c	auto-covariance matrix
$s(t)$	transmitted signal
T_b	bin size
T_l	time delay of the lth cluster
T_{max}	maximum time excess delay
T_{PRI}	pulse repetition interval
T_s	sampling time
TW	observation time window
V	voltage in the terminals of a dipole
V_r^{ff}	measured voltage in the far-field
V_r^{nf}	measured voltage in the near-field
X_σ	shadowing parameter
α	path-loss exponent
$\delta(.)$	Dirac delta impulse function
δ_D	distance decay constant
Δf_s	frequency spacing
ϵ_H	error in energy
ε	range error
ε_r	dielectric constant
ξ	threshold level

η	intrinsic impedance
γ_{FM}	fading margin
γ_{nf}	total channel loss
γ_{TIF}	threshold impact factor
γ_w	wall attenuation factor
γ	power decay constant for the rays
Γ	power decay constant for the clusters
Γ_i	correlation coefficient used in CLEAN algorithm
λ	mean ray arrival rate
λ_w	wave length
Λ	mean cluster arrival rate
$\tau_{l,k}$	delay of the kth component relative to the lth cluster arrival time T_l
τ_{rms}	root mean square delay spread
τ_{un}	unambiguous echo-path time-delay resolution
θ	azimuth angle
ϕ	elevation angle

Publications by the Author

Journal Papers

[J.1] Z. Irahhauten, J. Dacuna, G.J.M. Janssen, H. Nikookar, A. Yarovoy, and L.P. Ligthart, "Link budget analysis and modeling of short-range uwb channels", *IEEE Transaction on Antennas and Propagation*, Vol. 56, Issue 8, pp. 2730-2738, Aug. 2008.

[J.2] A.V. Vorobyov, S. Bagga, A.G. Yarovoy, S.A.P Haddad, W.A. Serdijn, J.R. Long, Z. Irahhauten, and L.P. Ligthart, "Integration of a pulse generator on chip into a compact ultrawideband antenna", *IEEE Transaction on Antennas and Propagation*, Vol. 56, Issue 3, pp. 858-868, 2008.

[J.3] Z. Irahhauten, H. Nikookar, and G.J.M. Janssen, "An overview of ultra wide band indoor channel measurements and modeling", *IEEE Microwave and Wireless Components Letters (WMCL)*, Vol. 14, Issue 8, pp. 386-388, Aug. 2004.

Conference Papers

[C.1] S. Bagga, Z. Irahhauten, S.A.P. Haddad, W.A. Serdijn, J.R. Long, and J. Pekarik, "A UWB transformer-C orthonormal state space band-reject filter in 0.13 μm CMOS", *IEEE conference on Solid-State Circuits, 34th European*, pp. 298-301, Edinburgh, UK, Sept. 2008.

[C.2] S. Bagga, Z. Irahhauten, W.A. Serdijn, J.R. Long, H. Pflug, and J. Pekarik, "A band-reject ir-UWB LNA with 20 dB WLAN suppression in 0.13 μm CMOS", *IEEE conference on Solid-State Circuits, Asian*, Fukuoka, Japan, Nov. 2008.

[C.3] Z. Irahhauten, J. Dacuna, G.J.M. Janssen, H. Nikookar, A. Yarovoy, and L.P. Ligthart, "Analysis and modeling of near-field effects on the link budget for UWB-WPAN channels", *IEEE International Conference on Communications (ICC)*, pp. 4872-4876, Beijing, China, May 2008.

[C.4] T. Gigl, G.J.M. Janssen, V. Dizdarevic, K. Witrisal, and Z. Irahhauten, "Analysis of a uwb indoor positioning system based on received signal strength", 4th *Workshop on Positioning, Navigation and Communication (WPNC)*, pp. 97-101, Hannover, Germany, Mar. 2007.

[C.5] Z. Irahhauten, A. Yarovoy , G.J.M. Janssen, H. Nikookar, and L.P. Ligthart, "Ultra wide band indoor channel: measurements, analysis and modeling", *IEEE European Conference on Antennas and Propagation (EuCap)*, Nice, France, Nov. 2006.

[C.6] Z. Irahhauten, G. Bellusci, G.J.M. Janssen, H. Nikookar, and C. Tiberius, "Investigation of uwb ranging in dense indoor multipath environments", *IEEE International Conference on Communication Singapore (ICCS)*, pp. 1-5, Singapore, Oct. 2006,

[C.7] Z. Irahhauten, G.J.M. Janssen, H. Nikookar, A. Yarovoy, and L.P. Ligthart, "UWB channel measurements and results for office and industrial environments", *IEEE International Conference on UWB (ICUWB)*, pp. 225-230, Boston, USA, Sept. 2006.

[C.8] Z. Irahhauten, J. Dacuna, G.J.M. Janssen, and H. Nikookar, "A link budget model for uwb-wpan applications", *IEEE European Conference on Wireless Technology (ECWT)*, pp. 95-98, Manchester, UK, Sept. 2006.

[C.9] Z. Irahhauten, J. Dacuna, G.J.M. Janssen, and H. Nikookar, "UWB channel measurements and results for wireless personal area networks applications", *IEEE European Conference on Wireless Technology (ECWT)*, pp.189-192, Paris, France, Oct. 2005.

[C.10] Z. Irahhauten, A. Yarovoy, G.J.M. Janssen, H. Nikookar, and L.P. Ligthart, "Suppression of noise and narrowband interference in UWB indoor channel measurements", *International Conference on UWB (ICUWB)*, pp. 108-112, Zurich, Switzerland, Sept. 2005.

[C.11] Z. Irahhauten, G.J.M. Janssen, and H. Nikookar, "Characterization of UWB wireless channel based on random partially known frequency responses", *Interactional Conference on UWB (ICUWB)*, pp. 103-107, Zurich, Switzerland, Sept. 2005.

[C.12] Z. Irahhauten, A. Yarovoy, G.J.M. Janssen, H. Nikookar, and L.P. Ligthart "Measurement setup for ultra wide band indoor radio channel characterization", *IEEE Symposium on Communications and Vehicular Technology in the Benelux (SCVT)*, Gent, Belgium, 2004.

[C.13] Z. Irahhauten, Alvaro R. Pastor, G.J.M. Janssen, and H. Nikookar, "A new approach for characterization of ultra wide band wireless channels", *IEEE Symposium on Communications and Vehicular Technology in the Benelux (SCVT)*, Gent, Belgium, 2004.

[C.14] Z. Irahhauten, A. Yarovoy, H. Nikookar, G.J.M. Janssen, and L.P. Ligthart,"Link budget evaluation for ultra wide band impulse radio transmission", *International Symposium on Antennas and Propagation, ISAP*, Sendai, Japan, Aug. 2004.

[C.15] Z. Irahhauten, A. Yarovoy, H. Nikookar, G.J.M. Janssen, and L.P. Ligthart, "The effect of antenna and pulse waveform on ultra wide band link budget with impulse radio transmission", *IEEE European Conference on Wireless Technology (ECWT)*, Vol. 1, pp. 113-116, Amsterdam, The Netherlands, 2004.

[C.16] Z. Irahhauten and H. Nikookar, "On the frequency dependence of wireless propagation channel's statistical characteristics", *IEEE conference on Vehicular Technology (VTC-Spring)*, Vol. 1, pp. 222-226, Jeju, South-Korea, Apr. 2003.

[C.17] Z. Irahhauten, H. Nikookar, G.J.M. Janssen, and L.P. Ligthart, "UWB channel modeling based on wideband indoor channel measurements at 2.4, 4.75 and 11.5 GHz", *IEEE Symposium on Communications and Vehicular Technology (SCVT)*, in the Benelux (SCVT 2003), Eindhoven, The Netherlands, Nov., 2003.

[C.18] Z. Irahhauten, H. Nikookar, and G.J.M. Janssen, "An overview of modeling of ultra wideband indoor channels", *IEEE European Conference on Wireless Technology (ECWT)*, Munich, Germany, Oct. 2003.

[C.19] H. Nikookar and Z. Irahhauten, "Statistical modeling of RMS delay spread of MIMO propagation channels", 6th *World Wireless Congress*, pp.73-78, San Diego, CA, USA, July 2003.

Relation to this thesis

This thesis is based, in part, on previously published results as listed above. The following table provides a good overview of the major and minor relations between these publications and the chapters of this thesis.

Table 8.1: *Relations between the publications and the chapters of this thesis: ●: major relation; ○: minor relation.*

Publication	Ch. 3	Ch.4	Ch. 5	Ch. 6	Ch. 7
J.1			●		
J.2	○	○			
J.3	●	●			
C.1					
C.2					
C.3		○	●		
C.4					●
C.5		●			
C.6					●
C.7		●			
C.8			●		
C.9		●	○		
C.10	●				
C.11				●	
C.12	●				
C.13				●	
C.14		○			
C.15		○			
C.16		○			
C.17		●			
C.18	●	○			
C.19					

Samenvatting

Op dit moment krijgt Ultra-wideband (UWB) technologie veel aandacht binnen het gebied van de draadloze communicatie, voornamelijk dankzij haar unieke mogelijkheden en potentiële toepassingen, mede dankzij de beschikbare brede licentievrije frequentieband. Nochtans, vereist het ontwerpen en succesvol implementeren van UWB transmissiesystemen een goed begrip van de propagatiekenmerken van het radiokanaal. Dit proefschrift gaat over de ontwikkeling van realistische kanaalmodellen ten behoeve van het ontwerp en de evaluatie van UWB systemen.

Er bestaan verschillende methoden om een UWB kanaalmodel te ontwikkelen. Dit proefschrift richt zich op een belangrijke methode die gebruik maakt van statistische methoden gebaseerd op metingen. Hiervoor is een tijddomein meetopstelling ontwikkeld, die de frequentieband van 3.1 tot 10.6 GHz afdekt. Verschillende beperkingen die specifiek zijn voor tijddomein metingen, worden onder de aandacht gebracht en er worden oplossingen voorgesteld om deze beperkingen te verwijderen. Vermits de prestaties van communicatiesystemen worden bepaald door de kenmerken van het radiokanaal waarin deze systemen opereren, zijn er metingen verricht in verschillende omgevingen b.v. op kantoor, in een industriële omgeving, van buiten naar binnen en in draadloze personal area network (WPAN) omgevingen. Om een goede statistische UWB kanaalkarakterisering te verkrijgen, is een voldoende aantal kanaalimpulsresponsies (CIRs) verzameld. Deze CIRs worden verkregen op basis van de tijddomein signaalmetingen met behulp van geschikte naverwerkingsmethodes. Gebaseerd op de gemeten gegevens, worden verschillende statistische kanaalmodellen voorgesteld voor de frequentieband van 3.1 tot 10.6 GHz, inclusief modellen voor grote, middelgrote en kleinschalige fading.

UWB is een veelbelovende technologie voor een aantal draadloze toepassingen met een klein bereik (b.v. WPAN). In deze toepassingen staan echter de zend- en ontvangstantennes heel dicht bij elkaar en zijn de zogenaamde verre-veld anten-

nevoorwaarden niet geldig, ook al worden deze voorwaarden wel aangenomen in de meeste beschikbare link budget modellen in de literature. Onder de nabije-veld voorwaarden worden afwijkingen in het link budget en de pulsvorm gevonden, in vergelijking met de verre-veld modellen. In dit proefschrift wordt een nieuw empirisch UWB link budget model voorgesteld voor UWB kanalen met een kort bereik. Verder wordt dit nieuw model gevalideerd door metingen en simulaties, gebruik makende van verschillende soorten antennes. Het voorgestelde model bevat de frequentie, de antenne afmetingen en -oriëntatie als parameters en toont een goede overeenkomst met de simulaties en de metingen.

Voor het statistisch modeleren van UWB kanalen, wordt gewoonlijk de hele UWB band gemeten. Maar wegens de grote bandbreedte wordt de meetopstelling al snel complex en als gevolg daarvan moeten verschillende parameters in rekening gebracht worden. Hier wordt een nieuwe benadering voorgesteld om het draadloze UWB kanaal te schatten, waarbij enkel gedeeltelijke kanaalinformatie uit een aantal subbanden wordt gebruikt in het schattingsproces.

Plaatsbepaling in binnenomgevingen is een belangrijke toepassing van UWB voornamelijk voor draadloze ad-hoc netwerken en locatie-afhankelijke radiodiensten. Een van de hoofdoelen van plaatsbepaling is om een goede afstandsschatting te krijgen. Gewoonlijk hangt de noodzakelijke afstandsnauwkeurigheid af van de toepassing en deze kan variëren van enkele centimeters tot enkele tientallen meters. UWB radio blijkt een veelbelovende oplossing te zijn voor het bereiken van een hoge nauwkeurigheid. Het laatste deel van dit proefschrift handelt over de toepassing van UWB technologie voor afstands/plaatsbepaling. Zo worden bijvoorbeeld verschillende methoden geëvalueerd, die gebaseerd zijn op aankomsttijd of signaalsterkte, om de afstand in binnenomgevingen met vele reflecties te schatten.

Zoubir Irahhauten
Delft, September 2008

Acknowledgements

I am indebted to a number of people who directly or indirectly contributed to the completion of this thesis.

First of all, I would like to thank my supervisors Dr. Gerard Janssen (also co-promotor) and Dr. Homayoun Nikookar for their guidance and support during my research work. Also I would like to thank Prof. Alex Yarovoy for his help and fruitful discussions especially in the beginning of my research.

I would like to owe my gratitude to my promotor Prof. Leo Ligthart for giving me the opportunity to pursue this thesis, and also for his valuable comments on the manuscript.

Many thanks go to Dr. Geert Leus for his encouragement to finish writing this thesis and of course for enjoying the work with him in the CAS group and 3UB company. I would also like to thank, ***all*** my colleagues from the WMC, NAS, CAS and IRCTR groups for their inspiring atmosphere, ***all*** members of the projects (Air-Link, EuropCom, Smart-PEAS) in which I was/am involved, ***all*** members of 3UB company, and ***all*** my friends in The Netherlands as well as in Morocco. Special thanks also go to my ex-roommates Marco Pausini, Nauman Kiyani and roommate Antoon Frehe for their humor and creating a nice work environment. I would like to thank Sumit Bagga, Dr. Wouter Serdijn, Giovanni Bellusci, Umar Rizvi and Javier Dacuna for their ambitions and collaboration.

I would like to thank Laura (Bauman), Marjon, Wendy, Mia, Dominique, Rowena and Laura (Bruns) for their constant help with the administrative matters. The experiments presented in this thesis were conducted with the technical support from several people of IRCTR. In particular, I would like to thank Pascal Aubry who gave his assistance for developing the measurement set-up and also for performing the measurements; Johan Zijderveld, for the calibration of all antennas; and Paul Hakkaard for providing all necessary UWB components.

I am, of course, particularly indebted to my parents, my sisters and my brother for their monumental, unwavering support and encouragement on all fronts.

Zoubir Irahhauten
Oujda, December 2008

Curriculum Vitae

Zoubir Irahhauten was born in Oujda, Morocco, on 23 October 1973. He received the "Diplome Universitaire de Technologie" certificate in Electrotechnics from the High school of Technology, University of Mohammed V in Oujda, in June 1995. Just after that he started working at the Atlas Bootling Company as a technician superior.

In 1996 he came to The Netherlands to continue his study at Delft University of Technology (TUD). After getting the Dutch language certificate he was enrolled with TUD in 1997. He received the B.Sc. and M.Sc. degrees both in Electrical Engineering in 2000 and 2002, respectively. Zoubir performed his graduation work at the International Research Center for Telecommunication and Radar (IRCTR) on the subject of: "On the frequency dependence of wireless channel's propagation characteristics".

In October 2002 he started his work towards the Ph.D. degree in the Wireless Mobile Communications (WMC) group and IRCTR which resulted in this dissertation. Since June 2006, is involved in the 3UB start-up company aiming to develop advanced wireless systems, solutions and chip design. In August 2007, he started working as a postdoc in the Circuits and Systems (CAS) group at TUD where he is involved in the development of channel models and antenna design for UWB communication and positioning systems for underwater applications.